July 2020

KINETICS OF THE CRYSTAL-MELT PHASE TRANSFORMATION IN SEMICRYSTALLINE POLYMERS

Kiran Subramaniam Iyer
University of Massachusetts Amherst

KINETICS OF THE CRYSTAL-MELT PHASE TRANSFORMATION IN SEMICRYSTALLINE POLYMERS

A Dissertation Presented

by

KIRAN SUBRAMANIAM IYER

Submitted to the Graduate School of the
University of Massachusetts Amherst in partial fulfillment
of the requirements for the degree of

DOCTOR OF PHILOSOPHY

May 2020

Department of Chemical Engineering

KINETICS OF THE CRYSTAL-MELT PHASE TRANSFORMATION IN SEMICRYSTALLINE POLYMERS

A Dissertation Presented

by

KIRAN SUBRAMANIAM IYER

Approved as to style and content by:

Murugappan Muthukumar, Chair

Dimitrios Maroudas, Member

Sarah Perry, Member

Jonathan Machta, Member

John Klier, Department Chair
Department of Chemical Engineering

DEDICATION

To my parents and my sister, my sources of inspiration and strength

ACKNOWLEDGMENTS

I am forever grateful to my advisor Professor Muthukumar for his timely guidance and useful advice. Professor Muthukumar is a very thorough and careful physicist, and this rubs off on the entire group. I have enjoyed all my discussions with him, whether scientific or related to anything else. He has afforded with immense professional and scientific freedom, from which I have greatly benefited. His scientific temperament and his leadership of the group are phenomenal. Professor Muthukumar has made me into a competent professional from a young kid.

I would like to express my gratitude to Professor Machta, Professor Maroudas and Professor Perry for serving on my committee. I have interacted with them from time to time, and they always had very sound advice. Professor Machta helped me to design an algorithm, for which I am thankful to him.

This PhD would not have been possible without the ever-present discussions with the members of the Muthukumar group. Over the years, I have had the pleasure of interacting with some great scientists. I would like to express my deepest gratitude to Dr. Anand Rahalkar, Dr. Harshwardhan Katkar, Dr. Debasish Mondal, Dr. Prabhat Tripathi, Dr. Zachary Dell, Dr. Sabin Adhikari, Dr. Jyoti Prakash Mahalik, Dr. Hamidreza Shojaei, Dr. Ining Jou, Dr. Kateryna Khairulina, Sadhana Chalise, Uma Nudurupati, Dr. Michael Leaf, Khatcher Margossian, Dr. Di Jia.

I would like to specially thank the collaborators on two of my projects: Marzbed Margossian and Uma Nudurupati. I learned a lot, while working alongside them.

I have received a tremendous amount of mentorship from the senior students in Chemical engineering, who have helped me without any inhibitions at times of dire

need - Dwaipayan, Harsh, Aditya, Navaid, Ishan, Ashutosh, Ashish, Shashank, and Achyuta Teella. Dwaipayan has been a source of constructive criticism from the beginning of my time in the group, and this document has been written with his support.

I would like to thank my Chemical engineering class of 2014. We were one of the largest classes of recent times - Ryan, Sualyneth, Bryan, Brandon, Abhinav, Pranav, Koushik, Poonam, Greg, Vishnu, Yooyeon, Shuo, Yalin, Mengxi, Li-Wei, Yen, Haley, and Nur. I have shared many a fond memory with them, often while solving assignments and while studying for the qualifying exams in the first year offices.

I would like to express my gratitude to the office staff in the Chemical engineering and Polymer Science and Engineering offices - Marie, Amity, Anshalee, Maggie, Lisa Groth, Lisa McNamara, Jessica, Maria, and Lindy. They have ensured that all transitions from the very first day of my arrival in Amherst were extremely smooth.

I would like to express my deepest gratitude to Professor Neil Forbes, Professor T.J. Mountziaris, and Professor Maroudas for supporting me through the darkest phase of my time in graduate school.

I would like to thank all of my roommates Ashok, Kushal, Shreyas, Dwaipayan, Koushik, Ashish, Ashutosh, Ishan, Akash, Aritra, Mohit, Abhinav for always maintaining a good home.

I would like to thank my previous advisor Professor Sanjay Mahajani and his group members from the Indian Institute of Technology Bombay for always providing me with professional advice. They remain some of the nicest people that I know. I would also like to thank Professor Anurag Mehra of the Indian Institute of Technology for mentoring me whenever I needed advice.

I would like to thank my friends from the Institute of Chemical Technology (my alma mater) - Pranav, Sidhant, Swej, Chaitanya, Ghata, Akash, Sameer, Aniket, Bhavesh, Akshay and Sanket for their continuous encouragement.

I would like to extend my gratitude to my friends from high school - Aniruddha, Anantpal, Meher and Arjun for being the jokers that they are.

I would like to thank my relatives from California, Connecticut and North Carolina for always welcoming me into their homes.

I would like to thank my family - my mother, father and my sister. They have kept me mentally hungry and have always been there to discuss the day's progress. They have been with me through the highs and lows. The night's phone call is something that I will look forward to even tonight.

Finally, I would like to thank all those people who I have not mentioned. There is something I have learnt from every single person that I have met.

ABSTRACT

KINETICS OF THE CRYSTAL-MELT PHASE TRANSFORMATION IN SEMICRYSTALLINE POLYMERS

MAY 2020

KIRAN SUBRAMANIAM IYER

B.Chem.Engg, INSTITUTE OF CHEMICAL TECHNOLOGY MUMBAI

Ph.D., UNIVERSITY OF MASSACHUSETTS AMHERST

Directed by: Professor Murugappan Muthukumar

The assembly of long-chain polymers into an ordered state is a process that has puzzled polymer scientists for several decades. A process that is largely controlled by the strength of intermolecular attractions in small molecular systems, this crystallization in the case of polymers is controlled by a competition between the aforementioned force of attraction between monomers and the formidable conformational entropy of polymer chains. Any factor that affects this conformational entropy, whether that is an equilibrium thermodynamic factor or a kinetic factor, has the ability to control polymer crystallization. In this thesis, we focus on understanding the underlying kinetic processes that occur during this phase transition from liquid polymer to the solid semicrystalline state using computer simulations and some experiments.

We first investigate the effect of chain ends on crystallization by comparing between the crystallization behavior of linear and ring polymers of the same molecular weight using Langevin dynamics simulations. We find single linear polymers to melt

at much larger temperatures than single ring polymers, in apparent contradiction of equilibrium thermodynamic arguments. We study several kinetic factors, and find that they explain this discrepancy.

We then study the melting of linear polymers by Langevin dynamics simulations to understand the processes occurring during their disassembly. We find that polymer chains go through a globular metastable state at lower melting temperatures before transforming to expanded coils at higher melting temperatures. We also compute a free energy landscape using parallel tempering Langevin dynamics simulations, and confirm the existence of metastable states in the crystalline-amorphous reaction coordinate.

We look at the crystallization of triblock copolymers using Langevin dynamics simulations, in which crystallizable blocks are separated by non-crystallizable ones to understand the effect of impurities. We investigate the effects of tailored inter-block and solvent-block interactions, and discover a rich system in which the final semicrystalline polymer forms an array of morphologies.

We also experimentally investigate the crystallization of calcium oxalate, which is a primary constituent of kidney stones. We crystallize calcium oxalate and show images of crystals obtained from an optical microscope.

Lastly, we extend the scope of our studies into the effect of impurities by looking at crystallization of branched polymers. We discover that branches affect the kinetics of crystallization when they are in close proximity with one another.

TABLE OF CONTENTS

LIST OF TABLES

Table **Page**

LIST OF FIGURES

Figure **Page**

CHAPTER 1

INTRODUCTION

Polymers are widely used in everyday life owing to their remarkable material properties. Polymers offer tunable mechanical, chemical, and electronic properties, which can make a particular polymer be applicable for a wide variety of applications. For example, the same polyethylene that is used as lightweight shopping bags day-to-day can also be utilized as a bullet-proof vest when made simply using ultra-high molecular weight polyethylene. This versatility has led to the use of polymers as commodity materials, specialist materials, as well as materials which are currently being researched for futuristic purposes like a solar cell applications. A key feature of the solid structure of polymers which affects their material properties is their crystallinity. There are very few unifying concepts in the crystallization of polymers, despite several heroic attempts at generalizing them [1–3].

The crystallization process of polymers is fundamentally governed by the thermodynamic relation

$$A = U - TS, \tag{1.1}$$

where A is the Helmholtz free energy, U is the internal energy, T is the temperature and S is the entropy. For crystallization to be favored, the free energy for a transformation from molten state to a crystalline state has to be negative. For this to occur, either the change in the internal energy has to be negative or the TS term has to be sufficiently negative. In the case of crystallizable polymers, the propensity of attractive interactions is vastly outweighed by the formidable conformational entropy of the polymers. This means that polymers prefer to align in the solid state in the

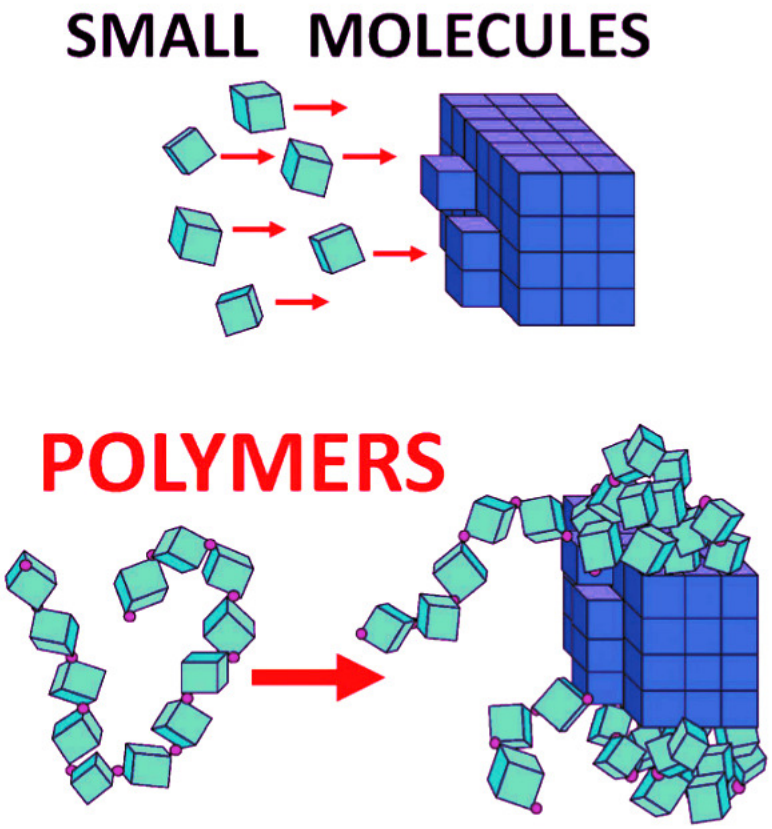

Figure 1.1. Polymers crystallize differently from small molecules, and do so by folding over themselves to form partly crystalline and partly amorphous states. This figure has been taken from the work of Reiter[4].

form of folded chains rather than elongated chains, as shown schematically in Figure 1.1 (adapted from Reiter [4]). This feature is totally different from the crystallization of small molecules. Essentially, the large conformational entropy controls the final crystalline structure, against a background of attractive interactions. Any factor that affects the entropy of the polymer, irrespective of whether it is a thermodynamic factor that governs equilibrium or a kinetic factor, has the ability to control the crystallization of the polymer. In this thesis, we study the effect of kinetic factors in a series of semicrystalline polymeric systems primarily using computer simulations and some experimental investigations.

In chapter 2, we investigate the differences in crystallization properties of a ring polymer, as compared to a linear polymer. Advances in catalysis have meant that ring polymers of high purity can be produced experimentally, and several researchers have experimentally investigated the crystallization of ring polymers. However, for the same polymer, different groups reported qualitatively different crystallization properties. To understand the variability in experimental results, and to develop a fundamental understanding of the differences between pure linear and ring polymers, we study the crystallization of single linear and single ring polymers. We find, contrary to equilibrium thermodynamic arguments, that ring polymers crystallize at much lower temperatures than linear polymers. An analysis of the early stage crystallization mechanism shows that ring and linear polymers crystallize through birth of baby nuclei with their coarsening depending uniquely on their topology. The single ring polymers nucleate faster than the single linear analogs and into several metastable lamellar thicknesses, although the motion of the monomers in both cases is comparable. Additionally, using multiple polymer molecules, we find that secondary nucleation of ring polymers proceeds with free energy barriers, as opposed to linear polymers where no barriers are found. Through these simulations, we argue that there are kinetic reasons for the lower melting temperature of the ring polymers.

In chapter 3, we investigate the reverse process of crystallization - melting, and do so for linear polymers. We consider two ideal situations: one in which we melt a single crystal, and the other in which we melt a multi-chain crystal. We show that the melting of the single crystal proceeds through a globular metastable state, which is followed by expansion to a more random coil-like state. Similarly, the melting of the multi-chain crystal reveals a special mechanism comprised of two steps: one in which a long-lived partially molten metastable state is formed, followed by a second step in which the chains peel off from the crystalline core to a free state. We elucidate the nature of the metastable state close to the equilibrium melting temperature, and

show that the multi-chain crystals equilibrate to states of intermediate order, with the extent of ordering decreasing as we increase the melting temperature. We quantify the kinetics of melting by estimating a free energy landscape using parallel tempering Langevin dynamics simulations. These simulations reveal a metastable state in the single molecule systems, allowing us to estimate the free energy barriers. Additionally, the melting of the multi-chain crystals reveal the existence of two barriers, with the preference for the intermediate state reducing with increasing temperature.

In chapter 4, we study the effect of blocky impurities on the crystallization of linear polymers. The effect of blocky impurities on the melting temperature is captured fundamentally by Flory's lattice-based calculation [5]. However, this does not explain the effect of crystallization kinetics on the melting point, which means that blocky polymers require further investigation. In this chapter, we study triblock copolymers of ABA and BAB type, where A is a crystallizable block and B is a non-crystallizable block, and we compare the simulation results from these systems to those of a crystallizable polymer of equal molecular weight. We tailor the interaction between A and B blocks, and between B blocks and the solvent. We find that these interactions greatly affect the melting point, as well as the final equilibrium morphology of the polymers. Having established these differences, we recommend several future investigations to complete this study.

In Chapter 5, we attempt to experimentally investigate the effect of polyelectrolyte additives on the crystallization of Calcium oxalate, which is a primary component of kidney stones. The kidney stone disease affects large parts of the human population, and is caused due to excess concentration of oxalate ions in the body. To mitigate kidney stones, several researchers have attempted to break the crystals, either before they nucleate, or before they grow. This has led to several fundamental investigations, which aim to elucidate the effect of polyelectrolyte additives on the crystallization of calcium oxalate. These investigations have shown that only anionic polyelectrolytes

affect the crystallization of calcium oxalate. We attempt to resolve this mystery experimentally by first crystallizing calcium oxalate, following the procedure of Chung and co-workers [6], and then suggest a few ideas for future investigations.

In Chapter 6, we extend our simulations to study branched polymers. Fundamentally, branches act as impurities and their effect has been quantified by Flory's theory [5], which predicts a depression in the melting temperature due to branching. However, the effect of branches on the nucleation mechanism of polymers and the motion of the monomers has not been quantified. We study the crystallization of three types of systems: one in which the branches are confined to an end of the polymer, another in which the branches are spread out across the polymer, and a third one in which the degree of branching is very high. We maintain the nature of the branches to mimic octene. Branches are attached on every 21^{st} monomer for the first and third systems, while they are on every 100^{th} monomer for the second system. We find through our simulations that the branches tend to break up the "baby nuclei" (as coined by Muthukumar and Welch [7]), which are formed along the chain, when the branches are in close proximity to one another. In the case where the branches are separated by 100 monomers, the branches do not disrupt the formation of nuclei. In all the cases where crystallization occured successfully, branches were found to be expelled to the periphery of the single chain crystal. Having established this, we recommend several ideas for future investigations, so as to complete this study.

CHAPTER 2

LANGEVIN DYNAMICS SIMULATION OF CRYSTALLIZATION OF RING POLYMERS

This chapter was published as Iyer and Muthukumar, Langevin dynamics simulation of crystallization of ring polymers, *Journal of Chemical Physics* **148**, 244904 (2018).

2.1 Introduction

Ring polymers are macromolecules without chain ends. Such unending molecules have been of interest to polymer scientists for several decades now, beginning with the early discovery that their radius of gyration is half of that of their linear counterparts[8]. Thereafter, several investigations have attempted to quantify the equilibrium and non-equilibrium properties of ring polymers. The main theoretical interest has been due to the behavior of ring polymers as self-avoiding random walks which have to return to the origin. Since chain reptation is not possible in unknotted melts of these ring polymers, they do not conform to the standard models of chain relaxation[9–12].

Ring polymers have several startling differences in their properties as compared to linear polymers. The relaxation of knotted and unknotted ring polymers has been investigated by several other authors and shown to be remarkably different from the Zimm predictions of the relaxation time for the linear polymers[9, 13, 14]. A single circular DNA (and other biological ring species[14, 15, 15, 16]) relaxes faster than a single linear DNA, and the scaling exponent of the diffusion constant with respect to the molecular weight M is closer to the case where excluded volume is absent[13].

At equilibrium, the lack of chain ends makes the cyclic species much more compact and crumpled than linear polymers[17–19]. There are several other features that arise as a result of endlessness[10, 20–22] including features in the crystallization properties[22, 23].

Experimental investigation of the crystallization of ring polymers has received a boost in recent years with the development of a novel metathesis catalyst which generates high purity ring polymers[24]. Following this, there have been in general two methods for the synthesis of cyclic polymers: ring closure and ring expansion[25], which have allowed several experimental investigations into their crystallization behavior. Contrasting rates of crystallization, melting temperatures and equilibrium melting points have been observed in experiments [26], and these experiments are not mutually conclusive. Experimental studies have been mainly conducted in the melt, with very few experiments probing the crystallization of single molecules from dilute solutions.

Many experimental studies determine spherulitic growth rates for linear and cyclic polymers of poly(ϵ-caprolactone)[26–32], poly(ethylene oxide)[33], and poly(lactide)[34], and show that cyclic polymers grow faster than linear polymers. On the other hand, for poly(tetrahydrofuran)[35] and polyethylene[36] the spherulitic growth rates for the linear species is higher than that of the ring species. In a set of separate experiments, the nucleation rate of spherulites was shown to be higher for the cyclic species in poly(tetrahydrofuran)[37].

Many studies also show differences in melting temperatures. Some authors report apparent melting temperatures T_m[24, 26–28, 35, 38, 38–41], while several others have reported equilibrium melting temperatures T_m^0[27, 28, 36–38, 40, 42]. The equilibrium melting temperature T_m^0 is the melting temperature of the infinite crystal and can only be obtained indirectly by measurements involving extrapolations, like in the case of the Hoffman-Weeks plot[3]. The apparent melting temperature T_m is

the temperature at which a crystalline sample undergoes a phase change to a liquid state when subjected to a particular heating rate, commonly in a differential scanning calorimeter. Several authors report contrasting melting behavior for linear and cyclic analogues of the same polymer, as is the case for polyethylene[24, 36], for example. For poly(tetrahydrofuran)[35], poly(lactide)[38, 39] and poly(ϵ-caprolactone)[40], apparent melting temperatures for the linear species have been shown to be higher than that of the ring analogue. Similarly, for polyethylene[36] and poly(tetrahydrofuran)[37], the equilibrium melting temperature of the linear polymer has been found to be higher. On the other hand, for polyethylene[24], poly(ϵ-caprolactone)[26–28] and polyolefins[41], the apparent melting temperatures of the linear polymer have been found to be lower than that of the ring species. Additionally, the equilibrium melting point for the ring poly(ϵ-caprolactone) has also been shown to be higher than its linear counterpart[27, 28]. Adding to the controversy, a third category of authors have found that the equilibrium melting points of ring and linear species are equal or not significantly different[38, 40, 42].

Several of these authors have provided interpretations about their respective findings as follows. The equilibrium melting temperature T_m^0 is defined as[43]

$$T_m^0 = \frac{\Delta H}{\Delta S}. \tag{2.1}$$

Here the ΔH is the enthalpy difference between the crystalline and the liquid phases, while the ΔS is the entropy difference between the crystalline and the liquid phases. Tezuka and co-workers[35] have argued that the monomers of the ring polymer will be more restricted in the crystalline phase and therefore, the cyclic system will have a larger entropy difference between its crystalline and liquid phases. They have used this reasoning to explain the lower melting point for the cyclic species. Several other authors[24, 28] have attributed the higher melting points of the cyclic species to the lower entropy difference between phases arising from a smaller number of microstates

accessible to it in the liquid state. It must be noted that in the various experimental systems the chemistries of the rings are quite different in terms of incorporation of catalysts during the synthesis and the efficiency of packing of the monomers into crystalline domains. Although it is unclear why these experiments disagree with one another, it is known that the presence of linear polymer impurities can also distort the data from ring polymer experiments considerably[9, 38, 44–47].

Very few experimentalists have studied the morphology of single crystals from rings[27, 33, 39]. Separate experiments on poly(ϵ-caprolactone) and poly(ethylene oxide) have confirmed that the nature of unit cells formed for both linear and ring species is similar, but they have noticed differences in the lamellar thicknesses. Zardalidis et al.[33] have confirmed that the lamellar thickness of the ring chain crystals is approximately half the distance of the extended chain conformation of the linear chain crystals, which is similar to what Sugai and co-workers[39] have shown. Additionally, Su et al.[27] have shown that cyclic chains crystallize into thicker lamellae than linear chains.

In such situations, where experiments disagree with one another, molecular simulations offer a suitable alterative to observe molecular behavior. Simulations have explained several features of polymer crystallization[43, 48–55] which could not be reconciled through experiments[7, 56, 57]. Simulations have shed a new light on several features like the effect of tilted lamellae[58] on morphology or the mechanism of early stage crystallization in polymers[7, 59]. In our earlier simulations[7], we have provided an explanation for the appearance of a peak at $q_{\max}$ in small angle X-ray scattering (SAXS) before any peak is obtained in wide angle X ray scattering (WAXS) by invoking the concept of "baby nuclei" formed at the very early stage of crystallization immediately after quench. In terms of nomenclature, these "baby nuclei" are distinguished from "intramolecular nucleation". When a full fledged nucleation inside a chain occurs as in a large crystallizing chain, the nucleus is well ordered as in the

eventual crystalline state. On the other hand, the baby nuclei are not fully crystalline. In the baby nuclei, the local monomer density is higher than that in the uncrystallized portion of the molecule and the local orientational order parameter within the baby nuclei is nonzero. In view of such observations in the simulations[7, 50], the phrases "baby nuclei" and "smectic pearls" are used to distinguish these structures from fully formed nuclei.

Similar to all of these discoveries using simulations, Xiao and co-workers[60] have studied the crystallization of ring polymer melts in comparison to linear polymer melts, and compared several crystallization properties and also the effect of entanglements on the crystallization of each system. Through their coarse-grained molecular dynamics simulations of the melt, they have found that the melting and crystallization temperatures of the cyclic polymer melts are higher than those of the linear polymer melts. But a key issue with this finding is that the determination of the melting point for polymers depends on the heating rate, and the non-equilibrium nature of the heating has to be accounted for when determining the melting point. Additionally, the authors report that the average stem lengths, which are equal to the lamellar thicknesses, for the cyclic polymers are 50% larger than those of the linear polymers. According to the Gibbs-Thomson equation[43], the degree of supercooling $\Delta T \left(= T_m^0 - T_m\right)$ for the cyclic polymers should then be lower than that for the linear polymer. Since the measurement of the stem length is made at the same temperature T_m for both systems, a natural conclusion is that the equilibrium melting point T_m^0 of the ring polymer should be lower than that of the linear polymer. This anomaly with the apparent melting temperatures is something that necessitates further clarification.

All of these works have shown that the molecular-level features of crystallization can be investigated using simulations. In an attempt to resolve the differences that arise in experiments and simulations and to uncover general crystallization principles

based on chain topology, we study the crystallization of single ring polymers and compare their behavior to that of single linear polymers, keeping the chain length constant. As opposed to the work of Xiao *et al.*[60], our focus is purely on the behavior of single molecules, although we also report behavior in the secondary nucleation regime using multiple molecules. Using our molecular model [7], which is derived after making modifications to another model that essentially reproduces several qualitative aspects of thermophysical properties of polyethylene [61], we observe several differences in the crystallization of linear and ring chains that highlight the complex role played by chain topology in crystallization. The primary goal of the present work is to identify the role of chain topology on the main features of crystallization by relegating the treatment of various chemical details related to the polymers for future work. Using Langevin dynamics simulations, we study the melting behavior, early stage mechanisms, lamellar thickness distributions, monomer diffusion up to long times, and secondary nucleation kinetics in the case of multiple molecules. We show differing features for each aspect. This chapter is organized as follows: in Section 2.2, we describe the simulation model; in Section 2.3 we discuss the results that we obtain from our simulations in its various subsections; we conclude in Section 2.4.

2.2 Simulation model

Our simulation model[7] incorporates just enough detail to obtain chain-folded structures without being very computationally intensive. This model is designed to mimic a polyethylene chain, with each methylene(CH_2) group taken to be a bead. We therefore have long chains of degree of polymerization up to 700. All the interaction parameters are modeled after the work of Paul *et al.*[61], which has successfully reproduced several thermophysical properties of polyethylene, with additional changes to the model. Firstly, although Paul *et al.*[61] treat the terminal methyl (CH_3) groups

separately, we treat all the beads of the chain to be the same. We make another minor modification to the model, which is discussed below.

Our model incorporates force fields to represent chain connectivity, chain rigidity and non-bonded interactions. Therefore, the total potential energy arises due to contributions from the chemical bonds, bond angles, dihedral angles and the van der Waals-like short ranged interaction. The potential energy associated with the chemical bonds is taken to be the harmonic form:

$$U_r = k\left(r - r_0\right)^2, \tag{2.2}$$

where r is the bond length and r_0 is the equilibrium bond length. In this potential, k is taken to be 115 kcal/mol Å^2 and the r_0 is taken to be 1.54 Å. The potential energy associated with the bond angle, defined as the angle formed between the bond vectors of any two successive bonds $\vec{r}_{12}$ and $\vec{r}_{23}$, is:

$$U_\theta = k_\theta\left(\cos\theta - \cos\theta_0\right)^2, \tag{2.3}$$

where θ_0 is 109° and k_θ is 60 kcal/mol.

To model chain stiffness, we invoke a potential energy arising due to the dihedral angle ϕ between the two planes formed by three successive bond vectors $\vec{r}_{12}$, $\vec{r}_{23}$ and $\vec{r}_{34}$. For this we adopt a multi-harmonic potential given by:

$$U_\phi = k_1\left(1 - \cos\phi\right) + k_2\left(1 - \cos 2\phi\right) + k_3\left(1 - \cos 3\phi\right), \tag{2.4}$$

where k_1 is 3.02 kcal/mol, k_2 is -0.560 kcal/mol and k_3 is 2.58 kcal/mol.

We model the non-bonded interactions by means of a modified Lennard-Jones potential:

$$U_{LJ} = \epsilon\left[\left(\frac{\sigma}{r}\right)^{12} - 2\left(\frac{\sigma}{r}\right)^{6}\right], \tag{2.5}$$

where the interaction strength ϵ is set to 0.112 kcal/mol. The equilibrium distance σ is 4.53 Å for beads further than five repeat units apart along the chain backbone. Beads closer than five repeat units interact with a reduced value of σ equal to 1.54 Å. This is expected to have only modest changes on the global behavior of the chain other than slightly increasing the chain's local flexibility. The form of the Lennard-Jones potential is slightly different from the usual form, because here the Lennard-Jones potential has its minimum value at σ, rather than the usual $2^{\frac{1}{6}}\sigma$. All these modifications together make the chain different from the original polyethylene model[61], and the chain now represents only a model polymer chain capable of crystallizing.

For the simulation, we use reduced units everywhere, and all the results that we present are in these units. All quantities are derived from the basic units of mass (130 g/mol), equilibrium bond length r_0 (1.54 Å) and Lennard Jones energy ϵ (0.112 kcal/mol). The reduced time t^* is then given in units of $\sqrt{\frac{m\sigma^2}{\epsilon}}$ (2.57 ps) and the reduced temperature T^* is given in units of $\frac{\epsilon}{k_B N_A}$ (56.38 K), where k_B is the Boltzmann constant and N_A is the Avogadro number.

We have calculated an approximate value of the persistence length l_p according to the relation[62]

$$\langle \mathbf{l}_i \cdot \mathbf{l}_j \rangle = l^2 \exp\left(\frac{-l|i-j|}{l_p}\right), \tag{2.6}$$

where $\mathbf{l}_i$ represents the i^{th} bond vector, l represents the equilibrium bond distance and l_p represents the persistence length. By taking an average over 1000 snapshots of a linear polymer consisting of 700 monomers at a reduced temperature of $T^* = 12$, we find the value of the persistence length to be 7.52 (11.58 Å), after all the modifications to the model.

The interaction potentials are combined and integrated[63] with respect to time by using the methodology of Langevin dynamics[64, 65]; the motion of the particles is described by a set of Langevin equations, wherein the particles are subjected to the Langevin thermostat along with the interaction potentials. This is collectively given

by the equation

$$\ddot{\mathbf{r}}_i = -\nabla_r U_i - \zeta \dot{\mathbf{r}}_i + \mathbf{\Gamma}_i(t). \tag{2.7}$$

Here U_i is the total interaction potential acting on the i^{th} bead as described above. The $\zeta \dot{r}_i$ term represents the frictional drag, ζ is the friction coefficient, and Γ represents the random noise.

The Langevin dynamics method simulates the solvent by assuming that the solvent particles collide with the solute particles, but their size is negligible compared to the solute molecules. Hence the entire collision can be parametrized in terms of a Gaussian white noise $\mathbf{\Gamma}$, which satisfies the fluctuation-dissipation theorem

$$\langle \mathbf{\Gamma}_i(t) \cdot \mathbf{\Gamma}_i(t') \rangle = 6 k_B T \zeta \delta(t - t'). \tag{2.8}$$

Additionally, this Gaussian noise has the property of being time-averaged to 0.

$$\langle \mathbf{\Gamma}_i(t) \rangle = 0 \tag{2.9}$$

We set the friction coefficient ζ to be 1, and integrate the Langevin equation using the velocity Verlet finite difference algorithm[61, 65]. In this algorithm, the velocities of the particles are calculated at every half timestep, before computing the new positions using those half timestep velocities, leading to greater accuracy. The time step size that we use in these simulations is 0.001.

Throughout the simulations, we calculate several quantities which are of interest to us. These include the radius of gyration, kinetic and potential energies and the orientational order parameter P_2 as

$$P_2 = \frac{\langle 3\cos^2\theta - 1 \rangle}{2} \tag{2.10}$$

where θ is the angle between all pairs of orientational vectors $\mathbf{r}_{i+1} - \mathbf{r}_{i-1}$ for any bead i.

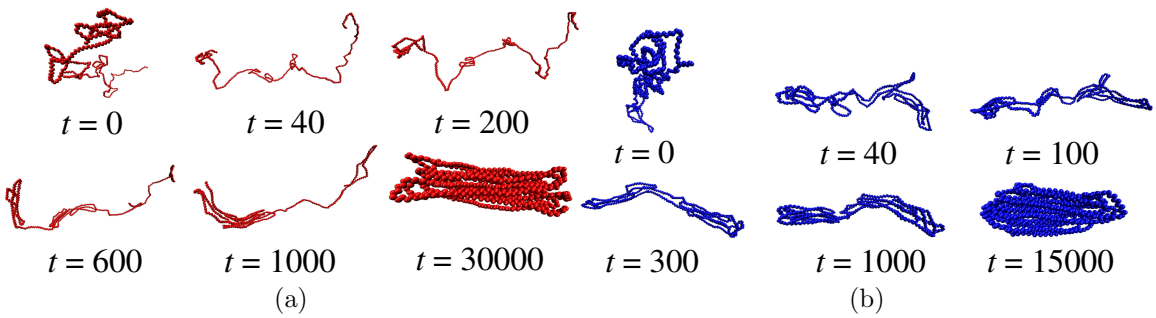

Figure 2.1. The evolution of crystallization in (a) linear and (b) ring polymer chains into lamellae.

2.3 Results and discussion

2.3.1 General crystallization procedure

We first studied the primary nucleation in a single linear chain and a single ring chain consisting of 700 monomers. In this process, a polymer forms a folded lamellar structure beginning from an expanded, coil-like structure. To achieve this, we start with a structure where the bond angle is set to 109°, and the dihedral angle is set to 120° and all the monomers are at a distance of 1 unit away from each other. We equilibrate both polymers at a temperature $T^* = 12$, well above the previously determined melting point for this model chain[48]. After equilibrating for enough time to ensure that the chain has acquired its equilibrium radius of gyration at higher temperatures, we quench the chain to a temperature of $T^* = 9$ and we start observing the "baby nuclei"[53, 54]. Subsequent structural analysis had revealed that this mechanism matches well with the observation of an early stage peak in small angle X-ray scattering, before any peaks are observed in wide-angle X-ray scattering[7, 57, 66]. We have in general studied two cases for the ring polymer: one where the quench temperature is $T^* = 9$ and the other in which the quench temperature is $T^* = 7.79$. The first case represents crystallization at the same temperature of crystallization T_c as the linear polymer, while the second case represents crystallization at an equal degree of supercooling $\Delta T \left(= T_m^0 - T\right)$ for ring and linear polymers.

Figure 2.1 depicts a typical crystallization process of both linear and ring polymers, rendered using the VMD package [67]. As seen in these snapshots, there are regions of local orientational order formed after the quenching stage. These structures have been referred to as "baby nuclei" or "smectic pearls" [7, 50] due to the fact that they serve as partially ordered nuclei within a single chain. After the formation of these baby nuclei, the strands connecting them are reeled in monomer-by-monomer while the baby nuclei grow in size. Then, these nuclei merge to form a large single crystal. This process for crystallization of the linear polymer was depicted in our earlier work [7, 48, 49]. We find that the process of crystallization of the ring polymer is qualitatively similar to that of the linear polymer, but with significant differences due to the inherent endless nature of the ring polymer. We illustrate these differences as follows.

2.3.2 Determination of melting points

We have determined the apparent melting points as well as the equilibrium melting points of both ring and linear polymers. To achieve this, we heat ring and linear polymer crystals at different heating rates. During this process, we have used the global average of the second order Legendre polynomial P_2 as an order parameter, wherein the polynomial is calculated from Equation 2.10 by taking an average over the entire system. A typical evolution of the P_2 is given in Figure 2.2. A transition is seen when there is an almost discontinuous change in the value of the P_2, beyond generic fluctuations about a particular average value. For trajectories like in the case of Figure 2.2a, this can be very easily determined, as the point at which a discontinuous change is discernible. For trajectories like those depicted by Figure 2.2b, where the transition point is difficult to be identified, a running average over every 1000 timesteps is taken, which enables the identification of the point at which a discontinuous change takes place. The values of P_2 are output to a file at every

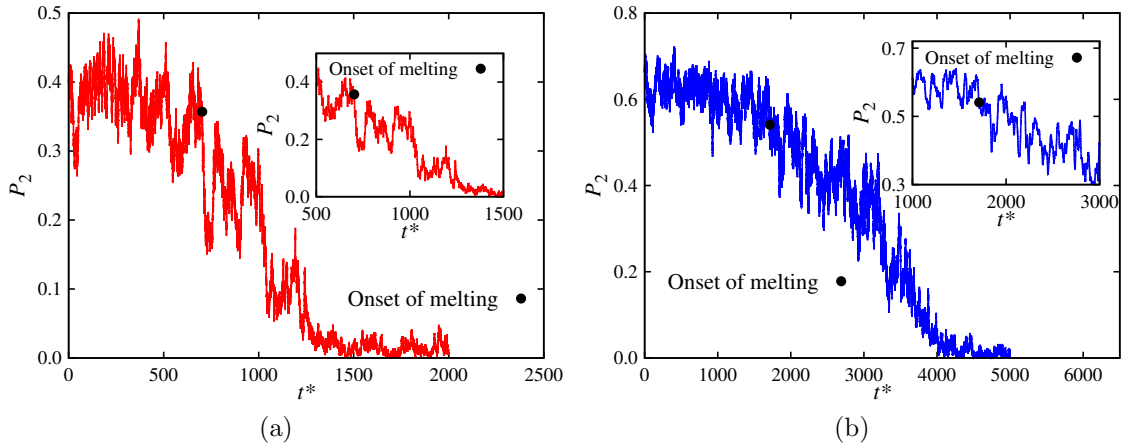

Figure 2.2. The variation of the orientational order parameter P_2 as the crystal is melted, beginning from a crystalline structure at $t^* = 0$. The heating rate for the linear polymer in (a) is $0.0015T^*/t^*$, while the heating rate for the ring polymer in (b) is $0.001T^*/t^*$. The onsets of melting are found by determining the first time instant at which a change in the value of P_2 is seen (by monitoring the running average over every 1000 time steps), beyond generic fluctuations about an average. By this process, the onset of melting for the linear polymer is determined to be at $T^* = 11.05$, while that for the ring polymer is determined to be at $T^* = 9.71$, as indicated by the corresponding points in black in the figure.

timestep, which generates a small inherent uncertainty in the determination of the onset of melting, equal to a value of $T^* = 1000\Delta t\dot{h}$. Here Δt corresponds to the step size, which is equal to the value of 0.001 as described previously in Section 2.2, and $\dot{h}$ corresponds to the heating rate. By this process, the onset of melting for the linear polymer in Figure 2.2a is determined to be at $T^* = 11.05$, while that for the ring polymer in Figure 2.2b is determined to be at $T^* = 9.71$. The onset of this step change is then taken to be the melting point for that particular crystal and that particular heating rate.

To calculate the melting points, the linear chains were heated to $T^* = 15.0$, then crystallized by quenching to $T^* = 10.0$ and then heated at various rates to $T^* = 13.0$. The ring chains were heated to $T^* = 15.0$, crystallized by quenching to $T^* = 8.0$ and then heated at various rates to $T^* = 13.0$, so as to be able to extract

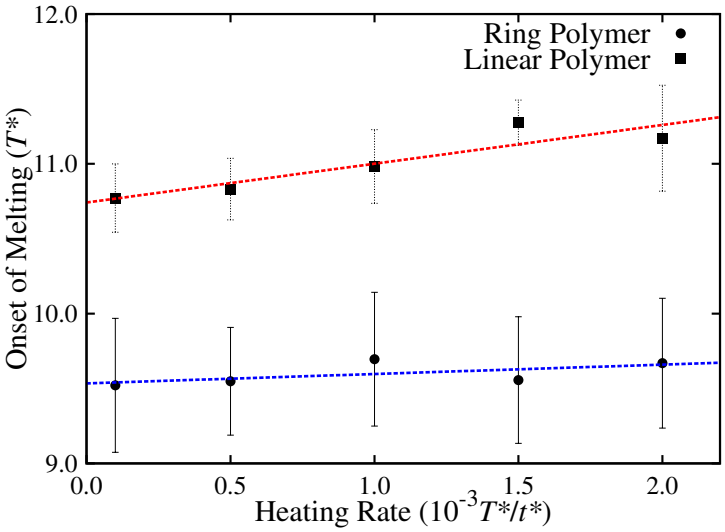

Figure 2.3. Melting temperature at different heating rates and extrapolating these onsets to zero heating rate. The equilibrium melting temperature as obtained by extrapolation to zero heating rate is $T_m^0 = 10.74 \pm 0.20$ in reduced units for linear chains and 9.53 ± 0.45 in reduced units for ring chains. The average lamellar thickness of the linear crystals is 11.34 ± 1.19, while that of the ring crystals is 10.89 ± 1.37. The method of calculation for the lamellar thickness will be explained in detail in the discussion on lamellar thicknesses.

the correct equilibrium melting point, in the absence of any existing data about its value. We computed the melting points of 15 different crystals, each heated at 5 different heating rates ranging from $0.0001\frac{T^*}{t^*}$ to $0.002\frac{T^*}{t^*}$. At each of these heating rates, the different onsets of melting were recorded. Then, these apparent melting points were extrapolated to zero heating rate to determine the equilibrium melting point T_m^0. This is shown in Figure 2.3. We found that the equilibrium melting point of the linear polymer was 10.74 ± 0.20, while the equilibrium melting point of the ring polymer was 9.53 ± 0.45. This corresponds to a difference of 68°C in real units for the present model of the polymer.

Since the number of monomers in both model chains is the same, we expect the contribution of the enthalpy difference ΔH to the melting point to be comparable. Hence the more significant contribution towards the difference in equilibrium melting points is from the entropy difference ΔS. Intuitively, we can expect the linear chains

to have a larger number of microstates accessible to them, indicating that the entropy of linear chains must, in general, be higher than that of the ring chains. But this intuitive argument may not always hold in the case of a "difference" between entropies of the liquid and the solid states. While we suspect that the difference in the entropy between the ring and the linear systems could be the cause behind this anomalous behavior of the ring chains, a more thorough calculation of the entropy difference ΔS between the two phases is needed.

Our simulation findings have qualitative agreements with some published experiments, whereas with others there is a disagreement. Our apparent melting points T_m, which are the averaged onsets of melting as shown in the Figure 2.3 have found qualitative agreements with several experiments, such as the 40°C difference in melting points found in poly(lactide)[39]. As mentioned in Section 2.1, several experiments have shown that the apparent melting temperatures of the ring species is lower than that of the linear species[35, 38, 40]. Many studies have also shown that the equilibrium melting temperature T_m^0 is higher for the linear polymers[36, 37]. In the various experimental systems, it is clear that the chemistries of the polymers play a role in the relative crystallization behaviors of rings and linear chains, in addition to the role of the topological feature of the polymer. In our simulations, where only the topological effect of the model is considered, the melting temperature of the ring polymer is lower than that of a linear polymer.

2.3.3 Early stage mechanisms

In Figure 2.1, we have shown snapshots of the crystallization mechanism for single chains. In an effort to quantify the processes of crystallization in both ring and linear systems, we have computed the time-resolved scattering profiles. We obtain the scattering profiles by calculating the static structure factor as given by

$$S(q) = \frac{1}{N} \sum_{i=1}^{N} \sum_{j=1}^{N} \frac{\sin\left(|\mathbf{q}||\mathbf{r}_i - \mathbf{r}_j|\right)}{|\mathbf{q}||\mathbf{r}_i - \mathbf{r}_j|}, \tag{2.11}$$

analogous to our previous study[7], where $\mathbf{q}$ is the scattering wave vector.

We compute the structure factor at various times t beginning from the time at which the systems are quenched to the crystallization temperature T_c. We average these structure factors over 100 different trajectories for both systems. Then, we subtract the structure factor at $t = 0$ from the structure factor at each time to generate the contribution from only the crystallized parts of each chain.

Once these structure factors have been obtained, they are integrated with respect to q as

$$I(t) = \int_{q_{\min}}^{q_{\max}} 4\pi q^2 S(q)^{(t)}\, dq, \tag{2.12}$$

where $q_{\min}$ (0.005) and $q_{\max}$ (0.25) refer to the minimum and maximum values of the scalar wave vector q used for the integration, and the total scattered intensity I for each time t is computed. The numerical integration has been performed using the quad function provided by the Scipy package in Python, to which the structure factors are provided as returnable functions after interpolating with a cubic spline interpolation using the interp1d function provided by the Scipy package.

We also determine the mechanism of the early stage crystallization during this "induction phase". The rate of growth of fluctuations Ω_q at different length scales corresponding to q is computed according to the following relation

$$S(q)^{(t)} = S(q)^{(0)} \exp\left(2\Omega_q t\right). \tag{2.13}$$

We take the ratio of the structure factors $S(q)$ at different times t with the structure factor $S(0)$ at time $t^* = 0$ and we fit an exponential function with time. The resulting coefficient of time in the expression is then recorded as the Ω_q for that particular q. $\frac{\Omega_q}{q^2}$ is then plotted against the value of q^2 to ascertain the mechanism of the process.

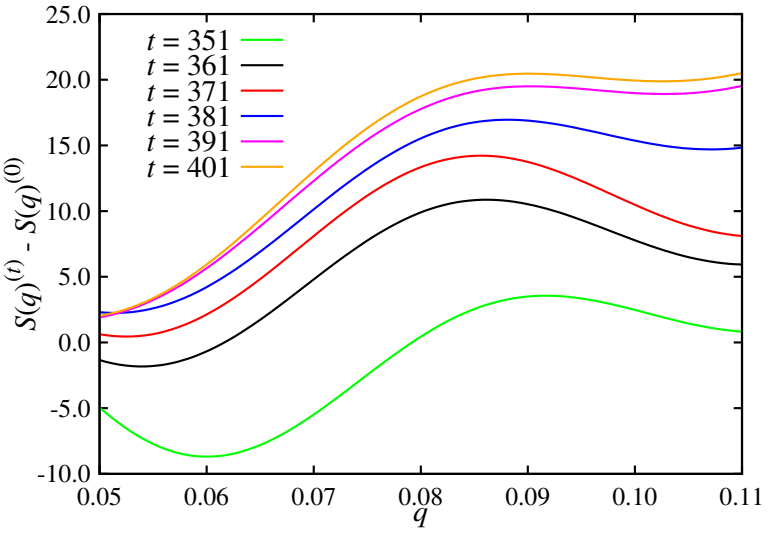

Figure 2.4. Time evolution of the structure factor of a crystallizing linear chain at $T^* = 9$. The position $q_{\max}$ of the peak structure factor corresponds to the distance between the baby nuclei in the linear chain. Some obtained values are negative because they are a difference between the structure factors at time t and time 0, and are simply less correlated as compared to the structures at the beginning of the quench. Data are displayed after smoothening using the csplines function provided by gnuplot. The raw data are provided in Appendix C.

We discuss the results for the linear system crystallized at $T^* = 9$, the ring polymer crystallized at $T^* = 9$, and the ring polymer crystallized at $T^* = 7.79$.

2.3.3.1 Linear Polymer

Figure 2.4 shows the baseline-corrected structure factor for the crystallization of the linear chains at very early times immediately after the quench. We obtain a scattering peak at $q_{\max} = 0.08585 r_0^{-1}$, corresponding to a length scale of $73 r_0$ in our simulations. We find from our simulations that this corresponds to the separation between the baby nuclei of Figure 2.1. The position of the peak is almost invariant with respect to time in this early stage. This means that for these times, the distance between the baby nuclei is not changing. Therefore, the baby nuclei are reeling in monomers from the connector one-by-one. This peak in the structure factor has been found in our previous simulations[7] and is the accepted explanation for the existence

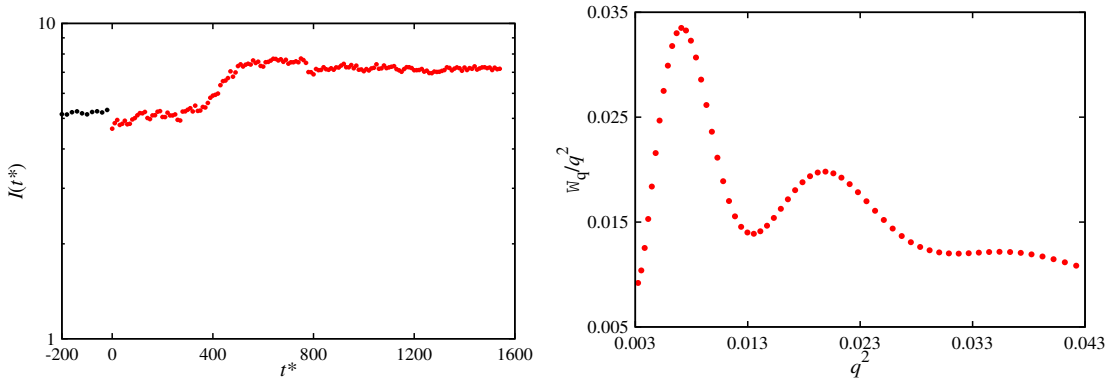

Figure 2.5. Exponential growth of intensity (a) and wave vector dependence of growth rate (b) for linear chains at $T^* = 9$. The total scattering intensity I increases exponentially after $t^* \sim 400$ for the linear chain. The weak increase in the total scattering intensity I of the linear chain preceding the exponential rise at $t^* \sim 400$ matches the total scattered intensity of the uncrystallized state prior to quenching, as shown in (a) by the points in black. The wave vector dependence of Ω_q does not show any signature of spinodal decomposition mechanism.

of the peak in structure factor in the small angle X-ray scattering profiles of Imai and co-workers[56, 57, 66, 68].

We have computed the total integrated intensity I for the duration of crystallization studied. Figure 2.5 shows the total integrated intensity exhibiting the typical behavior as observed in experiments. We can see from the figure that the intensity increases exponentially after $t^* \approx 400$. This particular feature is in accordance with the experiments of Imai and co-workers[56, 57, 66, 68]. The weak dependence preceding the exponential increase in the total intensity has also been found in some other experiments[69].

At earlier times ($t^* < 400$), the total scattered intensity is only weakly dependent on time, as seen in Figure 2.5a. In order to understand this feature, we have computed the structure factors $S(q)$ upto 200 time instances before the crystallization is begun. Once the structure factors are obtained, we integrate the structure factors to compute the total scattered intensity before quenching. This is shown in Figure 2.5a, with

the intensities before the quenching indicated in black. As is seen from the figure, the intensities at very early times appearing before the exponential rise are found to correspond to that of the molten state prior to crystallization. Therefore, for $t^* < 400$, the chain is in the uncrystallized state.

In order to explore the suggestion in the literature of a possible spinodal decomposition mechanism[57, 66, 68] for polymer crystallization, we have computed the rate of growth of fluctuations Ω_q from the structure factors and the ratio $\frac{\Omega_q}{q^2}$ as shown in Figure 2.5. A linearly decreasing $\frac{\Omega_q}{q^2}$ would have indicated the existence of spinodal decomposition. But Figure 2.5b clearly shows a non-spinodal mechanism between $q^2 \approx 0.003$ and $q^2 \approx 0.013$ in accordance with the work of Muthukumar and Welch[7].

2.3.3.2 Ring polymer

As has been computed for the linear polymer, we have studied the early stage crystallization for the ring polymer as well by computing the static structure factor at various times immediately after the quench, as given by Equation 2.11. The first case that we investigate is the crystallization of the ring polymer at the same crystallization temperature T_c of the linear chain of $T^* = 9$. We similarly correct for the amorphous region by subtracting the structure factor at the onset of crystallization from the structure factor calculated at each time. Our scattering results are shown in Figure 2.6a. The scattering peak appearing at $q = 0.0393$ (length scale of $160r_0$) has been found to correspond to the separation between the two adjacent baby nuclei. We observe that in the case of the crystallization of the ring, there are several different baby nuclei formed along the chain connector. Since the structure factors are computed as an ensemble average from 100 chains just like the one in Figure 2.1b, a clearly distinct number of smaller baby nuclei along the connector cannot be deduced from Figure 2.6a alone. Additionally, the amplitude of the structure factor at the

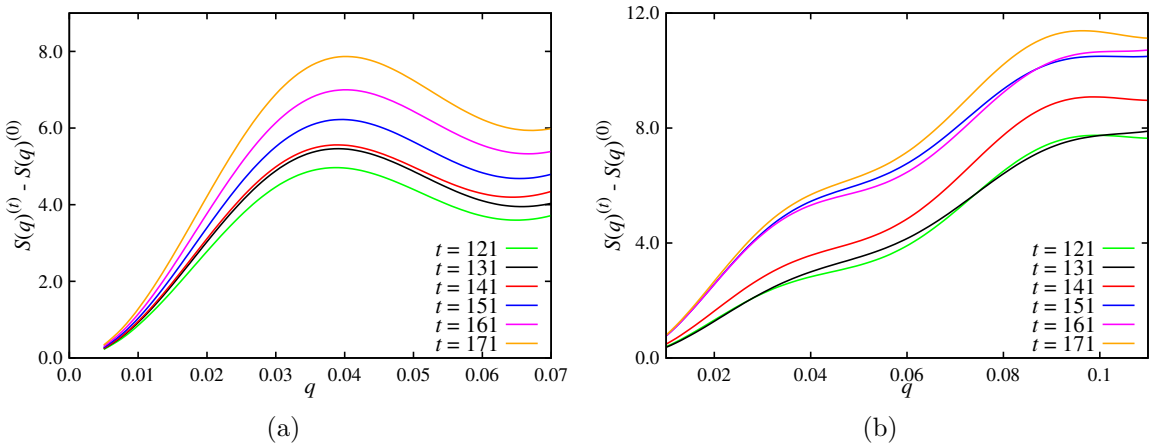

Figure 2.6. Scattering profiles for the crystallization of the ring polymer at (a) $T^* = 9$ and (b) $T^* = 7.79$. The scattering peak at $q \approx 0.04$ in the case of the ring polymer crystallized at $T^* = 9$ corresponds to the distance between the primary baby nuclei of Figure2.1b. Data are displayed after smoothening using the csplines function provided by gnuplot. The raw data are in Appendix C.

$q_{\max}$ value is far less for the ring polymer than for the linear polymer as shown in Figure 2.4, indicating that structural ordering among the baby nuclei of the ring is not as prominent as in the case of the linear polymer.

We integrate the structure factors according to Equation 2.12 to obtain the total scattered intensity as a function of the crystallization time. Figure 2.7a shows the total scattered intensity during the crystallization of the ring chain. A comparison with the total scattered intensity during the crystallization of the linear chain shows that the intensity of the ring polymer rises more exponentially and reaches the plateau much faster than the linear polymer. We can conclude from the computed total scattering intensities that the single ring polymers crystallize much faster than the single linear polymer in this regime of primary nucleation. This conclusion is in good qualitative agreement with several experiments, which also find that the nucleation of the ring polymer is much faster than that of the analogous linear polymer of the same molecular weight, when crystallized at the same temperature[37]. This rapid

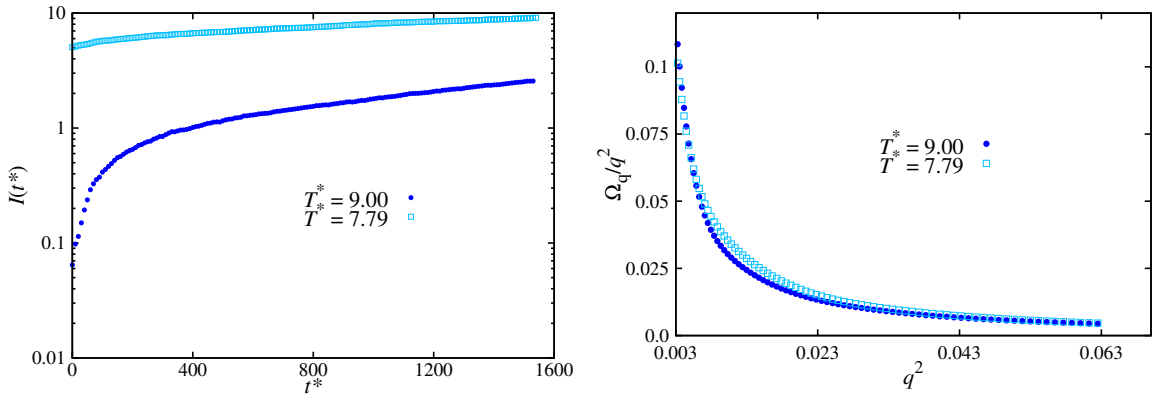

(a) (b)

Figure 2.7. (a) Growth of intensity and (b) wave vector dependence of growth rate for ring polymers. The integrated intensity during the crystallization of the ring polymer at the same crystallization temperature ($T^* = 9$) and at the same degree of undercooling ($T^* = 7.79$) indicates that the intensity rises exponentially to a plateau. The wave vector dependence of the growth rate as shown in (b), which indicates the coarsening kinetics of the ring polymer, shows the absence of spinodal decomposition.

nucleation can be attributed to the compactness of the ring polymer in comparison with its linear analog.

In an effort to understand the effect of chain topology on the mechanism of crystallization, we have computed the rate of growth of fluctuations Ω_q at different values of the scattering wave vector q from the exponential fits of Equation 2.13. $\frac{\Omega_q}{q^2}$ is then plotted against the value of q^2, as shown in Figure 2.7b. As seen from the figure, $\frac{\Omega_q}{q^2}$ is not linear with q^2 at both $T^* = 9$ and $T^* = 7.79$. As in the case of the linear chain, there is no evidence for the spinodal decomposition mechanism. The coarsening kinetics of a collection of baby nuclei is highly correlated and the pathway for this is distinctly different from that of the linear chain, as is evident from a comparison between Figure 2.5b and Figure 2.7b.

To understand this early stage mechanism of the crystallization of ring polymers better, we study the "induction phase" at a temperature corresponding to the case of equal degree of undercooling $\Delta T \left(= T_m^0 - T\right)$, where the T^* is now 7.79. We compute

the structure factors from 30 different trajectories and correct for the baseline by subtracting the structure factor at $t^* = 0$. Figure 2.6b shows the baseline-corrected structure factors. We observe a peak at $q = 0.0965$ (length scale of $65l_0$), which corresponds to the separation between the baby nuclei of the ring polymer. The position of this peak stays invariant with time. The peak in the case of crystallization at equal ΔT is much wider than that in the case of crystallization at equal T_c, indicating that there is far less structural uniformity in the baby nuclei formed.

Figure 2.7a shows the computed values of the total scattered intensity as a function of time. We see clearly that there is a non-exponential rise in the intensity just after time $t^* = 0$. Following the initial rise, the intensity then almost reaches a plateau. This shows that the crystallization at $T^* = 7.79$ is even faster than the crystallization at $T^* = 9$.

We then proceed to understand the early stage mechanism of this crystallization at equal degree of undercooling by studying the wave vector dependence of the growth rate of fluctuations Ω_q. Figure 2.7 shows the ratio $\frac{\Omega_q}{q^2}$ plotted against q^2. As in the case of linear chains, the fastest growing mode is at a finite q ($\neq 0$), because Ω_q/q^2 is a decaying function of q^2 so that Ω_q is a maximum at a non-zero value of q. However the coarsening kinetics of a collection of baby nuclei in rings is distinctly different from that of the linear chain and shows no evidence of the spinodal decomposition mechanism. This change in mechanism between ring and linear systems is therefore driven purely by chain topology.

2.3.4 Lamellar thickness

We have calculated the lamellar thickness L by calculating the principal radii of gyration of each available crystal. To calculate this, the positions of the particles are first translated to the frame of reference of the center of mass of the crystal. From this center of mass reference frame, the moment of inertia tensor is constructed and

its eigenvalues give the three principal radii of gyration of the crystal. As seen from the general shape of the crystals shown in Figure 2.1, the largest radius of gyration corresponds to the length scale along the axis corresponding to the lamellar thickness of the crystals. We use this largest radius of gyration as the measure L of the lamellar thickness.

Once this measure L of the lamellar thickness is obtained, we then estimate the Helmholtz free energy $F(L)$ as

$$F(L) = -k_B T \log\left(\frac{n(L)}{\mathcal{N}}\right). \tag{2.14}$$

In this equation, $n(L)$ is the number of crystals with a lamellar thickness between L and $L + \Delta L$ and $\mathcal{N}$ is the total number of crystals analyzed by this algorithm. Then a free energy landscape is constructed by compiling all these lamellar thicknesses into a histogram discretized along the lamellar thickness L, as described by the method of Kumar and co-workers[70]. These free energy estimates were constructed by taking averages from 100 simulations, with every simulation sampling 20000 crystals, after ensuring that all the polymers formed completely chain folded structures.

Figure 2.8a and Figure 2.8b illustrate the free energy landscapes for linear and ring polymer chains of 700 monomers, crystallized at the same temperature of $T^* = 9$. Each free energy well corresponds to a different number of stems within the single crystal. Here, the bin size ΔL is $0.25 l_0$. We observe that the global minimum of both free energy landscapes is at $L = 12.0$. Since the number of monomers in each polymer is equal, we can conclude that the global minimum corresponds to the same number of monomers per stem, although the ring polymer crystal will have at least one additional fold by virtue of its closed topology. We additionally find that there is a broad region of free energy minimum for the linear chain between $L = 10$ and $L = 14$, with a small free energy barrier separating the minima at $L = 12$ and $L = 14$. We therefore expect that the chains can frequently 'melt' to rearrange between these

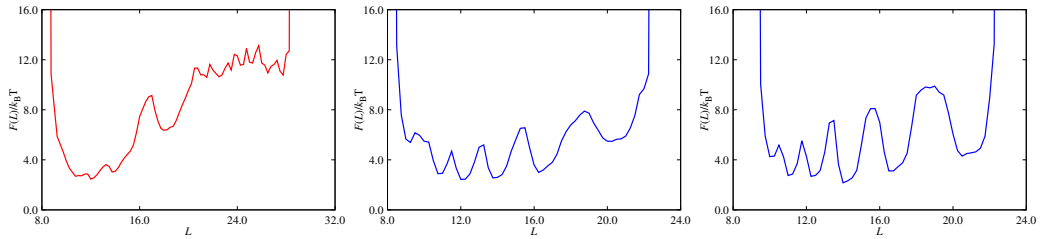

(a) (b) (c)

Figure 2.8. Free energy landscape in terms of lamellar thickness for (a) linear polymers at $T^* = 9$, (b) cyclic chains at $T^* = 9$ and (c) cyclic chains at $T^* = 7.79$. The ring polymer has several distinct lamellar thicknesses into which it can crystallize, whereas the linear polymer does not crystallize into as many distinct lamellar thicknesses at $T^* = 9$. The crystallization of the ring and linear polymers at equal supercooling shows that it is more difficult for the ring polymer at $T^* = 7.79$ to anneal to different lamellar thicknesses than at $T^* = 9$.

two minima. Above $L = 20$, we find several regions of local minima frustrated by free energy barriers. On the other hand, we find that the ring polymers can crystallize into several different minima, which are separated by large free energy barriers. These deep wells make it difficult for a crystal to anneal to a different lamellar thickness. Moreover, the number of stems that can be formed by a ring crystal will always be an even number because of the topology of the chain. We can clearly see free energy wells around even lamellar thicknesses in Figure 2.8b (and Figure 2.8c). Additionally, ring polymers do not favorably crystallize into lamellar thicknesses greater than 22 units, whereas the linear polymer can crystallize into lamellar thicknesses larger than 22 units. This behavior of the lamellar thickness is yet another example of the sensitivity of equilibrium crystallization states to the topology of the original polymers[71].

While this study represents the crystallization of a single linear polymer and a single ring polymer, an appropriate comparison of both crystallization processes can only be accomplished when the temperatures of crystallization are appropriately chosen. The lamellar thickness for a polymer crystal is given by[43]

$$L = \frac{C_1}{\Delta T} + C_2. \tag{2.15}$$

An appropriate comparison between the two systems can be made when the degree of supercooling $\Delta T \left(= T_m^0 - T\right)$ is equal. We have therefore computed the free energy landscape with respect to the lamellar thickness, by crystallizing the ring polymer at a temperature equal to $T^* = 7.79$. An estimate of the free energy landscape for the crystallization of the ring polymer at $T^* = 7.79$, to compare to the crystallization of the linear polymer at $T^* = 9$ is given in Figure 2.8c.

From the free energy landscapes shown in Figure 2.8c, we can observe that there is a shift to higher lamellar thickness with a decrease in the temperature of the ring system. The free energy wells for the lamellar thickness are much deeper in this case as compared to the crystallization of the ring polymer at $T^* = 9$, which arises because of a lack of thermal energy in the system owing to the lower crystallization temperature. We also observe a clear shift in the most probable lamellar thickness from $L = 12$ in Figure 2.8b to $L = 14$ in Figure 2.8c. This is remarkable as it shows that the ring prefers to crystallize into a larger lamellar thickness, in spite of being crystallized at a lower temperature. Ring polymer crystals forming thicker lamellae have also been observed experimentally by Su and co-workers[27] in the case of poly(ϵ-caprolactone) crystals and also by Shin and co-workers[34] in the case of poly(L-lactide), although the opposite has also been observed by Sugai and co-workers[39].

2.3.5 Monomer diffusion

In an effort to explain the various features seen in the crystallization of the ring polymer, it is of interest to understand the effect that the lack of chain ends bring to the behavior of the monomers. To understand the motion of the monomers inside the single crystal, we have studied the mean squared displacement of a single monomer ($\langle(\mathbf{R}_s(t) - \mathbf{R}_s(t+\tau))^2\rangle$) averaged across several simulations, where $\mathbf{R}_s$ is the position of the monomer.

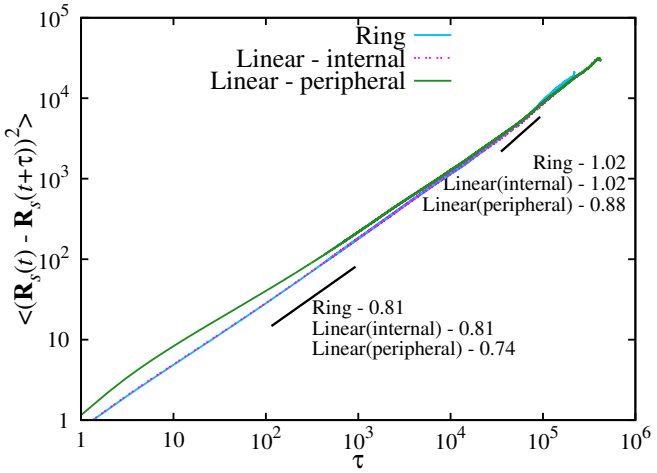

Figure 2.9. Mean squared displacement for different types of labeled monomers in linear and ring polymers. The cyan curve shows the mean squared displacement of a labeled monomer of the ring polymer, the magenta curve shows the mean squared displacement of a monomer close to the middle of the linear polymer, while the green curve shows the mean squared displacement of a monomer near the periphery of the linear polymer. The motion of monomers in the ring polymer is similar to that of the internal monomers of the linear polymer. However, the peripheral monomers of the linear chains diffuse much slower.

We take an average across 30 different simulations, each running up to at least $t^* = 300000$. The linear polymer was crystallized at $T^* = 9$, while the ring polymer was crystallized at $T^* = 7.79$. Figure 2.9 illustrates that there are two different power law regimes in each system. Different theories predict different values of the exponent[62]. We find that at long times, the monomer diffusion is reminescent of Einsteinian diffusion ($\langle(\mathbf{R}_s(t) - \mathbf{R}_s(t+\tau))^2\rangle \sim t$) of a Brownian particle. At shorter times the diffusion of the labeled monomer is sub-diffusive, with $\langle(\mathbf{R}_s(t) - \mathbf{R}_s(t+\tau))^2\rangle \sim t^{0.8}$, which is between the Rouse regime ($\langle(\mathbf{R}_s(t) - \mathbf{R}_s(t+\tau))^2\rangle \sim \sqrt{t}$) and that of Einsteinian diffusion ($\langle(\mathbf{R}_s(t) - \mathbf{R}_s(t+\tau))^2\rangle \sim t$). From Figure 2.9, we conclude that the dynamic behavior of the monomers inside the crystals for linear and cyclic chains is identical.

While the internal monomers in the linear and ring polymers have similar behavior as expected, an unusual behavior is seen near the end of the linear chain.

This is shown in Figure 2.9 by the solid green curve, which is the mean squared displacement of the 5^{th} monomer of the linear chain. Here we can see that the monomer diffuses over larger distances at small times, while its displacement is similar to that of the internal monomers at larger times. An analysis of the exponent of the time reveals some unexpected features. At short times, the monomer diffusion seems to be in between the two regimes of Rouse and Einstein, with an even smaller exponent ($\langle(\mathbf{R}_s(t) - \mathbf{R}_s(t+\tau))^2\rangle \sim t^{0.74}$) than that of the internal monomers. At larger times, the mean squared displacement approaches the Einstein regime ($\langle(\mathbf{R}_s(t) - \mathbf{R}_s(t+\tau))^2\rangle \sim t$) by reaching an exponent of 0.88 until $t = 417000t^*$. This finding implies that the timescales followed by the peripheral monomers are different from those of the internal monomers of either type of chain, in spite of the chains undergoing crystallization.

2.3.6 Secondary nucleation

Secondary nucleation represents the regime in which an already formed polymer crystal grows. A lot of the modeling contributions have focused on this regime, and the most dominant theory has been the multiple free energy barrier theory of Lauritzen and Hoffman[2]. Apart from this there also exist some other theories, which have been reviewed by Armitstead and Goldbeck-Wood[72], and the most recent entropic barrier theory[73]. In their theory, Lauritzen and Hoffman assumed that the addition of a stem onto an existing growth front is confronted by a free energy barrier and its crossing is then followed by a trough. Although there are several advantages of this theory, there are also several theoretical discrepancies[72] and experimental findings (reviewed by Strobl[74]) which cannot be explained using it. Apart from these, Welch and Muthukumar[49] have shown in their simulations that there is no free energy barrier for the addition of linear chains to an existing nucleus made of linear chains, under the conditions of the Lauritzen-Hoffman Theory [2].

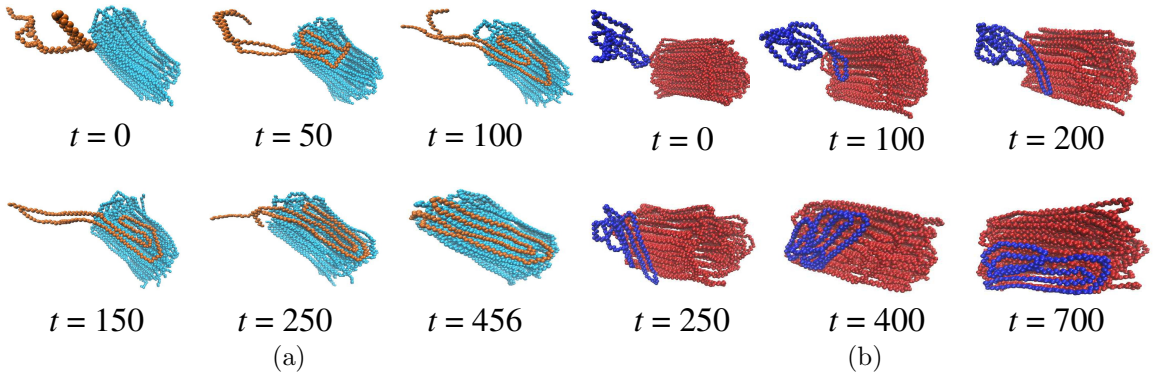

Figure 2.10. The evolution of secondary nucleation in (a) linear and (b) ring polymer chains. The ring polymer chain struggles to orient itself according to the crystal's stem orientation before adsorbing on to it.

We have studied secondary nucleation in the case of both ring and linear polymers. To model this, we have chosen already equilibrated polymer chains made of 200 monomers and we position them close to an existing pre-formed crystal. It is important to note the nature of the intermolecular Lennard-Jones potential in this case, where the equilibrium distance parameter σ between molecules of different chains is 4.53 Å. We bring a chain equilibrated at the higher temperature of $T^* = 12$ close to an existing crystal. We then allow the chains to equilibrate at their respective crystallization temperatures for 5000 time units. For the linear polymers, the crystallization temperature is $T^* = 9$, while the crystallization temperature for the ring polymers is $T^* = 7.79$, in accordance with the condition of equal degree of supercooling ΔT. If the equilibrated chain is brought close enough to the crystal, then it adds on to the crystal, which acts as a growth front. Then, another chain consisting of 200 monomers is brought close to this larger crystal. If the polymer crystal grows, then the simulation is accepted, but if the equilibrated chain simply crystallizes onto itself, then the run is rejected. In this process, we successively add 20 chains to existing crystals and our final crystals consist of up to 4000 monomers.

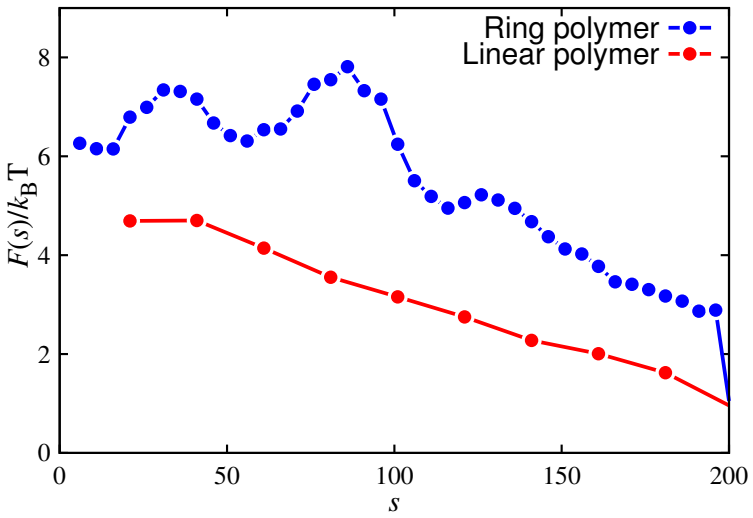

Figure 2.11. Free energy landscape at the growth front. The process of secondary nucleation in the ring and linear polymers at equal degrees of supercooling shows that there are several barriers for the addition of the ring polymer onto an existing crystal, while the linear polymer adsorbs on without any energy penalties.

A typical example of this process is shown in Figure 2.10, in which we show the addition of the 20^{th} chain onto a crystal made up of 19 chains, each consisting of 200 monomers. In the case of the linear chain, the chain approaches the crystal in an almost extended configuration, following which, each monomer attaches itself sequentially to the crystal. The linear chain is not constrained topologically, which ensures its swift addition onto the crystal. However, in the case of the ring chain this process is not so straightforward, as seen in Figure 2.10b. The ring approaches the crystal in its crumpled state and begins attaching on to the crystal monomer-by-monomer. But to orient itself correctly according to the crystal, it explores several configurations before a configuration acceptable to the crystal is reached, and only then does it add on correctly. This means that there are several barriers arising from configurational entropy in the process of the addition of the ring polymer onto an existing crystal.

To quantify the process of secondary nucleation, we modify the previous histogram-based technique[70] that we employed to study the lamellar thicknesses, where the number of monomers that have added to the growth front (s) is the secondary nucleation coordinate. We consider a monomer to be added to the growth front if it is within a certain distance from the closest monomer of the crystal. Using this metric, we count the number of monomers that have added to the crystal and then calculate the Helmholtz free energy as

$$F(s) = -k_B T \log\left(\frac{n(s)}{\mathcal{N}}\right) \tag{2.16}$$

where $\mathcal{N}$ represents the total number of snapshots sampled and $n(s)$ represents the number of monomers added to the growth front. Then, a free energy landscape is constructed by compiling all these monomers adding to the growth front, discretized using a large bin size of 20 monomers. This method has been devised to compute the free energy landscape for any dynamic process that has an order parameter to describe its evolution[70]. As mentioned earlier, we construct our free energy landscape after averaging over 20 simulations in which a chain is successively added to an existing nucleus, in accordance with the method used by Welch and Muthukumar [49]. Our free energy estimates are shown in Figure 2.11. As has been observed earlier for the case of the linear polymer[49], there are no significant barriers in the free energy of chain addition, which is in sharp contrast to one of the assumptions of the Lauritzen-Hoffman theory. On the other hand, there are significant barriers seen for the secondary nucleation of the ring polymers, at the initial stages of the chain addition. We attribute these barriers to the energy required by the adsorbing ring polymer to orient itself along with the stems of the crystal. This energy penalty does not exist in the equilibrated linear chain owing to its unfolded nature. The ring polymer faces a difficulty in annealing, as seen in Figure 2.8b and Figure 2.8c, which manifests itself as a free energy barrier during chain addition as well.

2.4 Conclusions

We have examined the crystallization behavior of a model ring polymer system and we have compared this to the crystallization of a linear polymer of equal chain length. We have chosen to do this using Langevin dynamics simulations on a coarse-grained molecular model. This model is generated after making modifications to an earlier model that represented polyethylene[61], representing a generic model polymer. Using this, we have investigated several features of single polymer crystals, namely equilibrium melting points, early stage mechanisms, lamellar thickness, monomer diffusion, and free energy landscape for crystallization.

Our results show that single ring polymers have equilibrium melting points which are about 68°C lower than analogous single linear polymers, which is in qualitative agreement with several experimental findings and in disagreement with several others. According to the prediction from equilibrium thermodynamics, the equilibrium melting point T_m^0 is inversely related to the entropy of fusion ΔS between the solid and liquid phases. The bonding of the terminal atoms of a linear chain results in fewer accessible microstates, and therefore, lesser absolute entropy for the ring chain. This argument has been used by several authors to justify the linear chain having a lower equilibrium melting point than the ring chain of similar molecular weight. However, this does not explain the findings of other authors who have reported that the ring polymer melts at a lower temperature than linear polymers. The diverging conclusions from experiments arise mainly from chemical aspects of the polymer and impurities in the system. Our simulations address only the consequences of chain topology. Our results, which are for model systems devoid of possible interferences from other molecules, have provided insight into this contentious issue. We find that kinetics associated with chain topology controls the crystallization phenomenon instead of the above crude thermodynamic argument.

To investigate the early stage kinetics of the crystallization of single linear and ring polymers, we have calculated the structure factor to reveal more about the intricate processes occurring during the 'induction' phase of the crystallization. We have found that for the linear polymer there is the existence of a distinct peak at $q_{\max}$, which corresponds to the average separation distance between two baby nuclei formed by the linear chain immediately after quenching. A similar feature has also been observed in the crystallization of the ring polymer at the same crystallization temperature, although this is much weaker. An analysis of the total scattered intensity reveals that the ring polymer nucleates faster than the linear polymer at the same temperature, and nucleates even faster when crystallized at the same degree of undercooling.

We have investigated the lamellar thicknesses into which these single linear and ring polymers crystallize. We find that ring polymers crystallize into several distinct metastable lamellar thicknesses as compared to linear polymers, which can crystallize into a small number of lamellar thicknesses. The lamellar thickness distributions of several statistically equivalent polymer crystals reveal that linear polymers can crystallize into very few lamellar thicknesses which can readily anneal into one another, while the topological constraint of the ring polymer makes it require a large amount of free energy for a similar annealing between lamellar thicknesses. This free energy requirement is much higher at lower temperatures, and shows up as larger free energy barriers when the ring polymer is crystallized at the same degree of undercooling as the linear polymer.

In an effort to understand the crystallization behavior of these two systems through the diffusion of the monomers, we have studied the mean squared displacement of various types of monomers. We have found that the mean squared displacement of a monomer far from the end of a linear polymer is equivalent to that of a monomer in the ring polymer. There is a small difference when this comparison is extended to include one of the peripheral monomers of the linear chain. The peripheral monomer

diffuses more initially, while it approaches the diffusion of the other monomers as crystallization proceeds. The time scales of the diffusion of the peripheral monomer and an internal monomer of a polymer are different, which could potentially affect the early stage mechanisms as well.

In addition to these studies on single chains, we have investigated the secondary nucleation of these topologies using the adsorption of polymers onto growth fronts. Computing a free energy landscape along this secondary nucleation coordinate reveals that there is no free energy barrier for the addition of a linear chain. We find that there are several barriers which an adding ring polymer needs to negotiate. We attribute these to the energy required to orient the adsorbing chain to the existing crystal, which is required due to the topological frustration of the ring polymer.

CHAPTER 3

INTERLUDE OF METASTABILITY IN THE MELTING OF POLYMER CRYSTALS

This chapter was published as Iyer, Margossian and Muthukumar, Interlude of metastability in the melting of polymer crystals, *Journal of Chemical Physics* **151**, 124903 (2019).

3.1 Introduction

Consider a crystal made of low molar mass simple molecules. Upon heating this crystal to a temperature above the equilibrium melting temperature, the crystal melts spontaneously. This spontaneous melting behavior is not common for semicrystalline polymers. The non-spontaneity of melting of polymers is widely recognized to arise from free energy barriers for melting [75–77]. It is reasonable to expect free energy barriers for melting of polymers, due to conformational correlations associated with the loss of crystalline order for temperatures below the equilibrium melting temperature. However, for temperatures higher than the equilibrium melting temperature, the origin of non-spontaneity of melting remains to be fully understood. In general, the melting of semicrystalline polymers is a process that has been investigated far less than its opposite process of crystallization. Along with its relevance to technological applications, understanding the process of melting of a tightly bound crystal is key to uncovering several long-standing mysteries in the field of polymer crystallization, such as the memory effect of the melt temperature on the crystallization shown experimentally[78–93]. The melting of a homopolymer crystal represents the unraveling of the simplest macromolecule, which fundamentally represents the competition

between thermal forces and the conformational entropy of polymers. Understanding how such crystals melt could also significantly impact our knowledge of several diseases like Alzheimer's, which are commonly known to be caused due to misfolding of proteins[94, 95], as they are the complicated counterparts of homopolymers.

The process of melting was historically studied using inferences drawn from X-ray scattering[96, 97], which seemed to indicate that melting occurred from the surfaces of crystalline lamellae in both melt-crystallized as well as solution crystallized polymer crystals. More recently, with the availability of several more advanced techniques, attention has shifted to the processes that occur during the melting itself. Barham and Sadler[98] first showed through neutron scattering that the melting of polyethylene single crystal mats results in an almost "explosive" change to a random coil structure, with the radius of gyration changing by 5 nm/s. The time taken for this change in size was observed to be on the order of seconds and independent of molecular weight. In a later publication[99], Barham showed that this melting time is uncorrelated to the relaxation time of individual molecules.

With the development of differential scanning calorimetry (DSC), several experimentalists then focused on the energetics and kinetics of melting[100]. The use of sinusoidal temperature modulation[101] in several experiments indicate that partial melting is reversible up to a certain degree[102–104]. This indicated a preference for the melting to occur, along with keeping a nucleus intact on to which the partially molten parts could recrystallize back, without needing to overcome a free energy barrier. Further, Hu and co-workers[105] extended this idea to show that this reversibility in melting is dependent on the ability of the polymer to carry out a sliding diffusion. Later, it was believed that there could be an activation barrier in the melting kinetics of polymer crystals[75, 106], which was attributed to the entropic barrier due to pinning[76].

Several authors have also tried to observe the melting process by annealing different polymers using Atomic Force Microscopy. An overwhelming majority of works indicate that melting begins from the edge of the single polymer crystal[107]. Some other authors report stepwise unfolding[108] and crystal thickening when observing the melting of oligomers[109] and ultra high molecular weight polyethylene[110]. Several experiments reported that the melting of single polymers caused several cavities to appear[111–115]. Later, Hobbs showed that the parts of the crystal which were crystallized at lower temperatures melt before the material in confined geometries, followed by the rest of the lamellae from the edges inward[116]. This is the reverse of the sequence during crystallization, where thick crystals form first before thin crystals. This was observed separately by Dubreuil and co-workers as well[117]. Sequential melting in different sectors of polyethylene single crystals have been observed as well[118, 119].

While the most of experiments have focused on single crystals, the study of highly concentrated systems have also yielded several insights into the mechanism of melting. In their work, Rastogi *et al.*[120] showed that there is a long-lived heterogeneous state that is formed when ultra high molecular weight polyethylene is melted, which they argued was formed because of restricted reptation due to a heterogeneous distribution of entanglements. In a subsequent work[121], they showed that there are two possible mechanisms of melting depending on the presence or absence of entanglements, correspondng to different bundle sizes of chains that detach from the crystal. The analysis however, was complicated due to an annealing process below the true melting point of 141°C. Later, Lippits and co-workers[122] showed evidence for important processes occuring before the melting point is reached. Rastogi and co-workers[123] then followed the melting of chains using solid state NMR experiments, and argued that adjacently re-entrant domains melt at lower temperatures and clusters of chains melt at higher temperatures, resulting in two types of structures depending on whether

melting happens fast or slow. Yao et al.[124] then showed that the entropic differences between the crystalline and amorphous parts of semicrystalline polyethylene could decide the diffusion of chains during melting. Pandey and co-workers[125] then observed the melting temperatures (T_m) of entangled and unentangled polyethylene and clearly showed increasing melting temperature with heating rate. This was attributed to a lag arising out of instrumental measurement constraints. However, as mentioned earlier, Toda *et al.*[75, 76] found an increase in melting temperature with heating rate. This observation was after accounting for instrumental deficiencies. This indicates the possibility of activation barriers being present during melting.

Recently, with the development of fast-scan Differential Scanning Calorimetry (DSC)[126], crystals have been melted at very high heating rates ($\sim 10^5$K/s). This meant that the crystals which were formed at lower temperatures and were susceptible to reorganization at lower melting temperatures no longer reorganize before the other parts. The artificial increase of the melting point due to this reorganization can be avoided, and the true nature of melting can be elucidated[127]. In one such work, Toda and co-workers suggested the existence of activation barriers during melting[128].

Several of these experimental findings have been accompanied by theoretical and simulation calculations as well. Using Kinetic Monte Carlo simulation of melting of a single molecule crystal in a simple cubic lattice, Hu and co-workers[129, 130] argued that the free energy barrier for melting is the reverse of that for crystallization. In their simple model, only parallel polymer bonds are subjected to an attractive interaction (with effective energy E_p) and all the other significant features such as the trans-gauche conformational states and polymer-polymer, polymer-solvent and solvent-solvent interactions are ignored. Based on this model, they showed that a first-order phase transition occured at the melting temperature of 3.125 E_p/k_B, where k_B is the Boltzmann constant. They then addressed the issue of free energy barriers for three temperatures below this phase transition temperature of 3.125, namely,

2.941, 2.967, and 3.030 in units of E_p/k_B. The barrier at the temperature of 3.030 is about 25 k_BT. Such high barriers would result in enormously long times for melting, which is unseen in experiments. The key conclusion from this simulation work is that there is a high barrier for melting. Most importantly, the focus of the work has been at temperatures below the equilibrium melting temperature[130]. The analysis at the different temperatures has been complicated because of discrepancies in the determination of the equilibrium melting temperature between their actual simulation data and the post analysis of their data in constructing the free energy profile. Furthermore, such large barriers are estimated using the total system without explicit considerations of an order parameter, such as the global order parameter of Liu et al.[48] or Welch et al[49]. This has hidden the nature of melting much above the melting temperature of the polymer. Furthermore, in the above work and a subsequent publication[130], Hu and co-workers treat the free energy landscapes of melting and crystallization to be the reverse of one another, with a single barrier in the free energy landscape. On the other hand, the pathway of crystallization into the final semicrystalline state of global free energy minimum consists of multiple entropic barriers[53, 54], and the reverse process is likely to follow a different set of entropic barriers. Additionally, it is important to note that the free energy barriers of $\sim 25k_BT$ are at temperatures below the melting point of the polymers. Moreover, a recent theory from the recrystallization of once-molten crystals invokes the presence of long-lived metastable states during the melting of a polymer[77] and explains several experimental findings[74, 81–85, 92] using such states.

The goal of this thesis chapter is to gain insight into the molecular basis of the non-spontaneity of polymer melting even at temperatures above the equilibrium melting temperature. To understand this, we study the melting process by use of Langevin dynamics simulations. Using our molecular model[7], which is derived after making modifications to another model that essentially reproduces several thermophysical

properties of polyethylene[61], we estimate the free energy landscapes using parallel tempering Langevin dynamics simulations along a new local order parameter, which serves as a reaction coordinate. We study two separate systems: single chain, and multi-chain crystal, and show the kinetics of melting in both systems. We show that both single crystals and multi-chain crystals pass through a globular metastable state at lower melting temperatures, before forming more expanded random coil-like structures at higher melting temperatures, which for the latter system results in individual chains peeling off the crystalline core. For the multi-chain crystals, we also study melting at temperatures close to the equilibrium melting temperature and show the existence of long-lived metastable states of partial order. We estimate free energy landscapes using parallel tempering simulations and show the existence of a metastable state during the melting of both systems. For single chain melting, we show one free energy barrier, while for multi-chain melting, we show two free energy barriers. Our work highlights the melting behavior of polymers in an ideal case, where all the monomers are subjected to the same temperature upon melting, within statistical fluctuations of the Langevin thermostat. The paper is organized as follows: in section II, we describe the simulation model and the sampling procedure; in section III, we discuss our findings from the simulations.

3.2 Simulation Model and Methods

The details of the simulation method can be found in the previous chapter in Section 2.2. We describe additional computational details below.

In an effort to monitor the ordering of the polymer on a local level, we introduce a new local order parameter in the spirit of Hu et al.[129] and Nicholson et al.[131]. We start from the global order parameter[48, 49, 54, 132],

$$P_2 = \frac{\langle 3\cos^2\theta - 1\rangle}{2}, \tag{3.1}$$

where θ is the angle between all pairs of orientational vectors $\mathbf{r}_{i+1} - \mathbf{r}_{i-1}$ for any bead i. Then, we modify this global order parameter to define it for each monomer by identifying all the monomers which fall within a cut-off radius. The cut-off radius is set at 6.5 (10.01Å), in keeping with the distance at which the Lennard Jones potential U_{LJ} is truncated. Once the monomers are identified, the angles between the orientation vectors of these monomers are then averaged according to Equation 3.1 to give a local value of the order parameter. If this local order parameter exceeds a value of 0.5, then the monomer is designated as a crystalline monomer, and amorphous otherwise. The threshold value has been chosen as 0.5 after making inferences from the structural order parameter values obtained first by Liu and Muthukumar[48]. For the multi-chain crystals, the monomers from all the chains are utilized to generate the orientational vectors, as long as the monomers fall within the cut-off radius. In this manner, we develop a count of the number of amorphous monomers $m_{\text{amorphous}}$ for every timestep, and use this as our order parameter for melting.

To calculate the free energy landscapes for the melting of single chains and multi-chain crystals, we use the method of parallel tempering along with Langevin dynamics[133, 134] as done earlier by Mahalik and Muthukumar[135]. In the parallel tempering method, there are a certain number of replicas of the system. We run Langevin dynamics with each of these replicas at their prescribed temperatures. Periodically, the information on the configurational details in a replica is exchanged into another replica chosen at random, with an acceptance probability and the system would evolve in the new replica at the new temperature. After an elapse of the swapping time period, the swapping of configurational information is performed into another replica, and this process is continued. We have shown the swapping time period for all simulations in Appendix D. If a state α is chosen to swap with a state β, then the acceptance probability $P_{\alpha\to\beta}$ for this swap is given by:

$$P_{\alpha\to\beta} = \min\left\{1, \exp\left[\left(\frac{1}{k_B T_\alpha} - \frac{1}{k_B T_\beta}\right)\left(U_\alpha - U_\beta\right)\right]\right\}, \tag{3.2}$$

where U_α is the total potential energy of the α^{th} replica, and T_α is the temperature of the α^{th} replica. To ensure that the average kinetic energy in any replica stays at $\frac{3}{2}k_B T$, we re-scale the momentum p of each monomer i of the system following a configuration swap as given by

$$p_i^{new} = \sqrt{\frac{T_{\text{new}}}{T_{\text{old}}}} p_i^{\text{old}}. \tag{3.3}$$

In order to make sure that the energies of replicas overlap sufficiently for Equation 3.2 to be used, we use an evenly spaced temperature grid containing the temperatures $T_c = 9$, $T_m - 0.4$, $T_m - 0.2$, T_m , $T_m + 0.2$, and $T_m + 0.4$, where the melting process has been studied for different melting temperatures T_m of 12, 14, 16, 18, and 20. Here, T_c and T_m are crystallization and melting temperatures, respectively. Additionally, we have also studied the melting of multichain crystals at temperatures of 11 and 11.6 to understand the kinetics close to the equilibrium melting temperature. Mahalik and Muthukumar[135] have suggested other methods to improve convergence. But as the results of the parallel tempering method will show in the next section, convergence was attained using the chosen temperature grid. Therefore, no other temperature grids were utilized. Several crystalline configurations were maintained at $T_c = 9$, and were also part of the sampling scheme so that the system could attempt swaps with crystalline configurations as well. The total number of steps for which the simulation was run for each melting temperature, and the frequencies of the swap step are provided in Table D.1 in Appendix D. The relative free energy contribution of each conformation to the free energy landscape along the melting reaction coordinate $m_{\text{amorphous}}$ is given by:

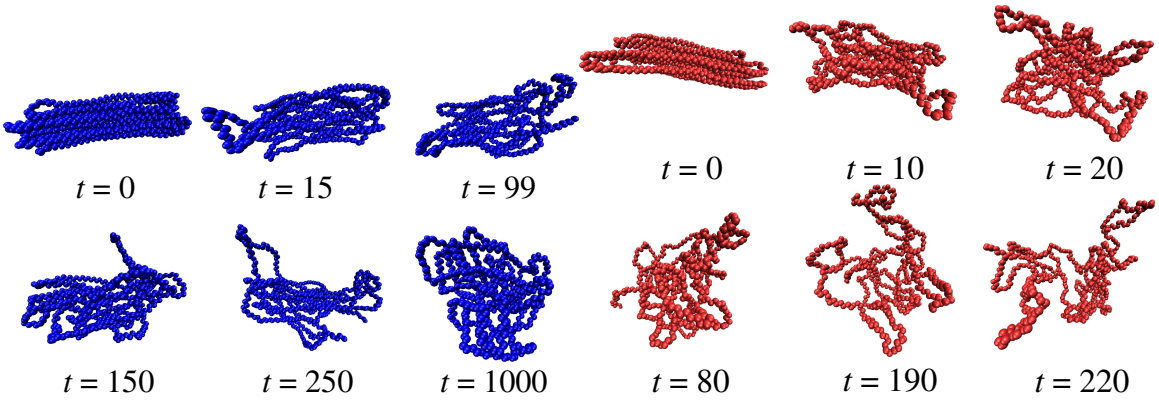

(a) $T^* = 12$ (b) $T^* = 18$

Figure 3.1. Representative snapshots for melting of a single chain from two out of the five temperatures analyzed. The snapshots in (a) depict melting at a temperature of $T^* = 12$, and the snapshots in (b) depict melting at a temperature of $T^* = 18$.

$$F\left(m_{\text{amorphous}}\right) = -k_B T \ln\left(\frac{n\left(m_{\text{amorphous}}\right)}{\mathcal{N}}\right), \tag{3.4}$$

where $n\left(m_{\text{amorphous}}\right)$ represents the number of conformations found that contain $m_{\text{amorphous}}$ number of amorphous monomers, and $\mathcal{N}$ represents the total number of conformations sampled.

3.3 Results and Discussion

3.3.1 Single crystal melting

We first studied the melting of a single polymer crystal consisting of 700 monomers. The crystals were obtained from the crystallization process of linear polymers of $N = 700$ as described in our previous work[132]. Then these crystals were melted isothermally by allowing them to equilibrate at their melting temperatures T_m for several thousands of simulation time units through the use of Langevin dynamics.

The melting process was studied at several different values of T_m. The equilibrium melting temperature T_m^0 was determined in our previous work as 10.74 ± 0.20[132]. To study melting, we chose five different values of the T_m - 12, 14, 16, 18 and 20. As

a reference for our model polymer, the difference between the temperatures of 12 and 10.74 in real units is 71.04 K. The choice of temperatures was made so as to explore the response of the polymer crystals to increasing driving force for melting.

Figure 3.1 shows typical trajectories of melting at two different temperatures, rendered using the Visual Molecular Dynamics Package(VMD)[67]. Figure 3.1a shows a trajectory when the polymer crystal was allowed to equilibrate at $T^* = 12$, which represents a case of weak driving force, while Figure 3.1b shows a trajectory when the polymer crystal was allowed to equilibrate at $T^* = 18$, which represents a case of strong driving force. At low melting temperatures like the one shown in Figure 3.1a, the polymer is found to progressively and uniformly lose its crystalline order throughout the crystal. Once the polymer loses its order, it equilibrates to a dense globule-like structure, until several thousands of Langevin dynamics time units, at which point we end the simulations. However, at higher melting temperatures, it is found that the polymer is able to escape the excluded volume attractions (Lennard Jones attractions) and expand to a coil-like structure, after passing through the dense globule-like state as an intermediate. In essence, the melting process comprises of a step where the chain loses order, and another step where the chain expands. The accessibility of the latter step depends on the temperature.

In order to show the change in size of the polymer with increase in the melting time, we show the ensemble-averaged radius of gyration with respect to simulation time. We have averaged the radius of gyration over 70 simulations. Figure3.2 shows the radii of gyration at different values of T_m. The figure shows that at the temperatures of 12 and 14, the polymer does not expand beyond a certain radius of gyration. In fact, the radius of gyration becomes smaller at the melting temperature of $T^* = 12$ as the polymer changes from an aligned lamella to a globular state. However, at higher melting temperatures, the polymer chain undergoes a transition similar to that discovered by Barham and Sadler[98] using Neutron Scattering. This

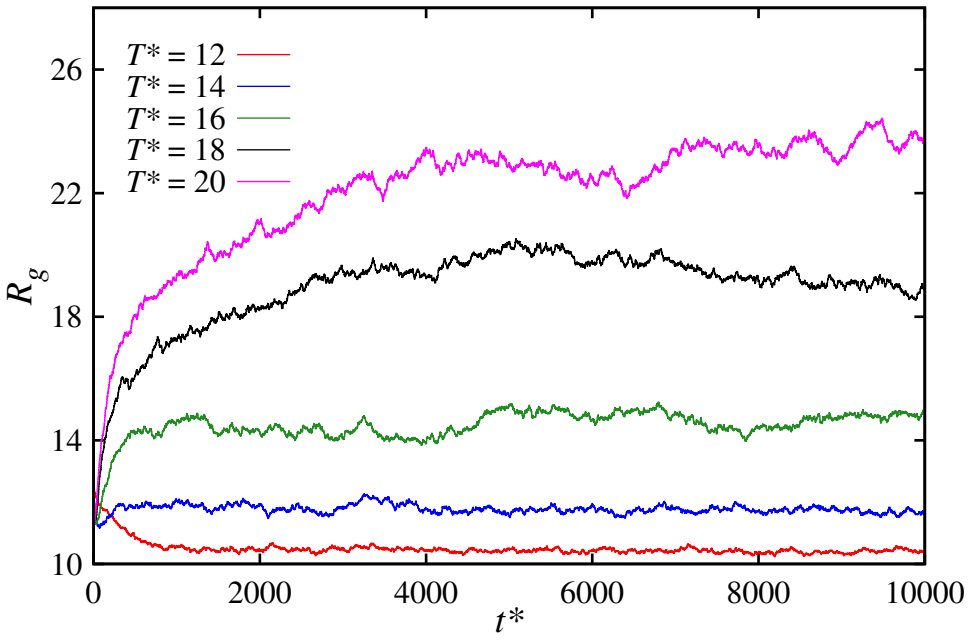

Figure 3.2. Radius of gyration changing with simulation time, when starting from crystalline states for different temperatures. Higher melting temperatures show that the polymer expands to a larger size. At temperatures closer to the equilibrium melting temperature, the radius of gyration even decreases because of the change in shape from an aligned lamella to a globular state. To give a sense of the time scale involved, the Rouse relaxation time for the polymer at $T^* = 12$ is calculated to be 1.49.

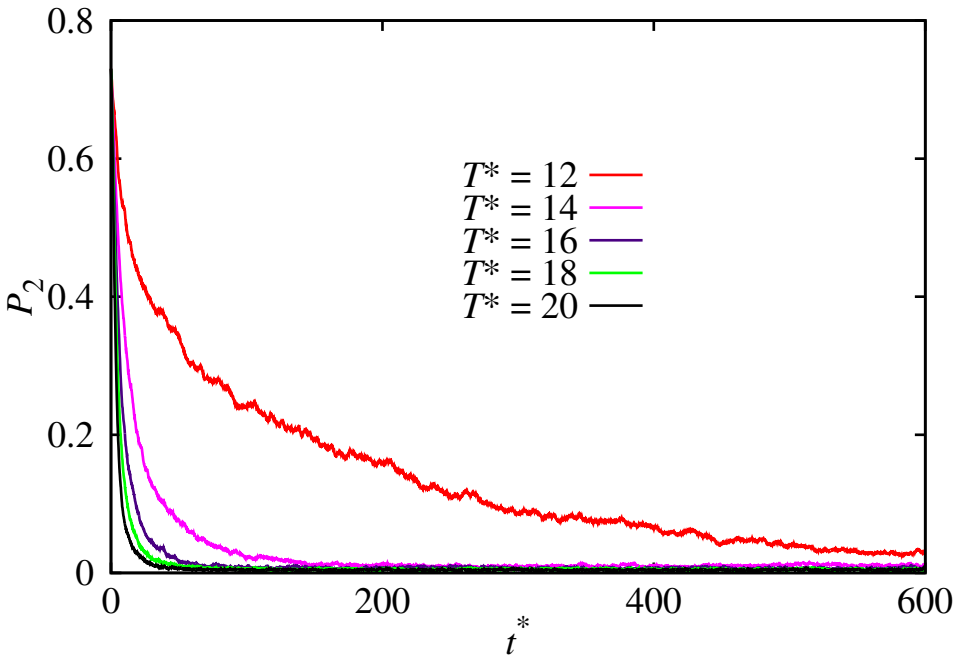

Figure 3.3. Change in the order of the system upon melting as described by the evolution of the global average of the second order Legendre polynomial P_2 with simulation time at different temperatures.

is seen in Figure 3.2, where we can observe a sudden transition in the radius of gyration within a few hundred time units of the beginning of the simulation at the melting temperatures of 16, 18, and 20. It should be noted that Barham and Sadler studied different molecular weights of polyethylene lamellae at 145°C and found the melting kinetics to be independent of molecular weight. An exact mapping of the melting behavior to that of Barham and Sadler[98] is beyond the scope of this work. Nevertheless, our simulation results are in qualitative agreement with the experimental results.

In addition to the change in shape of the polymers upon melting, we also describe the evolution of the crystalline order of the polymers. We describe the crystalline order of the polymer using the global average of the second order Legendre polynomial as described by Equation 3.1. Figure 3.3 shows the evolution of the ensemble-averaged value of P_2 at different T_m. The polymer is seen to lose order rapidly, and an as-

sociated timescale is evident from the figure. We assign the time at which the P_2 first passes a value of 0.1 as the melting time. This choice has been made after the global order parameter values first provided by Liu and Muthukumar[48]. Based on this melting time, we decide the swapping frequency for the parallel tempering with Langevin dynamics simulations to describe the free energy barrier of this melting step. Table D.1 in Appendix D describes the melting time for each of these melting temperatures. Our results, however are independent of this choice of 0.1 for the order parameter. It can be observed from the figure that the rate with which the crystal loses order increases with temperature. We then proceed to study the kinetics of the melting process.

3.3.2 Kinetics of single crystal melting

To quantify the free energy landscape of the melting process, we have performed parallel tempering Langevin dynamics simulations. Parallel tempering ensures that the sampling is not biased towards any particular region in the landscape and that detailed balance is maintained[133, 134].

To perform parallel tempering, we run 6 different Langevin dynamics simulations at 6 different temperatures as described in Section 3.2. This ensures that the sampling has access to all the sections of the $m_{\text{amorphous}}$. The number of simulations, the sampling frequency and the other details of the parallel tempering are shown in Table D.1 of Appendix D.

Using the parallel tempering in such a manner, we have then computed the free energy landscape along the number of amorphous monomers. A value of 0 amorphous monomers corresponds to a completely crystalline system, while a value of 700 corresponds to completely amorphous monomers. As examples, we show structures corresponding to $m_{\text{amorphous}} = 83$ and $m_{\text{amorphous}} = 698$ in Figure 3.4a. The crystalline monomers are marked in blue, while the amorphous monomers are marked

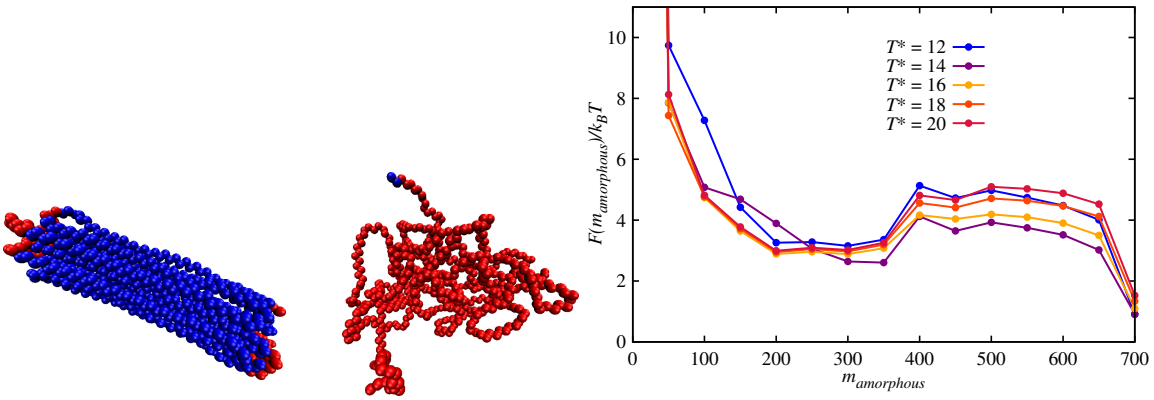

(a) Crystalline and amorphous structures

(b) Free energy landscape

Figure 3.4. (a) Representative structures and (b) free energy landscape for single crystals. (a) shows crystalline and amorphous structures, corresponding to $m_{\text{amorphous}} = 83$ and $m_{\text{amorphous}} = 698$, with crystalline monomers marked in blue, and amorphous monomers marked in red. (b) shows the free energy landscape for the melting of single polymer crystals. The free energy is plotted as a function of the reaction coordinate $m_{\text{amorphous}}$, and is scaled relative to the thermal energy at each temperature that the parallel tempering Langevin dynamics is run for.

in red. The $m_{\text{amorphous}}$ can then be thought of as a reaction coordinate. We have computed a free energy landscape using Equation 3.4, by discretizing the reaction coordinate using a bin size of 50 for the number of amorphous monomers, and using a histogram method, like the one used by Welch and Muthukumar[49]. Our free energy estimates are shown in Figure 3.4.

In Figure 3.4b, we first discuss the crystalline region of the landscape. Our initial crystalline structures contain $m_{\text{amorphous}} = 83$, as shown in Figure 3.4a. Thus, the contribution to the landscape below the $m_{\text{amorphous}} = 100$ region comes from purely crystalline structures. Even though the free energy values for $m_{\text{amorphous}} = 50$ appear to have a very high value in comparison to that of the intermediate regions of the landscape, they correspond to highly crystalline configurations.

Next, we discuss the intermediate regions of the landscapes. The free energy landscapes reveal clear barriers in going from the crystalline to the molten state, as seen from the free energy values when going from $m_{\text{amorphous}} = 350$ to $m_{\text{amorphous}} = 400$.

Although on a relative energetic scale, these barriers seem to be nearly similar, we have also proceeded to compute the exact heights of these barriers F^*, and have given those in Table 3.1. These free energy barriers are of the order of 1.5 k_BT. The heights of these barriers are considerably less than the heights of the barriers shown by Hu and co-workers[129], whose predictions were of a barrier height of 25 k_BT. Such high barriers would mean that the system has a very low probability of transitioning between the two states. Such a large barrier could arise due to several reasons. Firstly, Hu *et al.* use a rigid rod-cylinder model to represent their polymer on a simple cubic lattice. This model only has bond-bond interaction energy without any consideration of trans-gauche conformations and polymer-polymer, polymer-solvent, and solvent-solvent interactions. Secondly, their estimate of the barrier height is at a temperature below T_m^0. In contrast, our simulation is an off-lattice simulation, accounting for conformational flexibility and Lennard-Jones interaction between the united atoms. This provides the polymer with far more freedom to explore its conformations and thereby transform from a packed crystal to a molten state. This could explain why we see barriers of considerably smaller heights than those of Hu *et al.* Even more significantly, our melting kinetics is followed at temperatures higher than the equilibrium melting temperature. In general, according to the classical nucleation theory, when a bulk crystal is superheated above its melting point, there is a nucleation barrier for the birth of droplets of the liquid phase. The stability of the nuclei is given by the melting spinodal, at which the nucleation barrier vanishes. For the single-chain crystal studied here, we are unable to record any such intra-chain nuclei of the liquid phase, as evident from Figure 3.1. The barrier in Figure 3.4b is distinct and not thermal noise, and thus it cannot be attributed to melting spinodal. It is also to be noted that the temperature range in Figure 3.4b is very wide (450 K in experimental units!), and the relative insensitivity of F^*/k_BT to temperature (Table 3.1) emphasizes that the barrier for melting is entropic in origin.

Table 3.1. Free energy barriers F^* at different melting temperatures corresponding to Figure 3.4

T^*	$\frac{F^*}{k_BT}$	F^* (kcal/mol)
12	1.77	2.38
14	1.51	2.37
16	1.08	1.95
18	1.36	2.74
20	1.55	3.47

3.3.3 Melting of multi-chain crystals

We now address the melting behavior of multi-chain crystals. The multi-chain crystal was grown by sequentially growing the crystal one chain after another, as is explained in detail in our previous work[132]. Upon completion of the growth procedure, the multi-chain crystal contained 21 polymer chains, each containing $N = 200$ monomers. The crystals were melted isothermally by allowing them to equilibrate at their melting temperatures T_m for several thousands of time units through the use of Langevin dynamics, similar to that for single crystal melting.

We choose seven different melting temperatures T_m - 11, 11.6, 12, 14, 16, 18, and 20 to judge the change in the conformation of the multi-chain crystal and the kinetics of disassembly with respect to increasing driving force for melting. As an example, we show the trajectories of two such melting temperatures $T^* = 12$ and $T^* = 18$ in Figure 3.5. The visualization has been rendered using the Visual Molecular Dynamics (VMD) package[67]. The 21^{st} chain has been marked in orange in Figure 3.5a, and in blue in Figure 3.5b to understand the effect that a rise in temperature has on the outermost chain in the aggregate.

Analogous to the melting of the single crystal, we observe differences in the melting of the multi-chain crystal with increasing temperature. At melting temperatures close to the equilibrium melting temperature T_m^0, like the one shown in Figure 3.5a, it was

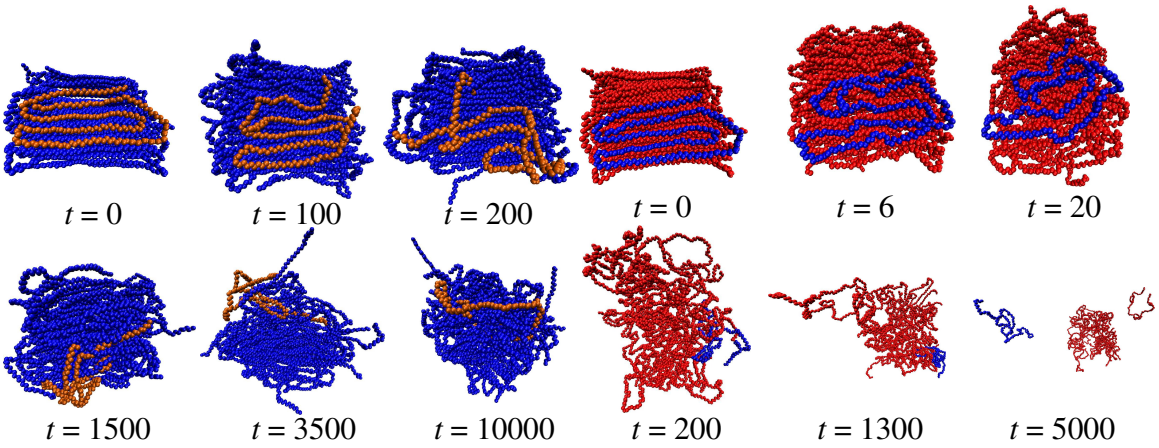

(a) $T^* = 12$ (b) $T^* = 18$

Figure 3.5. Representative snapshots for melting of a multi-chain crystal consisting of 21 chains of $N = 200$ from two out of the seven temperatures analyzed. The snapshots in (a) depict melting at a temperature of $T^* = 12$, and the snapshots in (b) depict melting at a temperature of $T^* = 18$. The 21^{st} chain has been marked for reference in orange in (a) and in blue in (b).

found that even after running the Langevin dynamics simulation for several thousands of time units, the multi-chain crystal does not separate into its individual chains but remains closely packed together in a dense disordered state. This is akin to the mesomorphic state that Hafele *et al.*[92] seem to observe in their re-crystallization experiments on random polyethylene-co-octene, and the inhomogeneous intermediate state that Muthukumar[77] invokes to explain the same phenomenon. Additionally, the entire crystal seemed to lose its order uniformly.

When the temperature was increased, it was found that the system escaped out of its dense compact shape into a free state, where the individual chains peel off from the core, and behave as independent chains. An example of this is shown in Figure 3.5b, where the chains begin to disengage from the crystal towards the end of the simulation. In essence, the melting process seems to comprise of a step where the crystal loses its order, and then expands in the next step. The accessibility of the

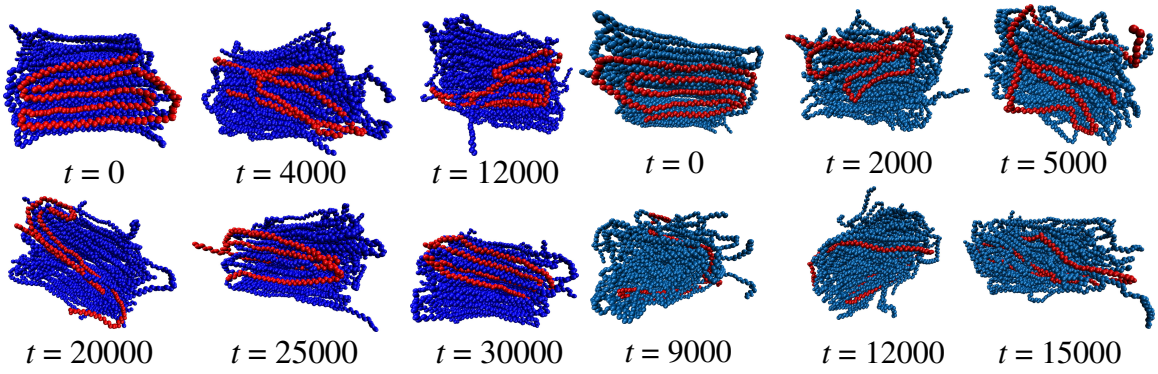

(a) $T^* = 11$ (b) $T^* = 11.6$

Figure 3.6. Representative snapshots for melting of a multi-chain crystal consisting of 21 chains of $N = 200$ from two out of the seven temperatures analyzed. The snapshots in (a) depict melting at a temperature of $T^* = 11$, and the snapshots in (b) depict melting at a temperature of $T^* = 11.6$. The 21^{st} chain has been marked for reference in red in both (a) and (b). At a temperature of $T^* = 11$, the aggregate continues to stay in its original state, while at $T^* = 11.6$ the aggregate melts to a partially disordered state.

latter step is dictated by the melting temperature, analogous to the melting of the single crystals.

We studied melting at temperatures even closer to the equilibrium melting temperature T_m^0 to further the longevity of the metastable state. As described previously, the multi-chain crystals were allowed to equilibrate at temperatures of $T^* = 11$ and $T^* = 11.6$. At a temperature of $T^* = 11$, we observed that the multi-chain crystal continues to remain in its crystalline state, while at the increased temperature of $T^* = 11.6$, we observed the aggregate to be in a partially ordered state. We show representative trajectories in Figure 3.6, and describe the evolution of disordering in the system next.

To explore the time scales involved in how the crystalline order of the polymer changes with temperature, we show the time evolution of the global order parameter averaged over all of the chains in Figure 3.7. We show the global average of the orientational order parameter at different melting temperatures. Figure 3.7a shows

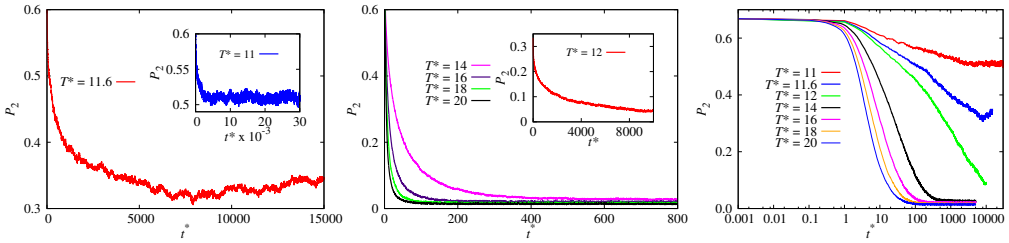

(a) T close to T_m^0 (b) $T > T_m^0$ (c) Semi-logarithmic scale

Figure 3.7. Time evolution of the global order parameter P_2 averaged over all of the chains at melting temperatures (a) close to T_m^0, (b) greater than T_m^0 and (c) at all the studied melting temperatures and displayed on a semi-logarithmic scale. The insets show the time evolution of the P_2 at the melting temperature of $T^* = 11$ (a) and $T^* = 12$ (b), and are displayed separately for clearly distinguishing the timescales involved from those of the other melting temperatures. All the data has also been displayed in a semi-logarithmic scale in (c) to distinguish the time-dependent relaxations for the cases in which the system stays in the metastable state ($T^* = 11.0, 11.6$, and 12.0).

the change in crystalline order for temperatures close to the equilibrium melting temperature, while Figure 3.7b shows the evolution of crystalline order for temperatures well above the equilibrium melting temperature. The insets in these figures represent the temperatures for which simulations were run for much longer times ($T^* = 11$ for Figure 3.7a and $T^* = 12$ for Figure 3.7b). They are shown separately to clearly distinguish the timescales involved. It can be seen from the figure that the crystalline order drops to negligible values very quickly for $T_m = 14, 16, 18,$ and 20, while the inset (Figure 3.7b) shows that a long time is required at $T^* = 12$ for the aggregate to become completely disordered. The rate at which the crystal loses order can be seen to increase with melting temperature. Moreover, Figure 3.7a shows the evolution of the crystalline order much closer to the equilibrium melting point. At the temperature of $T^* = 11$ as seen in the inset of Figure 3.7a, the system stays in a state of order that is very close to its original state of order. More interestingly, at a temperature of $T^* = 11.6$ as seen in Figure 3.7a, the system equilibrates to a state of partial order denoted by the value of P_2 at about 0.35. To quantify such metastable states, we then proceed to study the kinetics of melting of the multi-chain crystals.

The time evolutions of the orientational order parameter P_2, as given in Figure 3.7a and Figure 3.7b are presented in Figure 3.7c on a semilogarithmic plot. For high melting temperatures ($T^* > 14$), P_2 decays with time essentially as a single exponential. On the other hand, at temperatures of 11, 11.6, and 12, when the system stays in the metastable intermediate state, the kinetics is quite complex, representing a hierarchy of local back-and-forth segmental kinetics. For such temperatures, which are close to, but above the T_m^0, the time evolutions appear qualitatively as a stretched exponential (e^{-t^β}), with the exponent β roughly $\frac{1}{3}$.

3.3.4 Kinetics of melting of multi-chain crystals

To quantify the free energy of the melting of multi-chain crystals, we have performed parallel tempering Langevin dynamics simulations, similar to those for single crystal melting. The details of the parallel tempering simulations are shown in Table D.1 of Appendix D. Each melting temperature was explored by running a six-temperature tempering at $T = T_c,\ T_m - 0.4,\ T_m - 0.2,\ T_m,\ T_m + 0.2,\ T_m + 0.4$. The crystalline conformations were allowed into the simulation so as to ensure that swaps with crystalline regions were also possible. We computed the free energy landscape along the $m_{\text{amorphous}}$ reaction coordinate using Equation 3.4. The number of amorphous monomers were discretized using bins of size 100, and the bins were then transformed to free energy using a histogram method similar to the one used by Welch and Muthukumar[49]. The free energy estimates are shown in Figure3.8. The crystalline configurations at the beginning of the simulation have $m_{\text{amorphous}}$ in the range of 500-800. Therefore, the free energy well in the region around 500 in Figure 3.8 corresponds to the starting crystalline conformations. The points with $m_{\text{amorphous}} < 500$ correspond to the low probability that annealing of the crystal at T_c resulted in crystal thickening, causing the total number of amorphous monomers

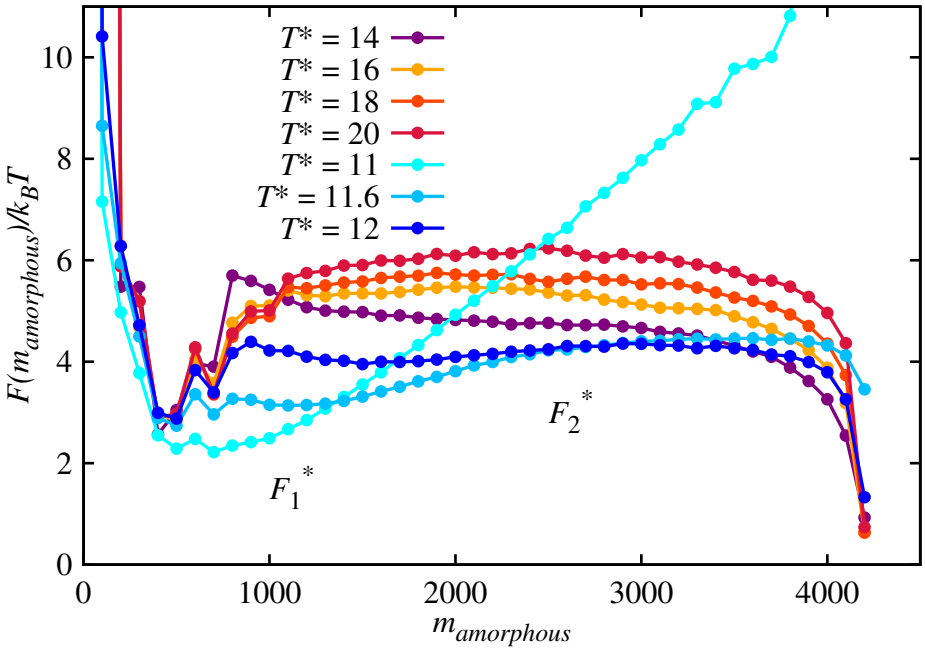

Figure 3.8. Free energy landscape calculated for the multi-chain crystal consisting of 21 chains of 200 monomers each. The free energy has been plotted relative to the thermal energy at each temperature. The free energy landscape reveals two barriers: one near the beginning of the landscape (the beginning of this barrier is denoted as F_1^*) and another near the middle of the landscape (F_2^*), which begins at about $m_{\text{amorphous}} = 1900$. The second barrier ($F_2^*$) is found only at the temperatures of $T^* = 11.6$ and $T^* = 12$, and vanishes as temperature is increased beyond that.

Table 3.2. Free energy barriers F_1^* and F_2^* at different melting temperatures corresponding to Figure 3.8.

T^*	$\frac{F_1^*}{k_BT}$	F_1^* (kcal/mol)	$\frac{F_2^*}{k_BT}$	F_2^* (kcal/mol)
11.6	0.62	0.81	1.73	2.25
12	1.52	2.04	0.4	0.54
14	3.13	4.91	-	-
16	2.57	4.61	-	-
18	2.57	5.17	-	-
20	2.73	6.12	-	-

to reduce. The low probability of this step is reflected in the very high free energy of the points below $m_{\text{amorphous}} = 500$.

The free energy landscapes shown in Figure 3.8 show the presence of two barriers, and they have been tabulated in Table 3.2. First, all the free energy landscapes show a free energy barrier at about $m_{\text{amorphous}} = 1000$ (F_1^*). The free energy landscape at $T^* = 11$ shows that the slightly molten crystals of Figure 3.6a and Figure 3.7a correspond to the valley in free energy at about $m_{\text{amorphous}} = 500$ in Figure 3.8. The system cannot escape the barrier at this temperature. As the temperature is increased we find that the system has to navigate through a barrier of finite height. The heights of these barriers, as tabulated in Table 3.2 show that these barriers are of nearly equal height, relative to k_BT.

Next, the free energy landscapes of Figure 3.8 also show a second barrier (F_2^*) near the middle of the landscape (around $m_{\text{amorphous}} = 2500$). The heights of these barriers have been tabulated in Table 3.2. From these values and from Figure 3.8, we can clearly see that the barrier height decreases with increasing melting temperature. At a temperature of $T^* = 11$, this barrier is too high for the system to surmount. When the temperature is increased to $T^* = 11.6$, the barrier reaches a finite size of $\sim 2k_BT$. When the temperature is increased further, the barrier height drops

even more, before disappearing at temperatures above $T^* = 14$. The positions of these barriers (near the middle of the reaction coordinate) prove the existence of the partially molten long-lived metastable states, which were shown earlier in Figure 3.6 and Figure 3.7a. The overall mechanism of the crossing of the two barriers at the temperatures of 11, 11.6, and 12 is quite rich and involves a hierarchy of local dynamics, as evident in Figure 3.7c. On the other hand, the melting mechanism at melting temperatures higher than 14 essentially follows an exponential kinetics, as seen in Figure 3.7c.

3.4 Conclusions

We have studied the melting of single molecule crystals and multi-chain crystals in solutions by the use of Langevin dynamics simulations. We have performed this using our coarse-grained united atom model, which was generated after making modifications to a model that represented polyethylene[61]. Using this system, we have observed the responses of the semicrystalline polymer systems to melting by allowing pre-formed crystals to equilibrate at temperatures above the equilibrium melting point, which was determined in our previous work[132]. To analyze the changes in the morphology of single crystals during melting, we have monitored the ensemble-averaged radius of gyration and the global order parameter. Additionally, we have developed a new order parameter by locally averaging the second order Legendre polynomial P_2 and determining if a particular monomer can be categorized as a crystalline or amorphous monomer. This idea has been adapted from some previous works[129, 131] and modified to suit our system. Using this new order parameter, we have computed free energy landscapes using parallel tempering Langevin dynamics simulations.

The melting of single molecule crystals is found to be qualitatively similar to the experimental results of melting of single polyethylene mats by Barham and Sadler[98],

when the crystals undergo a transition to a coil-like state. However, we find that the melting process is comprised of two steps: one where the crystal loses its order, and the other where the globule-like chain expands into a coil-like one. We find the former step to occur at every temperature studied, but the latter is accessible only when the temperature is increased relative to the equilibrium melting temperature. However, we did not find any evidence found to suggest preferential directions for melting, as seen in several experiments[107–110, 116, 117]. We suspect that this might be because of constant temperature provided to all monomers by the Gaussian random noise in our simulations. The kinetics of the melting process was quantified after sampling the free energy from parallel tempering Langevin dynamics simulation over 6 different temperatures (one of which was constrained to sample the crystalline configurations alone), and these revealed the presence of long-lived partially crystalline metastable states during the melting process. This has been observed in experiments as well[74, 92]. We quantified the free energy barrier, and found that there was one significant barrier in this process for single chain crystals. The position of the barrier, interestingly, was at the middle of the reaction coordinate and it had a height of approximately 2 k_BT.

For the melting of multi-chain crystals, we find that the crystal initially loses order uniformly, without any preferred direction. This is similar in feature to the melting of the single molecule crystal. The melting process is comprised of a step where there is a transition to a coil-like state formed before transforming to a free state where chains begin to peel off the crystal. The accessibility of the second step was dependent on the temperature, with higher temperature providing easier access. These simulations revealed that the system escapes its native state to a state of intermediate order at temperatures close to the equilibrium melting temperature, as addressed earlier by Muthukumar in a previous work[77], consistent with the hypothesis of mesomorphic state by Strobl[74, 92]. The extent of this intermediate ordering

decreases with increasing temperature. We quantified the free energy landscape using parallel tempering Langevin dynamics simulations. Simulations at all of the melting temperatures revealed a free energy barrier closer to the beginning of the reaction coordinate. At temperatures closer to the equilibrium melting temperature, the simulations revealed a second barrier near the middle of the landscape. These indicate that the partially molten metastable states are preferred by the system above the equilibrium melting temperature, with the preference for such states decreasing with increasing temperature consistent with the earlier theory by Muthukumar on melt memory[77]. At a certain temperature above the equilibrium temperature, the barrier near the middle of the reaction coordinate vanishes and the system prefers to be in a completely molten state.

CHAPTER 4

CRYSTALLIZATION OF TRIBLOCK COPOLYMERS

4.1 Motivation

Legacy polyolefin-based plastics are largely non-biodegradable, which makes them environmentally harmful. To make these plastics biodegradable, one of the techniques that has been recently suggested is the copolymerization of these homopolymers to triblock copolymers, which are blocky copolymers consisting of 3 different polymer sequences bonded together. Out of the multiple sequences of the triblock polymer, some would be these legacy olefins, while some others would be biodegradable blocks. The other polymer sequences being biodegradable makes the entire block copolymer biodegradable. This strategy has meant several investigations have explored the fundamental properties of such biodegradable polymers. Examples of such biodegradable blocks include Lactic acid, Lactide and Ethylene Glycol blocks. This has inspired several works to look into the properties of bulk triblock copolymers [136–138, 138–147]. However, a systematic investigation into the fundamental properties of crystallizable triblock copolymers is yet to be reported.

In his classical work, Flory [5, 54] predicted that the melting point of a polymer containing x_2 mole fraction of non-crystallizable blocky impurity will be depressed as given by the expression:

$$\frac{1}{T_m} - \frac{1}{T_m^0} = -\frac{R}{\Delta h} \ln p, \tag{4.1}$$

where p ($p < x_2$) is the sequence propagation probability, R is the universal gas constant, and Δh is the enthalpy of fusion. Although this sets the framework for developing an understanding of the properties of triblock copolymers, but the question

of the effect of crystallization kinetics on the melting point remains unanswered. Additionally, it also does not explain the effect of the position of the blocks on the kinetics of crystallization.

In an effort to explain the effects of kinetics on the crystallization of triblock copolymers, we have modeled several configurations of ABA triblock copolymers, BAB triblock copolymers, as well as B-AA multi-chain polymers. In our model, A is a crystallizable block, and B is a non-crystallizable block. In these configurations we have tailored the interaction between the A and B blocks to be either attractive or repulsive. We have also tailored the interaction of the non-crystallizable B block with the solvent to mimic a good solvent case, or a bad solvent case. This has given a rise to four combinations of polymer-solvent and polymer-polymer interactions for each of these three configurations of ABA, BAB and B-AA: attractive-good, attractive-bad, repulsive-good, and repulsive-bad. To compare with the base case, we have also crystallized a chain consisting purely of the crystallizable A block with the same molecular weight as that of the triblock copolymers. We explain our simulation model in Section 4.2, and melting point predictions in detail in Section 4.3 .

4.2 Simulation model

The details of the simulation method can be found in the previous chapter in section 2.2. We describe additional computational details below.

To crystallize all polymers, we equilibrate the chains to a temperature above the equilibrium melting temperature ($T^* = 15$), before introducing a step-change in temperature to $T^* = 9$.

We model the attractive interaction between the crystallizable and non-crystallizable blocks using the standard Lennard-Jones 12-6 potential as given by:

$$U_{LJ_{ABa}} = 4\epsilon_{ABa}\left[\left(\frac{\sigma_{ABa}}{r}\right)^{12} - \left(\frac{\sigma_{ABa}}{r}\right)^{6}\right], \tag{4.2}$$

where we choose the values of ϵ_{ABa} to be 4.0 and σ_{ABa} to be 1.0. This corresponds to a net excluded volume interaction of ~ -1.8, as seen in Figure 4.1a. We cut off this potential at a distance of 6.5 units, similar to the crystallizable $U_{LJ_{AA}}$ potential.

We model repulsive interaction between the crystallizable and non-crystallizable blocks using the Weeks-Chandler-Andersen potential as given by

$$U_{LJ_{ABr}} = 4\epsilon_{ABr}\left[\left(\frac{\sigma_{ABr}}{r}\right)^{12} - \left(\frac{\sigma_{ABr}}{r}\right)^{6} + 0.25\right], \tag{4.3}$$

where values of ϵ_{ABa} and σ_{ABa} are both taken to be 1.0. The cut-off distance for this potential is 1.12 units, which corresponds to the critical $2^{\frac{1}{6}}$ value. This corresponds to a net excluded volume interaction of ~ 1.8, as seen in Figure 4.1b.

To calculate the value of the excluded volume parameter v_{AB}, we simply integrate the appropriate potential U_{LJ}, according to the expression [62]

$$v = \int_0^{r_c} d\mathbf{r}_{ij}\left[1 - \exp\left(-\beta U_{LJ}\left(\mathbf{r}_{ij}\right)\right)\right]. \tag{4.4}$$

In our calculation, U_{LJ} and r_c are replaced with the appropriate potential and the appropriate cut-off distance in reduced units. We show the excluded volume interaction between A and B blocks v_{AB} in Figure 4.1. We show the excluded volume interaction between the monomers of the B block in Figure 4.2.

We model the repulsive interactions between the monomers of the B block by using a Lennard-Jones 12-6 potential, as given by

$$U_{LJ_B} = 4\epsilon_B\left[\left(\frac{\sigma_B}{r}\right)^{12} - \left(\frac{\sigma_B}{r}\right)^{6}\right], \tag{4.5}$$

where we choose the value of the ϵ_B to be either 4 or 1, depending on whether attractive or repulsive BB interactions are desired. The value of the σ_B is taken to be 1.0. The potential is cut-off at a distance of 6.5 in reduced units. To obtain the value

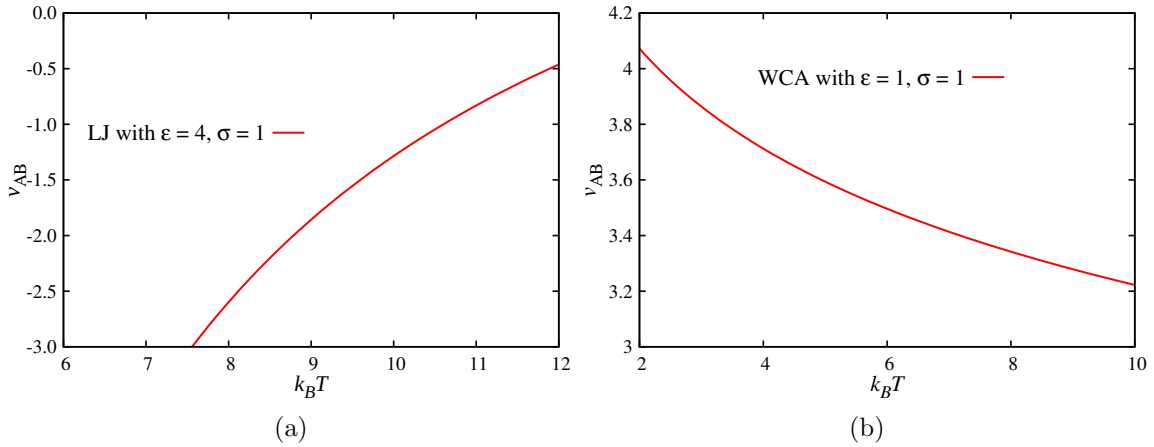

Figure 4.1. Excluded volume interaction between A and B blocks for the (a) attractive and (b) repulsive interactions. At our chosen crystallization temperature of $T^* = 9$, the effective attractive excluded volume parameter is ~ -1.8, while the analogous effective repulsive excluded volume parameter is ~ 1.8 at the same conditions.

of the excluded volume parameter v_B, we integrate equation 4.5 as per equation 4.4. We show the excluded volume parameters in Figure 4.2.

4.3 Results

We study the crystallization of several types of polymers: completely crystallizable, ABA triblock copolymers, BAB triblock copolymers, and B-AA multi chain polymers. To crystallize these polymers, a chain is started from a low-energy conformation and equilibrated at a temperature of $T^* = 15$, followed by a step-change to a temperature of $T^* = 9$. Then the chains were allowed to equilibrate at the temperature of $T^* = 9$ for several thousand time units in Langevin dynamics. In the following sections, we show typical simulation snapshots, along with determination of the melting point for some of the triblock copolymers. We study polymers at a constant degree of polymerization of $N = 600$.

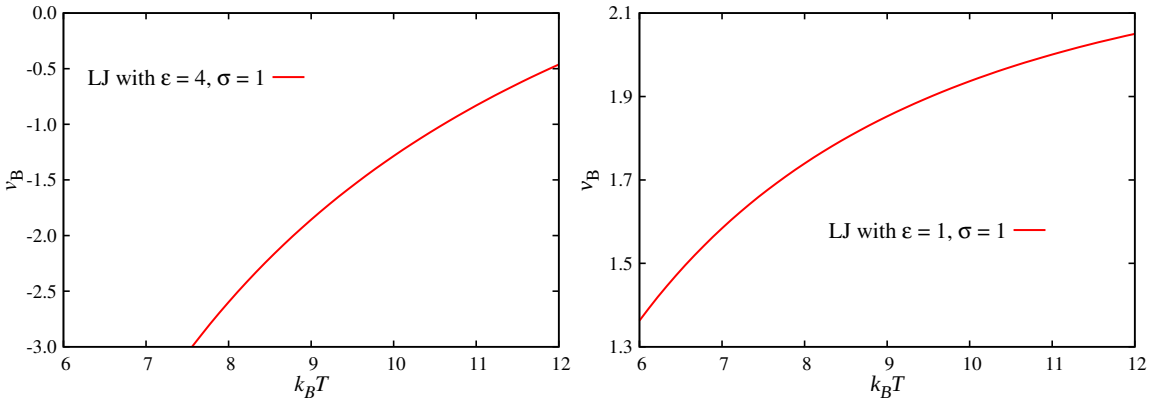

Figure 4.2. Excluded volume interaction between monomers in the B block for the (a) attractive and (b) repulsive interactions. At our chosen crystallization temperature of $T^* = 9$, the effective attractive excluded volume parameter is ~ -1.8, while the analogous effective repulsive excluded volume parameter is ~ 1.8 at the same conditions.

4.3.1 Pure crystallizable polymer

We crystallize a completely crystallizable polymer of containing 600 monomers for a clear comparison of crystallization properties between completely crystallizable and triblock copolymers containing different amount of non-crystallizable blocks. We show a typical simulation trajectory in Figure 4.3.

We see through the snapshots in Figure 4.3 that the crystallization process happens through the well-established mechanism of baby nuclei formation [7, 48, 49, 132], which are regions of segmental order within the chain. We showed this mechanism in chapter 2 of this thesis.

We also determine the equilibrium melting point of this polymer, by heating 15 pre-formed crystals to a temperature of $T^* = 13$ at 5 different heating rates of 0.0001, 0.0005, 0.001, 0.0015, and 0.002 $\frac{T^*}{t^*}$. Then we monitor the value of P_2, as shown in chapter 2, determine the first time step at which that value falls below 0.1. We consider the temperature at this time step to be the onset of melting. We determine the onsets of melting for all 15 crystals at a particular heating rate, and then calculate

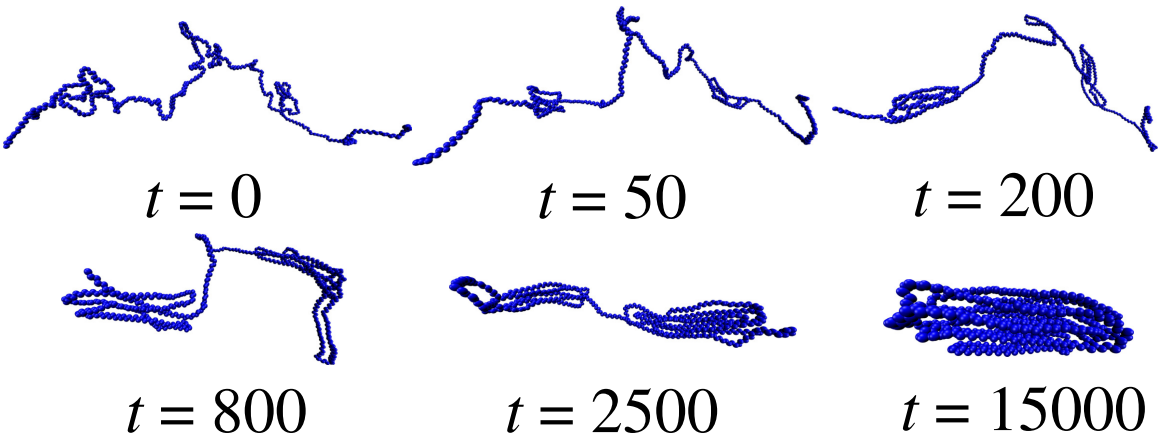

Figure 4.3. Typical simulation trajectory for the crystallization of a completely crystallizable polymer of $N = 600$. The polymer can be seen to crystallize through the mechanism of baby nuclei.

the average and the standard deviations. Then we plot the onsets of melting with the heating rates, and determine the equilibrium melting temperature from the y-intercept of that plot. We show our estimate of the melting point in Figure 4.4, which is obtained to be 10.68 ± 0.13.

4.3.2 ABA Triblock copolymers

We study the crystallization of ABA-type triblock copolymers where B is the non-crystallizable block. We study four types of ABA triblocks, depending on the interaction between A and B blocks, and the interaction between B and the solvent. In these simulations, we have 200 monomers in each block, making the entire chain consist of 600 monomers. We study crystallization in systems where the interaction between A and B blocks is attractive or repulsive, in combination with the B block being exposed to either a good solvent or a bad solvent, and we discuss these in the following subsections. In the simulation snapshots, the crystallizable A block is shown in blue, while the non-crystallizable B block is shown in red.

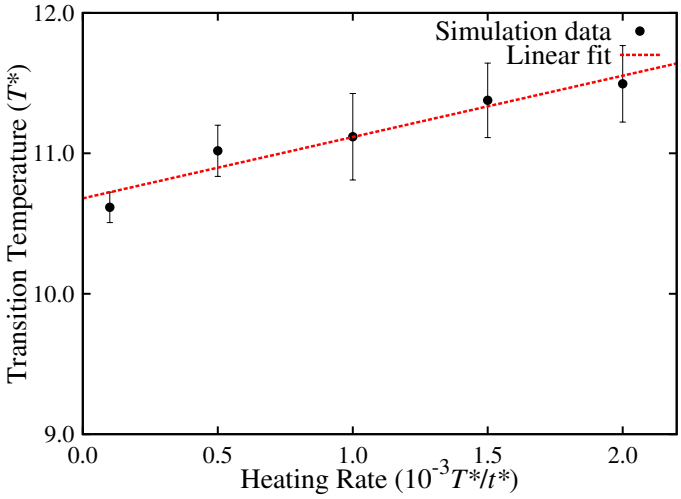

Figure 4.4. Determination of equilibrium melting point for completely crystallizable polymer containing 600 monomers. The equilibrium melting temperature is 10.68 ± 0.13.

4.3.2.1 B in good solvent and attractive A-B interactions

We first study an ABA system where A and B attract, while B is in a good solvent. This corresponds to cases where B can explore all its conformations. We expect the competing phenomena to be nucleation and subsequent crystallization of the A blocks, while being attracted to a self-avoiding B block. A typical trajectory is shown in Figure 4.5. The two A blocks crystallize by forming baby nuclei, while the B block explores its conformations as a self-avoiding chain at the crystallization temperature of $T^* = 9$. Since B attracts A, it pulls both A blocks together, which is reflected in the timescale of crystallization of the large A-A crystal.

We have computed the equilibrium melting temperature of this ABA triblock copolymer system using the same method that is described in Section 4.3.1. Our estimate for the equilibrium melting temperature is reported in Figure 4.6. We obtain the equilibrium melting temperature to be 10.26 ± 0.28. As expected from Flory's prediction (Equation 4.1), we see a depression in melting temperature from 10.68 to 10.26.

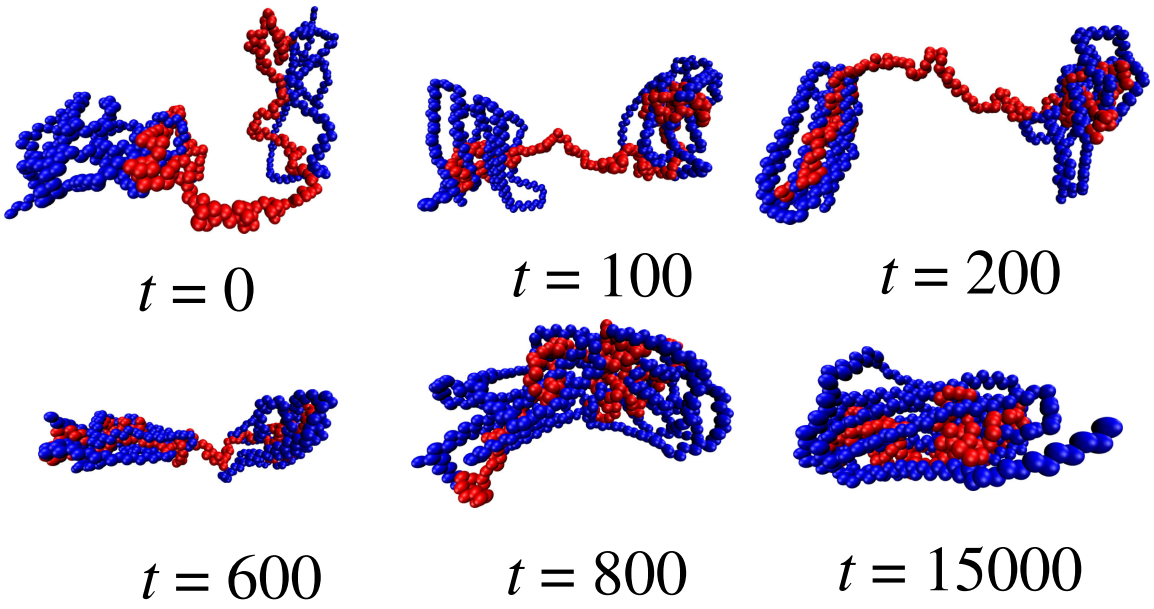

Figure 4.5. Typical simulation trajectory for the crystallization of an ABA triblock copolymer of $N = 600$, where B is in a good solvent, and A and B attract. Each A block crystallizes through the formation of baby nuclei. Finally, the triblock copolymer forms a micelle where the B block prefers to be in the interstices of the crystalline region formed by the two A blocks.

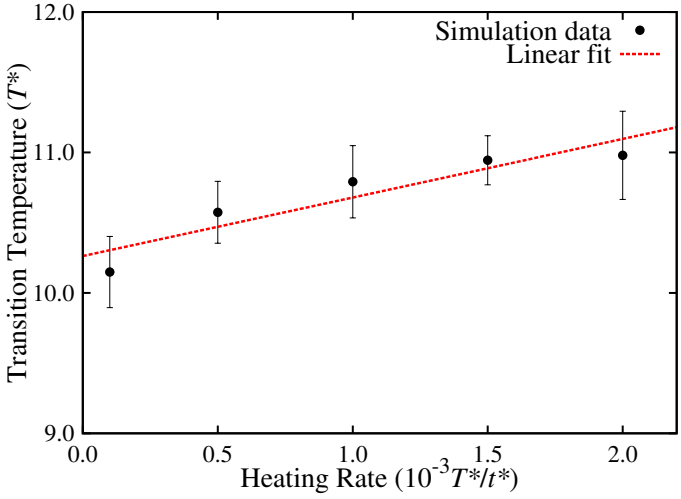

Figure 4.6. Determination of equilibrium melting point for ABA triblock copolymer containing 600 monomers, where A and B attract, while B is in a good solvent. The equilibrium melting temperature is 10.26 ± 0.28.

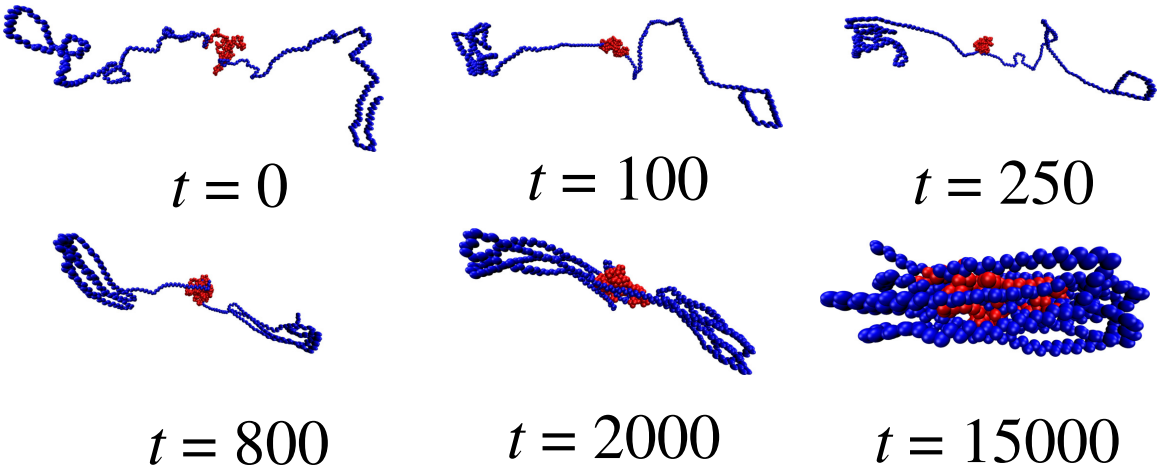

Figure 4.7. Typical simulation trajectory for the crystallization of an ABA triblock copolymer of $N = 600$, where B is in a bad solvent, and A and B attract. Each A block crystallizes through the formation of baby nuclei. Finally, the triblock copolymer forms a micelle where the B block prefers to be in a globular state in the interstices of the crystalline region formed by the two A blocks.

4.3.2.2 B in bad solvent and attractive A-B interactions

Next, we study an ABA system where A and B attract, while B is in a bad solvent. This corresponds to cases where B is in a collapsed conformation, and can only be globular. We expect the competing phenomena to be nucleation and subsequent crystallization of the A blocks, while being attracted to a globular B block. A typical trajectory is shown in Figure 4.7. The two A blocks crystallize by forming baby nuclei, while the B block collapses to a globule at the crystallization temperature of $T^* = 9$. Since B attracts A, it pulls both A blocks together, which is reflected in the timescale of crystallization of the large A-A crystal. However, the extent of this attraction is not very high as B is in a collapsed conformation.

We have computed the equilibrium melting temperature of this ABA triblock copolymer system using the same method that is described in Section 4.3.1. Our estimate for the equilibrium melting temperature is reported in Figure 4.8. We obtain the equilibrium melting temperature to be 10.16 ± 0.18. As expected from Flory's

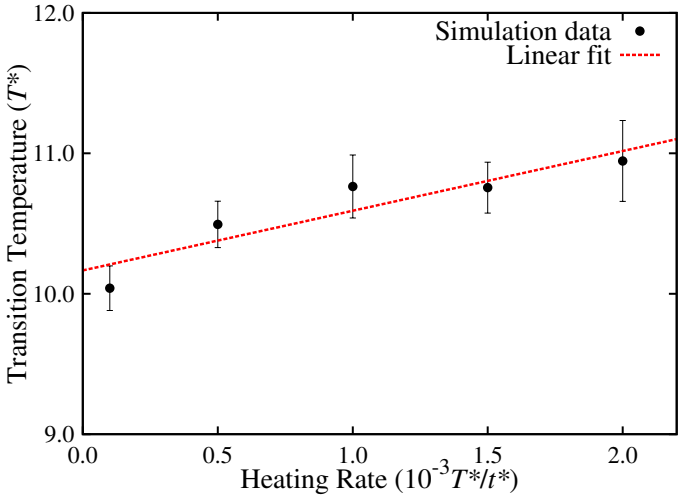

Figure 4.8. Determination of equilibrium melting point for ABA triblock copolymer containing 600 monomers, where A and B attract, while B is in a bad solvent. The equilibrium melting temperature is 10.18 ± 0.18.

prediction (Equation 4.1), we see a depression in melting temperature from 10.68 to 10.18.

4.3.2.3 B in bad solvent and repulsive A-B interactions

Next, we study an ABA system where A and B repel, while B is in a bad solvent. This corresponds to cases where B is in a collapsed conformation, and can only be globular. We expect the competing phenomena to be nucleation and subsequent crystallization of the A blocks, while being repelled by a globular B block. A typical trajectory is shown in Figure 4.9. The two A blocks crystallize by forming baby nuclei, while the B block collapses to a globule at the crystallization temperature of $T^* = 9$. Since B repels A, it pushes both A blocks apart, which is reflected in the huge increase in the timescale of crystallization of the large A-A crystal. However, the extent of this repulsion is not very high as B is in a collapsed conformation.

We have computed the equilibrium melting temperature of this ABA triblock copolymer system using the same method that is described in Section 4.3.1. Our estimate for the equilibrium melting temperature is seen in Figure 4.10. We obtain

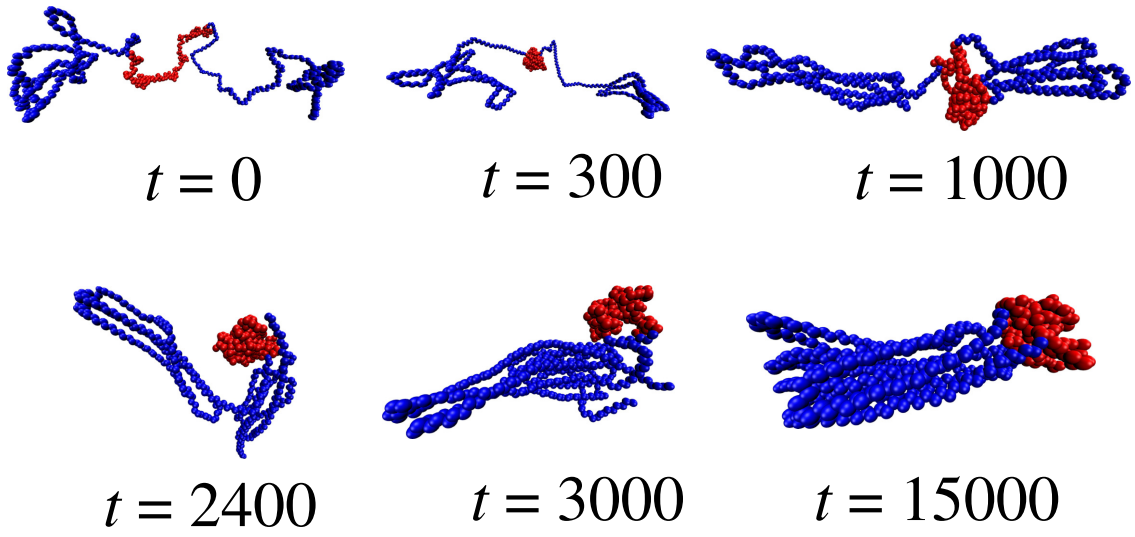

Figure 4.9. Typical simulation trajectory for the crystallization of an ABA triblock copolymer of $N = 600$, where B is in a bad solvent, and A and B repel. Each A block crystallizes through the formation of baby nuclei. Finally, the triblock copolymer forms a microphase-separated structure where the B block prefers to be in a globular state outside the crystalline region formed by the two A blocks.

the equilibrium melting temperature to be 9.42 ± 0.29. As expected from Flory's prediction (Equation 4.1), we see a depression in melting temperature from 10.68 to 9.42. The extent of the depression is much higher than that for the case where A and B blocks were attracting. This is because the attractive interactions promoted the formation of more stable crystals, while repulsive interactions mean the system needs more of a thermodynamic driving force to overcome the repulsions and form a crystal. This is reflected in the large deviation from the equilibrium melting temperature of the purely crystallizable polymer.

4.3.2.4 B in good solvent and A-B repulsive

Next, we study an ABA system where A and B repel, while B is in a good solvent. This corresponds to cases where B is can explore all its conformations, and is a self-avoiding chain. We expect the competing phenomena to be nucleation and subsequent crystallization of the A blocks, while being repelled by a self-avoiding B

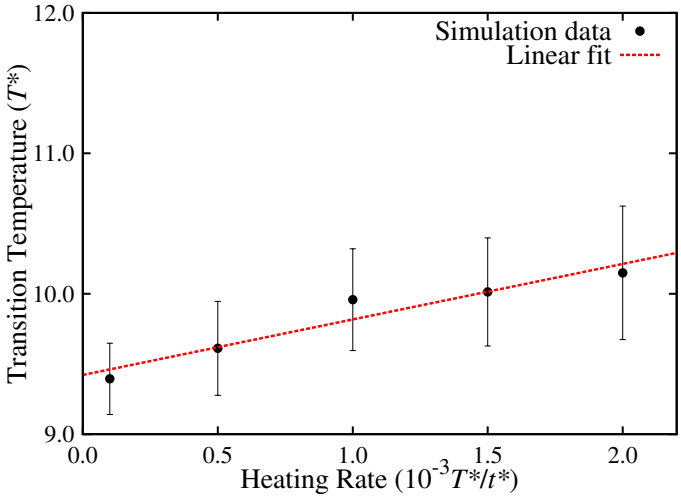

Figure 4.10. Determination of equilibrium melting point for ABA triblock copolymer containing 600 monomers, where A and B repel, while B is in a bad solvent. The equilibrium melting temperature is 9.42 ± 0.29.

block. A typical trajectory is shown in Figure 4.11. The two A blocks crystallize by forming baby nuclei, while the B block explores its conformations at the crystallization temperature of $T^* = 9$. Since B repels A, it pushes both A blocks apart. However, it itself is self-avoiding, and this makes it promote the crystallization of the two A blocks. This is reflected in the reduction in the timescale of crystallization of the large A-A crystal.

We have computed the equilibrium melting temperature of this ABA triblock copolymer system using the same method that is described in Section 4.3.1. Our estimate for the equilibrium melting temperature is seen in Figure 4.12. We obtain the equilibrium melting temperature to be 9.37 ± 0.26. As expected from Flory's prediction (Equation 4.1), we see a depression in melting temperature from 10.68 to 9.37. The extent of the depression is much higher than that for the case where A and B blocks were attracting. This is because the attractive interactions promoted the formation of more stable crystals, while repulsive interactions mean the system needs more of a thermodynamic driving force to overcome the repulsion and form a crystal.

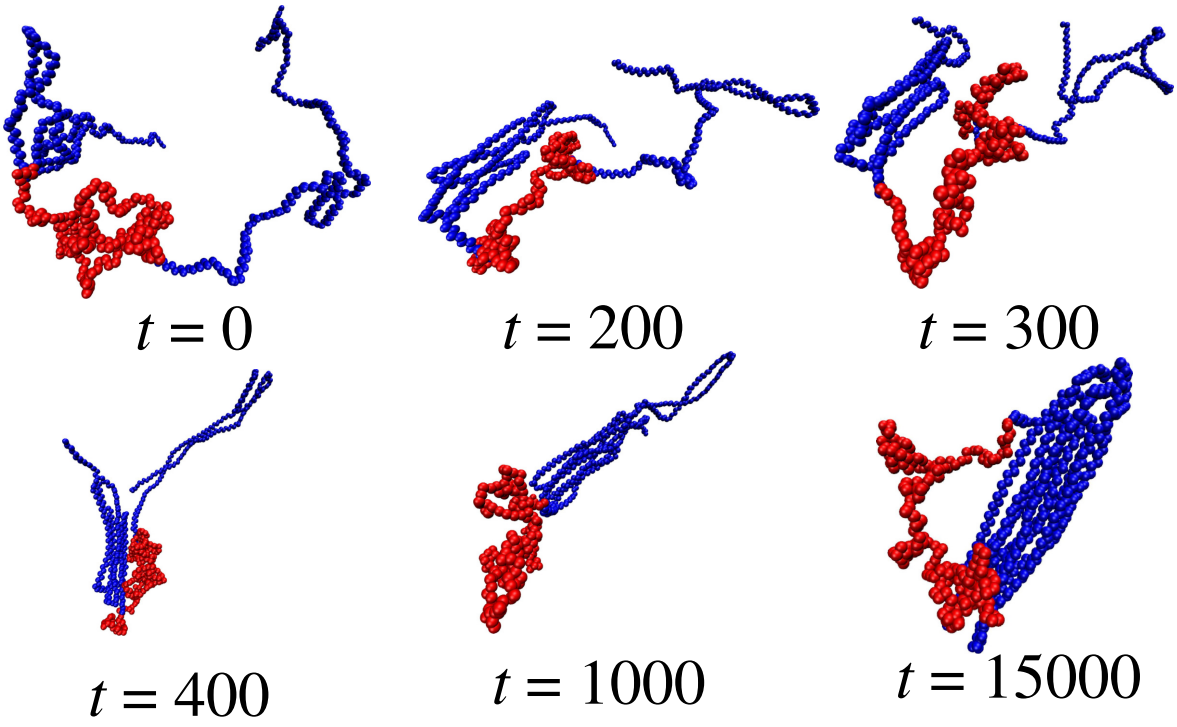

Figure 4.11. Typical simulation trajectory for the crystallization of an ABA triblock copolymer of $N = 600$, where B is in a good solvent, and A and B repel. Each A block crystallizes through the formation of baby nuclei. Finally, the triblock copolymer forms a microphase-separated structure where the B block prefers to be in a self-avoiding state outside the crystalline region formed by the two A blocks.

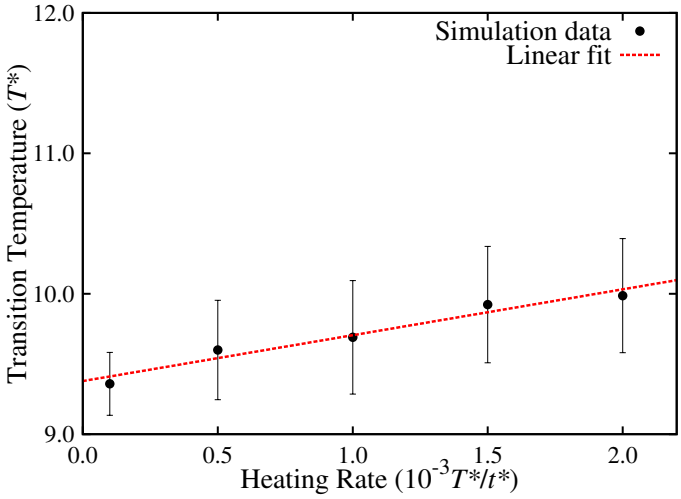

Figure 4.12. Determination of equilibrium melting point for ABA triblock copolymer containing 600 monomers, where A and B repel, while B is in a bad solvent. The equilibrium melting temperature is 9.37 ± 0.26.

This is reflected in the large deviation from the equilibrium melting temperature of the purely crystallizable polymer.

4.3.3 BAB triblock copolymers

We study the crystallization of BAB-type triblock copolymers where B is the non-crystallizable block. We study four types of BAB triblocks, categorized based on the interaction between A and B blocks, and the interaction between B and the solvent. In these simulations, we have 200 monomers in each block, making the entire chain consist of 600 monomers, just like the ABA-type triblock copolymers. We study crystallization in systems where the interaction between A and B blocks is attractive or repulsive, in combination with the B block being exposed to either a good solvent or a bad solvent, and we discuss these results in the following subsections. In the simulation snapshots, the crystallizable A block is shown in blue, while the non-crystallizable B block is shown in red.

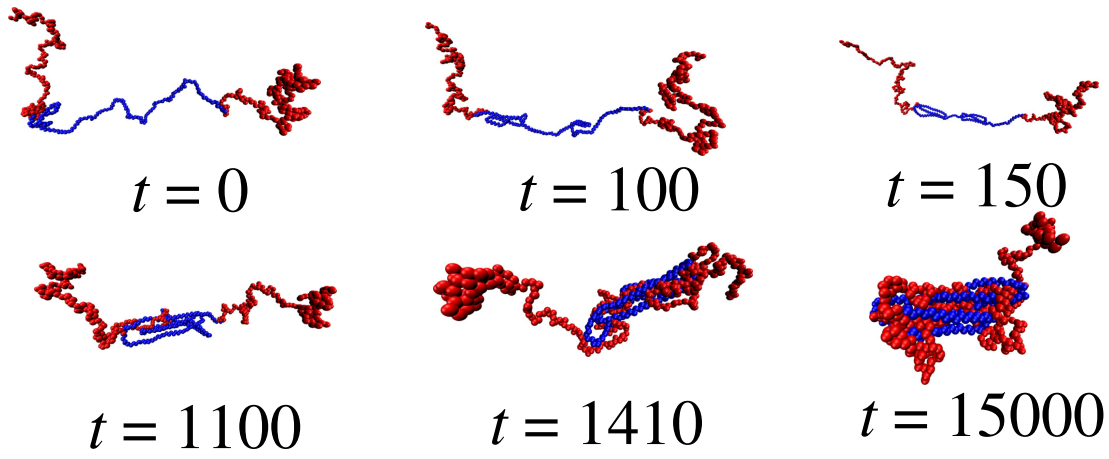

Figure 4.13. Typical simulation trajectory for the crystallization of a BAB triblock copolymer of $N = 600$, where B is in a good solvent, and A and B attract. The A block crystallizes through the formation of baby nuclei. Finally, the triblock copolymer forms a micelle, where the B blocks are both inside as well as outside the crystalline A block.

4.3.3.1 B in good solvent and attractive A-B interactions

We first study an ABA system where A and B attract, while B is in a good solvent. This corresponds to cases where B can explore all its conformations. We expect the competing phenomena to be nucleation and subsequent crystallization of the A blocks, while being attracted to two self-avoiding B blocks. A typical trajectory is shown in Figure 4.13. The A block crystallizes by forming baby nuclei, while the B blocks explore their conformations as self-avoiding chains at the crystallization temperature of $T^* = 9$. Both B blocks are attracted to A, but not to each other. Eventually they form micelles with the crystallized A block, and are present both inside as well as outside the crystal, owing to the reduced molecular weight of the crystalline component.

We have computed the equilibrium melting temperature of this BAB triblock copolymer system using the same method that is described in Section 4.3.1. Our estimate for the equilibrium melting temperature is shown in Figure 4.14. We obtain the equilibrium melting temperature to be 9.32 ± 0.21. As expected from Flory's

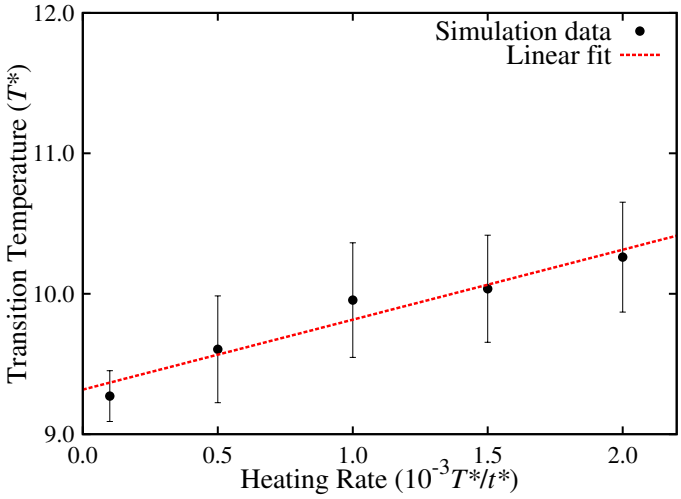

Figure 4.14. Determination of equilibrium melting point for a BAB triblock copolymer containing 600 monomers, where A and B attract, while B is in a good solvent. The equilibrium melting temperature is 9.32 ± 0.21.

prediction (Equation 4.1), we see a depression in melting temperature from 10.68 to 9.32. This depression in melting point is much larger than that of the corresponding ABA system because of an increased content of non-crystallizable impurity.

4.3.3.2 B in bad solvent and attractive A-B interactions

Next, we study a BAB system where A and B attract, while both B blocks are in a bad solvent. This corresponds to cases where B is in a collapsed conformation, and can only be globular. We expect the competing phenomena to be nucleation and subsequent crystallization of the A block, while being attracted to two globular B blocks which are also attracted to each other. A typical trajectory is shown in Figure 4.15. The A block crystallizes by forming baby nuclei, while the B blocks collapse to globules at the crystallization temperature of $T^* = 9$. Finally, the polymer forms a micellar structure with the B blocks going into the crystalline region formed by the A block, and severely distorting its crystallinity.

We have computed the equilibrium melting temperature of this BAB triblock copolymer system using the same method that is described in Section 4.3.1. Our

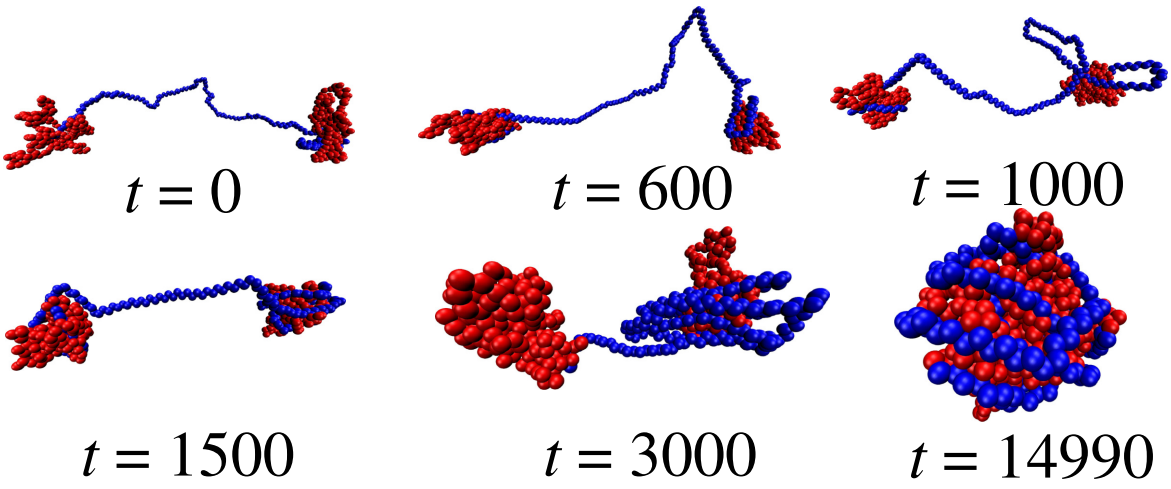

Figure 4.15. Typical simulation trajectory for the crystallization of a BAB triblock copolymer of $N = 600$, where the B blocks are in a bad solvent, and A and B attract. The A block crystallizes through the formation of baby nuclei. Finally, the triblock copolymer forms a micelle where the B blocks prefer to be in a globular state in the interstices of the crystalline region formed by the A block, severely distorting its crystallinity.

estimate for the equilibrium melting temperature is shown in Figure 4.16. We obtain the equilibrium melting temperature to be 9.01 ± 0.06. As expected from Flory's prediction (Equation 4.1), we see a depression in melting temperature from 10.68 to 9.01. However, the crystals were so distorted at the beginning of the melting procedure that the corresponding value of the P_2 order parameter was already below 0.1. So this melting point calculation has to be repeated by crystallizing the copolymer to a lower temperature of $T^* = 8$ perhaps.

4.3.3.3 B in bad solvent and repulsive A-B interactions

Next, we study a BAB system where A and B repel, while B is in a bad solvent. This corresponds to cases where B is in a collapsed conformation, and can only be globular. We expect the competing phenomena to be nucleation and subsequent crystallization of the A blocks, while being repelled by a globular B block. A typical trajectory is shown in Figure 4.17. The A block crystallizes by forming baby nuclei,

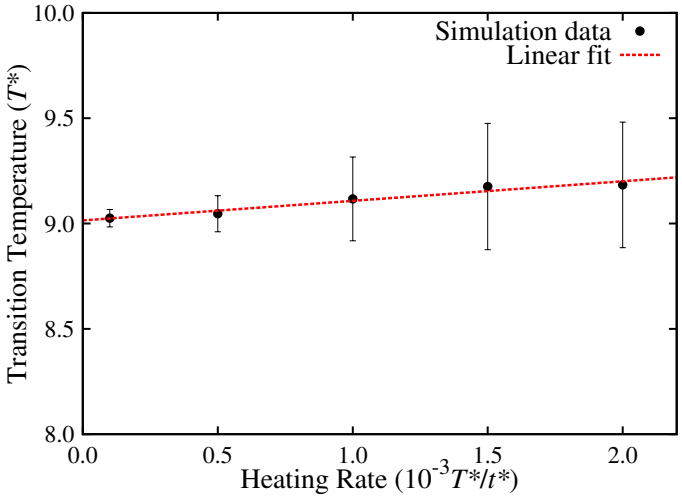

Figure 4.16. Determination of equilibrium melting point for BAB triblock copolymer containing 600 monomers, where A and B attract, while B is in a bad solvent. The equilibrium melting temperature is 9.01 ± 0.06, but the crystals were distorted below the onset of melting criterion at the beginning of the melting procedure. So this calculation will have to be repeated by crystallizing the copolymer to a lower temperature of $T^* = 8$ perhaps.

while the two B blocks collapse to globules at the crystallization temperature of $T^* = 9$. Finally, the B blocks combine together to form a globule and are separated from the crystalline A block.

We have computed the equilibrium melting temperature of this BAB triblock copolymer system using the same method that is described in Section 4.3.1. Our estimate for the equilibrium melting temperature is shown in Figure 4.18. We obtain the equilibrium melting temperature to be 9.26 ± 0.16. As expected from Flory's prediction (Equation 4.1), we see a depression in melting temperature from 10.68 to 9.26.

4.3.3.4 B in good solvent and A-B repulsive

Finally, we study a BAB system where A and B repel, while B is in a good solvent. This corresponds to cases where the B blocks can explore all their conformations, and are self-avoiding chains. We expect the competing phenomena to be nucleation and

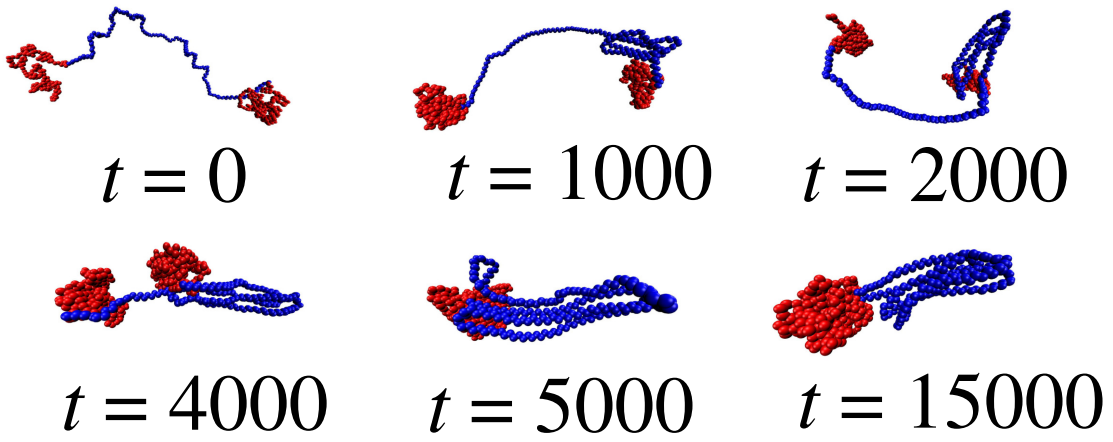

Figure 4.17. Typical simulation trajectory for the crystallization of a BAB triblock copolymer of $N = 600$, where B is in a bad solvent, and A and B repel. The A block crystallizes through the formation of baby nuclei. Finally, the triblock copolymer forms a microphase-separated structure where the B block prefers to be in a globular state outside the crystalline region formed by the two A blocks.

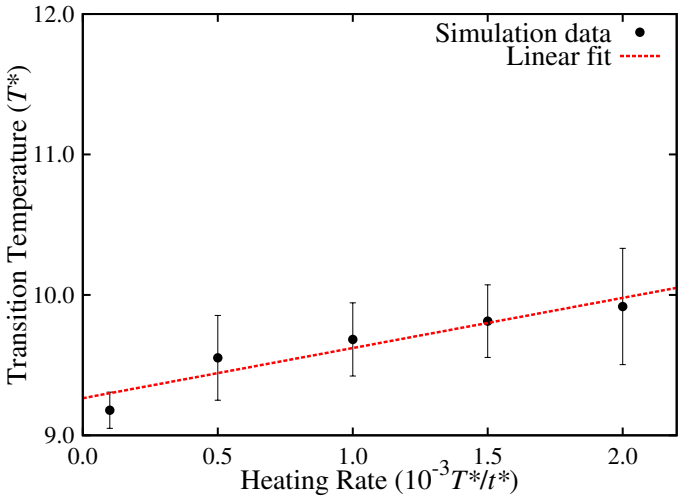

Figure 4.18. Determination of equilibrium melting point for BAB triblock copolymer containing 600 monomers, where A and B repel, while B is in a bad solvent. The equilibrium melting temperature is 9.26 ± 0.16.

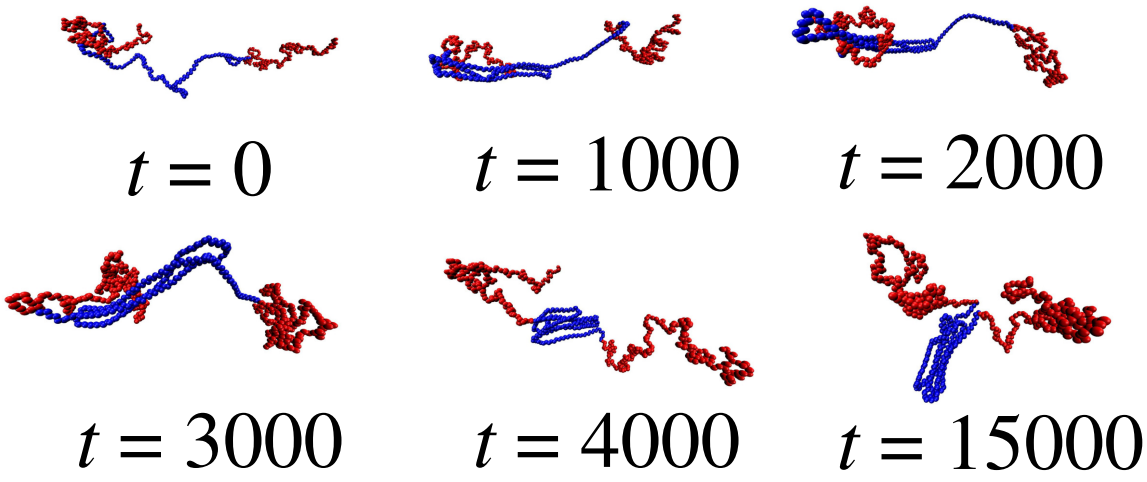

Figure 4.19. Typical simulation trajectory for the crystallization of a BAB triblock copolymer of $N = 600$, where B is in a good solvent, and A and B repel. Each A block crystallizes through the formation of baby nuclei. Finally, the triblock copolymer forms a microphase-separated structure where the B blocks prefer to be in self-avoiding state conformations the crystalline region formed by the A block.

subsequent crystallization of the A block, while being repelled by two self-avoiding B blocks, which repel each other as well. A typical trajectory is shown in Figure 4.19. The A block crystallizes by forming baby nuclei, while the B blocks explore their conformations at the crystallization temperature of $T^* = 9$. Finally, the copolymer forms a microphase-separated structure where all three blocks are separated from one another.

We have computed the equilibrium melting temperature of this BAB triblock copolymer system using the same method that is described in Section 4.3.1. Our estimate for the equilibrium melting temperature is seen in Figure 4.20. We obtain the equilibrium melting temperature to be 9.58 ± 0.38. As expected from Flory's prediction (Equation 4.1), we see a depression in melting temperature from 10.68 to 9.58.

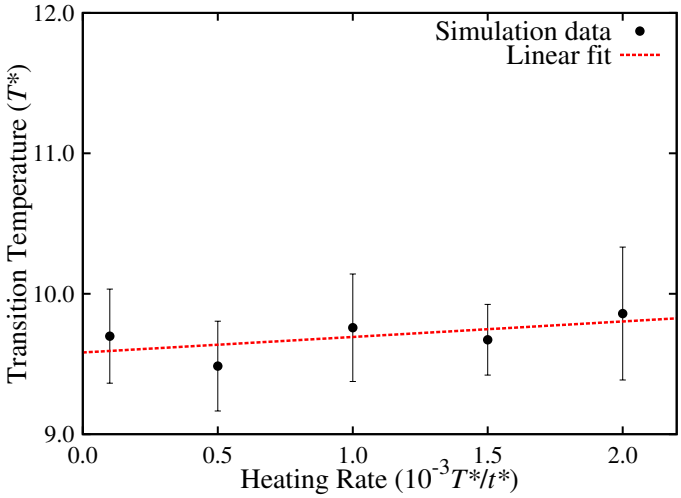

Figure 4.20. Determination of equilibrium melting point for the BAB triblock copolymer containing 600 monomers, where A and B repel, while B is in a bad solvent. The equilibrium melting temperature is 9.58 ± 0.38.

4.3.4 Crystallization of B and AA chains

When a B chain consisting of 200 monomers and an A chain consisting of 400 monomers was crystallized, the B chain simply diffused away from the A chain under all combinations of interactions. These simulations will have to be repeated with the B chain very close to the A chain.

4.4 Conclusion and Future Work

In this work, we have studied the effect of non-crystallizable blocky impurities (B) on the crystallization of a single chain, and have compared this to the crystallization of a completely crystallizable chain (A) of the same molecular weight. We have studied different levels of impurities by looking at the crystallization of ABA and BAB triblock copolymers. Then we computed their equilibrium melting temperatures using an approach similar to finding the first-passage time.

We find that the interactions between A and B blocks greatly affect the crystallization of the A block or blocks. Overall, the melting points of all systems agree

qualitatively with Flory's prediction of a depression in melting point when blocky impurities are present. However, the effect of the A-B interactions needs to be quantified properly as there are many effects which Flory's prediction cannot capture.

Firstly, the timescales of crystallization need to be determined for all systems. These timescales, once determined, will show whether the interactions with the non-crystallizable B block kinetically impair or promote crystallization. Secondly, the micellization process in the cases where micelles are formed can also be studied better. The micellization can be followed by a reverse micellization step, where the B block is changed from a bad solvent case to a good solvent case. The kinetics of this process can be determined using these simulations, and that will be technologically relevant. Next, the structure factor can be determined for the early stage of crystallization. This will determine how the length scales of the baby nuclei are affected by the presence of the B blocks. Subsequently, the final equilibrium configuration has to be quantified based on the A-B and B-solvent interactions. Next, crystallization of patterned polymers (to perhaps model trimers like those of Mucin [148] or other biological polymers like DNA) can be studied by tailoring these blocky models accordingly. Finally, the monomeric mean-squared displacement can also be tracked to find whether the crystallizing monomers are diffusing or not. Overall, these ABA and BAB triblock copolymer systems provide a very promising set of systems, which can lead to the discovery of a lot of inherent physical phenomena.

CHAPTER 5

CRYSTALLIZATION OF CALCIUM OXALATE

5.1 Motivation

Nephrolithiasis, commonly known as the disease of kidney stones affects large portions of the population by forming hard deposits in the kidney. These stones are then difficult to pass out of the body through urination, leading to extreme pain. The stones then need to be removed out of the kidney through procedures which break them into smaller parts, which can then be passed out by regular urination. Kidney stones, which affect roughly 10% of the population [149], are formed when the concentration of oxalate ions in the body exceeds a particular limit.

Chemically, kidney stones are crystals, which consist of calcium oxalate monohydrate and calcium oxalate dihydrate, which are formed by the process of nucleation and growth, in the presence of some critical biological macromolecules [150]. There have also been investigations in which it was observed that calcium oxalate nuclei adhere and stick to the walls of the kidney and then grow [151–153]. All current research investigating mitigation of kidney stone formation attempt at preventing either nucleation or the growth of pre-formed nuclei. Some of these methods involve inhibiting the crystallization of calcium oxalate using small molecule and polyelectrolyte additives [154–157].

Since kidney stones are chemically calcium oxalate crystals, many experimental investigations have attempted to study the effect of inhibition of calcium oxalate formation in solutions which mimic the conditions of the human body (typically in solutions containing 150 mM NaCl). Several experimental investigations show that

only anionic polyelectrolytes inhibit the growth of calcium oxalate crystals [158–173]. On the other hand, neutral or cationic polyelectrolytes have not shown an effect on crystallization, indicating a peculiarity in the interaction between salt ions and polyanions.

In this work, we attempt to elucidate this peculiarity of interaction by first crystallizing pure calcium oxalate. To complete this work, the effect of a polyelectrolyte additive on this crystallization process will have to be studied. We show our experimental methods in Section 5.2, our microscopy result in Section 5.3 and conclude with some future ideas.

5.2 Experimental methods

5.2.1 Materials

We purchased the following reagents from Sigma Aldrich for Calcium oxalate monohydrate crystallization: Sodium oxalate (ACS reagent, $\geq$ 99.5%), anhydrous Calcium chloride (ACS reagent, $\geq$ 96%). We purchased Sodium chloride from Fisher Chemical. We also used Milli-Q water, as obtained from the Milli-Q dispenser to make solutions.

5.2.2 Crystallization methods

The crystallization method was adapted from the work of Chung and co-workers [6]. We prepared stock solutions of calcium chloride (10mM), sodium oxalate (10mM) and sodium chloride (1M). Using these stock solutions, we prepared a 10mL solution of composition 0.7mM $CaCl_2$, 0.7mM $Na_2C_2O_4$ and 150mM NaCl at 60°C in a clean glass vial. We did this by making two separate solutions. The first solution contained NaCl and water, into which $CaCl_2$ was added under constant stirring using a magnetic stirrer on a hot plate at 60°C. Then the vial containing this solution was placed in an oven at 60°C for a period of 1 hour. After 1 hour, the vial was removed from the

oven and $Na_2C_2O_4$ was added in a dropwise manner over a period of precisely 30 seconds under stirring at constant moderate RPM. Once all the $Na_2C_2O_4$ was added, the magnetic stirrer was carefully removed from the solution using a magnet. Once removed, a piece of a cut glass slide was slowly dropped into the glass vial. Then the vial was placed in the oven for a period of 3 days at a temperature of 60°C without disturbing it.

After a period of 3 days, we observed solids deposited on the glass slide. The glass slide was slowly removed from the solution and dried under air overnight. Then the glass slide was imaged using a Leica DM 2700 P optical microscope.

5.3 Results

We prepared calcium oxalate monohydrate crystals and imaged them using a Leica Optical microscope at a zoom of 20X. Our microscope images confirm the presence of single crystals. We show our optical microscope images in Figure 5.1. We show two representative single crystals in Figure 5.1a and Figure 5.1b. The hexagonal morphology of the crystal matches the morphology obtained by Chung and co-authors [6].

5.4 Conclusion and Future Work

We prepared calcium oxalate crystals using a method described by Chung and co-workers [6]. After these crystals were prepared, we imaged these crystals using an optical microscope and obtained hexagon-shaped crystals just like those obtained by Chung *et al.*

The study of preventing the formation of kidney stones centers around small-molecular and macromolecular additives, which distort the crystallization of calcium oxalate monohydrate. At present, it is known that anionic polyelectrolyte additives prevent this crystallization, with cationic ones not affecting it in any manner. This

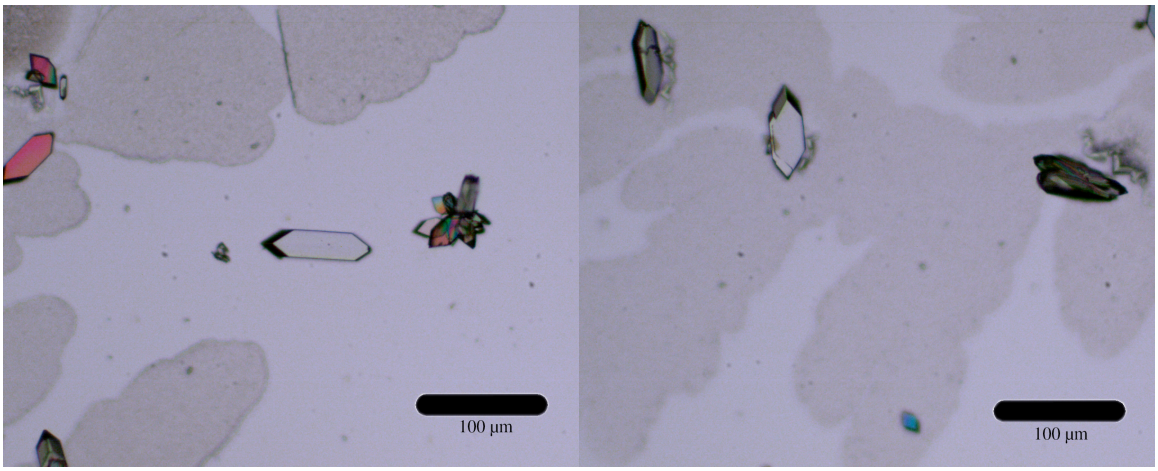

(a) Image of crystal 1 (b) Image of crystal 2

Figure 5.1. Representative optical microscope images for the single crystals obtained after the crystallization procedure. The scale bar corresponds to a length of 100 μm.

necessitates probing the nature of the interaction between calcium oxalate and polyelectrolytes. This can be done by studying the effect of zwitterionic polyelectrolytes on the crystallization of calcium oxalate, which is an open question in the field of small-molecular crystallization.

CHAPTER 6

CRYSTALLIZATION OF BRANCHED POLYMERS

6.1 Motivation

Classical experimental investigations of the crystallization of olefins were predominantly those of branched polymers, because of a lack of purity of linear polymers, which were obtained from catalytic polymerization reactions [174]. Typically, these branches act as impurities to the crystallization of polymers, with the final morphology of the branched polymer dependent on the length of the polymer.

Fundamentally, the effect of branching on the crystallization of linear polymers is best captured by Flory's prediction. He predicted that the melting point of an otherwise linear polymer gets depressed according to the expression:

$$\frac{1}{T_m} - \frac{1}{T_m^0} = \frac{R}{\Delta h}\frac{v_u}{v_1}\frac{N_{\text{imp}}}{N}, \tag{6.1}$$

where Δh is the enthalpy of crystallization of the linear chain, v_u is the molar volume of the crystallizable unit, v_1 is the molar volume of the non-crystallizable component, N_{imp} is the degree of polymerization of the non-crystallizable impurtity and N is the degree of polymerization of the entire polymer. In their work, Ungar and Zeng [71] have detailed the effect of branching on n-alkanes and have catalogued that branches get expelled from the crystalline region into the interlamellar amorphous region, causing the polymer to fold at the branch points. Keith and Padden then showed that these impurities slow down the kinetics of crystallization to a parabolic form, where the radius of the spherulite varies as $\sqrt{t}$ [175, 176]. This slowing down of crystallization has also been observed in molecular dynamics simulations [177]. Recently, Rojas

et al. [178] studied the crystallization of precisely branched polyethylenes (branches on every 21^{st} carbon atom) and showed that branches upto butyl branches are accommodated within the crystalline region, while larger branches get expelled into the amorphous region. They also found that when branches were expelled into the amorphous region, the melting points of the polymers were not affected, in apparent contradiction of Flory's predictions [5]. Moreover, branched polyethylene-like copolymers have been known to cause memory effects in the recrystallization of a melt [74, 78–82, 84, 85, 179–181]. Thus, branched polymers have always been of interest to polymer scientists. However, the primary nucleation mechanism of branched polymers is something that has not been investigated.

Muthukumar and Welch showed that the mechanism of nucleation for linear polymers was one in which the polymer forms intramolecular regions of segmental order (called "baby nuclei"), which then reel in all the other monomers sequentially to form one single crystal [7]. Ono and Kumaki [182] then proved the experimental existence of this mechanism by showing AFM images which matched exactly with the earlier simulation predictions.

In an effort to extend the simulations of Muthukumar and Welch [7] for branched polymers, we have modeled polymers containing octene branches, making each branch consist of 6 monomers. We vary the frequency of branching, but keep the total branch content to match the experimental branch content of Alamo [79] and Strobl [179] at roughly 5 mol%. We detail the simulation model in Section 6.2, the results in Section 6.3, and we conclude in Section 6.4.

6.2 Simulation model

Our simulation model for the regular linear polymer and the monomers of the branches has been described in reference [132], as well as in Chapter 2 of this dis-

sertation. We describe below the additional modeling details required to model the monomers at the branch points.

To model the monomers at the branch points, we introduce a degree of flexibility by relaxing the forces arising from the bond angle and the dihedral angle. The monomer at the branch point is subjected only to the bonding potential, and the modified Lennard Jones potential. The potential energy associated with the chemical bonds is taken to be the harmonic form:

$$U_r = k\left(r - r_0\right)^2, \tag{6.2}$$

where r is the bond length and r_0 is the equilibrium bond length. In this potential, k is taken to be 115 kcal/mol Å^2 and the r_0 is taken to be 1.54 Å. The potential energy associated with non-bonded interactions is taken to be the modified Lennard-Jones potential:

$$U_{LJ} = \epsilon\left[\left(\frac{\sigma}{r}\right)^{12} - 2\left(\frac{\sigma}{r}\right)^{6}\right], \tag{6.3}$$

where the interaction strength ϵ is set to 0.112 kcal/mol. The equilibrium distance σ is 4.53 Å for beads further than five repeat units apart along the chain backbone, and along the branch. Beads closer than five repeat units along the chain backbone, along the branch, and those closer than five repeat units around the branch points interact with a reduced value of σ equal to 1.54 Å. The monomer at the branch is not subjected to the bond angle and dihedral potential. We then follow a similar crystallization procedure to the one showed in Chapter 2.

6.3 Results

We study the crystallization of several types of branched polymers, in which we maintain the degree of branching at approximately 5 mol% (36 monomers in 6 branches) and vary the location of branches along the 700-monomer linear poly-

mer. The 6 branches are either at one end of the linear polymer and separated by 21 monomers, or spread out across the linear polymer and separated by 100 monomers. We also study the crystallization of one type of precision polymer, where we add branches to our polymer at every 21^{st} monomer of the polymer backbone of 700 monomers to match those created experimentally by Wagener and co-workers [178] (192 monomers in 32 branches). We consider the nature of the impurities to be octene impurities to match the experiments of Strobl and co-workers [92], which then makes the impurities a 6-monomer sequence. To crystallize these polymers, we equilibrate a low-energy conformation of every chain at a temperature of $T^* = 15$, and then equilibrate to a temperature below the melting temperature of the linear polymer. We choose this temperature to be $T^* = 8$ for the cases where 6 branches are added to the linear chain, and $T^* = 7$ for the case where 32 branches are added to the polymer.

6.3.1 6 branches on the linear backbone

We crystallize branched polymers containing 6 branches either at an end of the polymer or spread out across the polymer, and show typical simulation trajectories in Figure 6.1. We see from the figure that both kinds of polymers crystallize even though non-crystallizable branches are present. This is in qualitative agreement with the experiments of Alamo [79] and Strobl [179].

We show typical simulation snapshots of a branched polymer with branches at one end of the polymer in Figure 6.1a. We see from these simulations that the presence of branches has a destructive effect on the formation of "baby nuclei" [7]. The polymer chain can be seen to form nuclei in the region where the branches exist, but the nuclei are not crystalline. On the other hand, at the end where the branches are not present, the baby nucleus is very similar to that seen in Chapter 2. Additionally, the branches are also expelled from the final crystal as can be seen in the simulation snapshots.

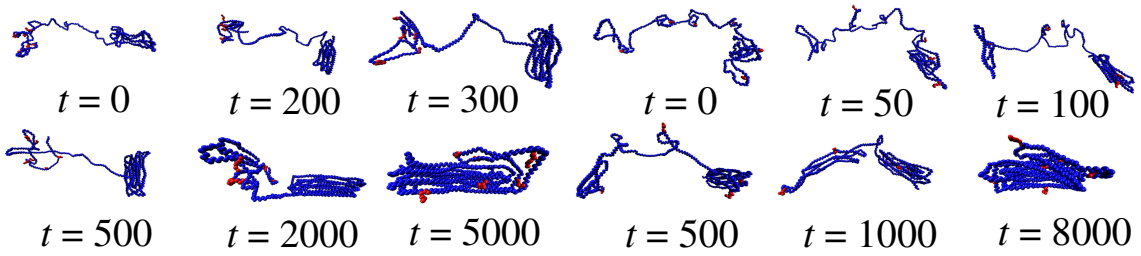

(a) Branches at end of polymer (b) Branches spread out along the polymer

Figure 6.1. Representative snapshots for crystallization of a branched polymer containing 6 branches. The snapshots from (a) depict crystallization when branches are separated by 21 monomers at one end of the linear polymer, while the snapshots from (b) depict crystallization when the branches are separated by 100 monomers across the entire length of the linear polymer. Monomers in the branches have been shown in red for clarity.

We show typical snapshots of a polymer with the branches separated by 100 monomers in Figure 6.1b. We see from these snapshots that the integrity of the baby nuclei is maintained despite the presence of non-crystallizable branches. The polymer then crystallizes in a manner similar to that of the linear polymers shown in Chapter 2, and expels the branches to the outside of the crystal.

6.3.2 32 branches on the linear backbone

We have also crystallized a linear polymer, which has 32 branches on its backbone. These branches are separated by 21 monomers, in a bid to match the system with the precision polyethylenes of Wagener [178]. We show typical simulation snapshots for this crystallization in Figure 6.2.

We see from these simulation snapshots that the polymer tries to crystallize by forming baby nuclei, the branches disrupt the crystallinity of these baby nuclei. The polymer then forms amorphous aggregates across the chain, which then coalesce to form a large amorphous globule. The branches can be seen to be inside as well as outside the globule.

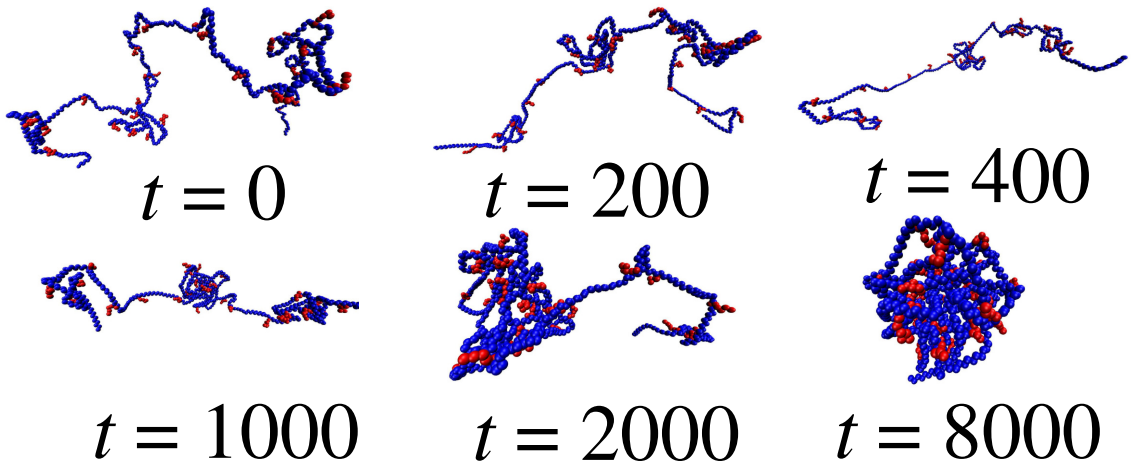

Figure 6.2. Representative snapshots for crystallization of a linear polymer of 700 monomers containing an additional 32 branches with 6 monomers in each branch. These branches are separated by 21 monomers, and are shown in red in the snapshots for clarity.

6.4 Conclusion and future work

In this work, we have studied the effect of non-crystallizable branched impurities on the crystallization of a single linear chain. We have studied two cases where the branching content is about 5 mol%, and another cases where the branching content rises to about 20 mol%. For the lower branching content case, we have looked at two systems: one where the branches are separated by 21 monomers and are restricted to one end of the polymer, and the other where the branches are spread out across the entire length of the polymer and are separated by 100 monomers. We find that these systems are crystallizable despite the presence of non-crystallizable impurities, and this is in qualitative agreements with the experimental systems that they have been designed to mimic [78, 179]. The branches disrupt the crystallinity of the baby nuclei when in close proximity with one another. For the 20 mol% branching case, the crystallinity of all the baby nuclei were disrupted and the entire polymer formed an amorphous globular aggregate.

Several quantities need to be computed to take this work to completion. Firstly, the timescales of crystallization will reveal the quantitative effect of the disruptive motion of the branches. Next, the structure factor should be determined for the early stage mechanism to quantify the extent to which the branches disrupt the crystallinity of the baby nuclei. Next, mean-squared displacements of branched as well as backbone monomers should be computed for long times to determine the nature of the motion within the crystalline polymer. Next, a distribution of lamellar thicknesses should be determined, followed by an estimate of the melting temperatures of these branched polymers. Finally, the effect of these branches on the melting of the polymer should be studied, as this will add to the experimental knowledge of melt-memory for these systems.

CHAPTER 7

CONCLUSIONS AND FUTURE WORK

7.1 Conclusions

In this thesis, we have investigated the effects of kinetic factors on the crystallization of various semicrystalline polymer systems: ring polymers, triblock copolymers, and branched polymers using Langevin dynamics simulations. We have also studied the reverse process of crystallization - melting for linear polymers. Additionally, we have also investigated the crystallization of calcium oxalate, which is a primary constituent of kidney stones using crystallization experiments and optical microscopy.

In the first work, we have compared the crystallization of ring polymers with that of linear polymers by crystallizing single linear and single ring polymers. Our results show that equilibrium melting points of single ring polymers are about 68°C lower than their linear analogues, which is in qualitative agreement with several experimental findings and in disagreement with several others. To explain this feature, which cannot be accounted for by equilibrium thermodynamic arguments, we investigated several kinetic factors. We find through an analysis of the scattering structure factor that ring polymers crystallize faster than linear polymers at the same temperature, and nucleate even faster when crystallized at the same degree of undercooling. We also find several metastable lamellar thicknesses into which the ring polymers crystallize, with large free energy barriers separating the lamellar thicknesses, whereas the linear polymer crystallizes into a single lamellar thickness. Moreover, we find that ring polymers have to negotiate several free energy barriers in their secondary nucleation, while linear polymers add onto existing crystals spontaneously. Due to these

reasons, we conclude that ring polymers melt at lower temperatures than ring polymers, even though equilibrium thermodynamic arguments suggest that the opposite behavior should be expected.

In the second work, we studied the melting of two types of linear polymer crystals - single crystals and multi-chain crystals, using Langevin dynamics simulations by heating the systems at temperatures above the equilibrium melting points. We find the existence of globular metastable states at lower equlibrium melting temperatures. The single polymers melt to globular conformations at lower temperatures before transforming to self-avoiding chains at higher melting temperatures. Similarly, the multi-chain crystals melt to a globular aggregate at lower temperatures and then peel off from the globular core at higher melting temperatures. We have computed a free landscape across this crystalline-amorphous reaction coordinate using parallel tempering Langevin dynamics simulations and have found one free energy barrier in the melting of single crystals, and two barriers in the melting of multi-chain aggregates.

In the third work, we have studied the effect of non-crystallizable blocky impurities and their interaction with the crystallizable blocks on the crystallization of triblock copolymers. We have studied 2 types of triblock copolymers: ABA and BAB, where A is the crystallizable block and B is the non-crystallizable block, and we have compared this to the crystallization of a completely crystallizable single-chain polymer of equal molecular weight. We tailor these polymers to have attractive and repulsive A-B interactions, and attractive and repulsive B-solvent interactions. We find that the interactions between A and B blocks greatly affect the melting points and the final crystalline morphology of the A block or blocks. Overall, the melting points of all systems agree qualitatively with Flory's prediction of a depression in melting point when blocky impurities are present [5].

In the fourth study, we have attempted to experimentally crystallize calcium oxalate and had originally aimed to study the effect of polyelectrolyte additives on

this crystallization process. We have crystallized calcium oxalate from supersaturated solutions using the experimental methodology provided in the work of Chung and co-workers [6]. Through this crystallization process, we have obtained hexagonal crystals as observed under an optical microscope, which matches the work of Chung and co-workers.

In the fifth work, we have investigated the effect of branches on the crystallization of linear polymers. Branches are known to cause a depression in the melting point of polymers from Flory's theory [5]. However, the effect of branches on the kinetics of crystallization is not known. We have investigated the effect of density of branches on crystallization. We find that when the branches are separated by 21 monomers, and restricted to one end of the polymer, the branches disrupt the crystallinity of the baby nuclei during the early stages of the crystallization. When the branches are spread out across the the polymer with a similar frequency, they disrupt the crystallinity of all the baby nuclei, leading to the formation of a globular aggregate. However, when the branches are far apart, they do not disrupt the crystallization process. In all the cases where the polymer successfully forms a crystal, the branches get expelled to the periphery of the crystal.

7.2 Future work

We recommend several areas of possible future investigations for all of our work. The effect of the several metastable lamellar thicknesses on the melting of ring polymers must be understood. The melting of simple linear polymers itself produced interesting metastable states, with small free energy barriers during the process. Melting the more entropically-constrained ring polymer system and trying to understand the kinetics of this process will help to add to the understanding of ring polymers.

We recommend several areas of work to extend our understanding of melting of linear polymers as well. Currently, our simulation model shows the existence

of metastable states, which are known to cause a memory effect by enhancing the recrystallization temperature of once-molten semicrystalline polymer in experimental systems. Therefore, one possible future step is to recrystallize the obtained melts and determine the effect of melt-memory arising from simulations of our simple molecular models. A method to determine a simulation equivalent of crystallization temperature will be required to complete this. This will ultimately help to understand melt-memory quantitatively.

We have studied melting for model polymer systems and discovered the existence of hierarchical timescales in the relaxation of the global order parameter. A systematic investigation of these hierarchical timescales will provide a multitude of valuable information. Calculations can be performed to obtain the stretched exponentials at various intermediate melting temperatures. These calculations will reveal many significant details about the nature of the metastable state and the variation in relaxation of the order parameter with melting temperature. Moreover, a theoretical understanding of these timescales will complete the understanding of melting. This can be performed by analyzing model crystals theoretically and obtaining timescales using a Fokker-Planck analysis, similar to that performed by Muthukumar [43, 50, 53, 54] for the early stage of crystallization. This will provide evidence for a particular mechanism during the melting process as well.

The inherent issues arising out of using Langevin dynamics simulations can be addressed. Langevin dynamics simulations suffer from an inherent drawback that they apply the same average temperature (within fluctuations) to all entities in the simulation. To account for this weakness of the method, we recommend a theoretical investigation to calculate the specific heat capacity of a crystalline polymer configuration and an amorphous polymer configuration by extending Debye's lattice vibration theory [183] to polymers. This theoretical investigation will enable a fundamental understanding of how heat flows in a semicrystalline polymer, and will help to the-

oretically understand how polymers conduct heat and which regions of the polymer should melt first.

We recommend several future studies for our triblock copolymer work. The timescales of crystallization should be computed for all the triblock copolymer systems. This will reveal whether the blocky interactions aid or hamper crystallization kinetics. Next, we have obtained several cases where micellization occurs. The kinetics of micellization and reverse micellization can be studied for the appropriate systems. This has been studied experimentally in the works of Lodge [184, 185] and Bansil [148, 186]. Our simulations can readily complement such experiments by revealing the molecular mechanisms of such transitions. Additionally, the effect of the impurities on the early stage kinetics can also be determined by computing the structure factors at early times during the crystallization process. This will elucidate the mechanism of early stage nucleation for these triblock copolymers, which have blocky impurities. Lastly, this model can easily be extended to study the crystallization of patterned polymers. This will help to understand crystallization in biologically relavant systems like Mucin or DNA, in which the backbone is patterned by different bases.

Further, we recommend future experimental investigations to understand the effect of additives on calcium oxalate crystallization, and to understand the nature of interaction between calcium oxalate and polyelectrolytes of different charges. To understand why only anionic polyelectrolytes affect the crystallization of calcium oxalate, the effect of zwitterionic polyelectrolytes can be studied under physiological conditions. This will significantly advance the existing fundamental understanding of therapeutics for kidney stone disease.

Lastly, we recommend future simulations to extend our branched polymer work. The effect of branches on the early stage mechanism needs to be quantified by measuring the timescales and by computing the structure factors. The mean-squared

displacement of the monomers along the backbone and the chain should also be monitored. This will enable us to understand the difference in monomer movement, which is caused due to the presence of branches. Lastly, the melting temperatures should be estimated for all the cases of the branched polymers so as to complete our characterization of the system.

APPENDIX A

FORCES ARISING FROM THE ANGULAR POTENTIALS

The calculation of the forces due to each of the potentials in the system is the first step for the Velocity-Verlet algorithm to proceed. The force $\vec{F}$ arising from any potential $U(\vec{r})$ is given by:

$$\vec{F}(\vec{r}) = -\nabla_{\vec{r}} U(\vec{r}). \tag{A.1}$$

In the case of the bond potential and the Lennard Jones Potential, the calculation of the force F due to each of these potentials is a relatively straightforward exercise because they are both functions of $\vec{r}$. But for the calculation of the forces arising from the bond angle potential and the dihedral angle potentials, the mathematics involved is not straightforward. Moreover, owing to the high values of the spring constants, an improper calculation of these forces will lead to a breakdown of the system.

Forces due to Bond Angle Potential

Figure A.1 shows a schematic diagram of the bond angle that can be obtained when the bond vectors are defined from the i^{th} bead to the $(i+1)^{th}$ bead. The cosine of the angle θ is given by:

$$\cos\theta = \frac{\vec{d}_{32} \cdot \vec{d}_{21}}{|\vec{d}_{32}||\vec{d}_{21}|} \tag{A.2}$$

$$\Rightarrow \cos\theta = \frac{(\vec{r_3} - \vec{r_2}) \cdot (\vec{r_2} - \vec{r_1})}{|\vec{r_3} - \vec{r_2}||\vec{r_2} - \vec{r_1}|}$$

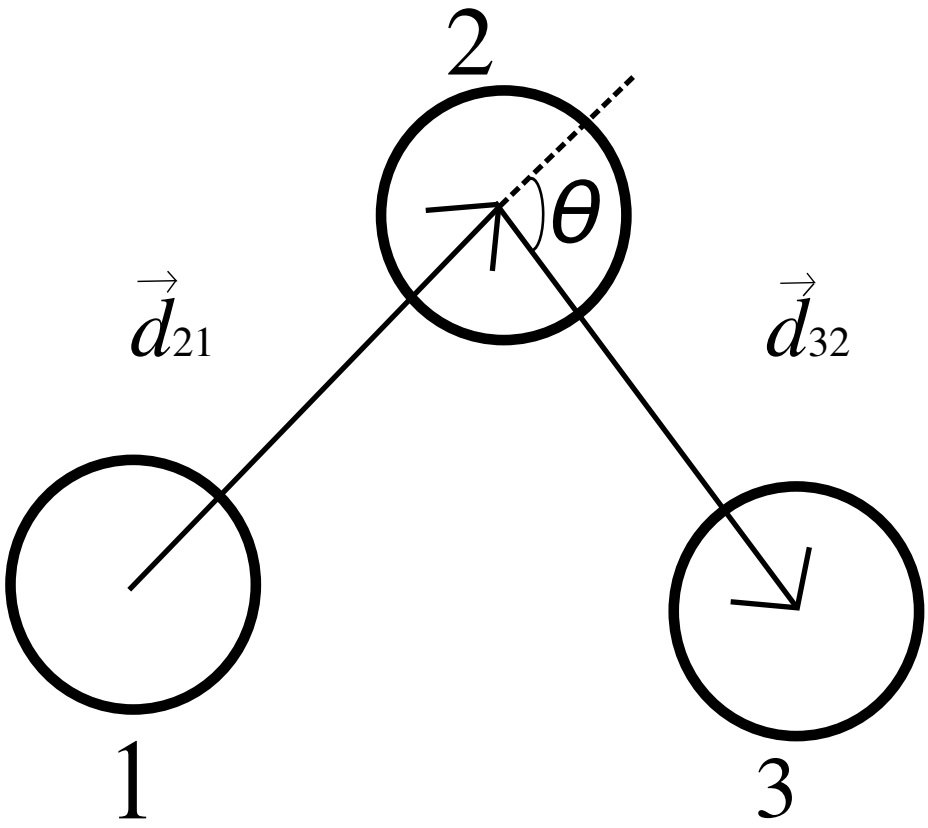

Figure A.1. Schematic diagram depicting the bond angle which will be obtained from a specific choice of bond vectors

Having established this, we can now proceed to find the individual forces on each atom. The force on atom 1 can be written as:

$$\vec{f_1} = \nabla_{\vec{r}_1} U$$
$$\Rightarrow \vec{f_1} = -\frac{\partial U}{\partial \cos\theta}\frac{\partial \cos\theta}{\partial \vec{r_1}} \tag{A.3}$$
$$\tag{A.4}$$

The first term is easy to evaluate. The second term requires some vector calculus to be performed on the $\cos\theta$. Upon performing the vector differentiation, we obtain the following result

$$\vec{f_1} \;=\; -2k_\theta\left(\cos\theta - \cos\theta_0\right)\left(\frac{(\vec{r_3}-\vec{r_2})\cdot(\vec{r_2}-\vec{r_1})}{|\vec{r_3}-\vec{r_2}||\vec{r_2}-\vec{r_1}|^3}\vec{d}_{21} + \vec{r_2} - \vec{r_3}|\vec{r_3}-\vec{r_2}||\vec{r_2}-\vec{r_1}|\right) \tag{A.5}$$

A similar analysis will yield the force on atom 3, $\vec{f_3}$. The force on atom 2 can then be found by summing these forces to zero:

$$\vec{f_1} + \vec{f_2} + \vec{f_3} = \vec{0} \tag{A.6}$$

Forces due to Dihedral Angle Potential

In a way similar to how the forces due to the bond angles were resolved, the forces due to dihedral angle shall also be computed.

Figure A.2 shows a schematic description of the dihedral angle between a quadruplet of beads. The dihedral angle ϕ is then given by the relation:

$$\cos\phi = \frac{(\vec{r}_{12}\times\vec{r}_{32})\cdot(\vec{r}_{32}\times\vec{r}_{43})}{|\vec{r}_{12}\times\vec{r}_{32}||\vec{r}_{32}\times\vec{r}_{43}|} \tag{A.7}$$

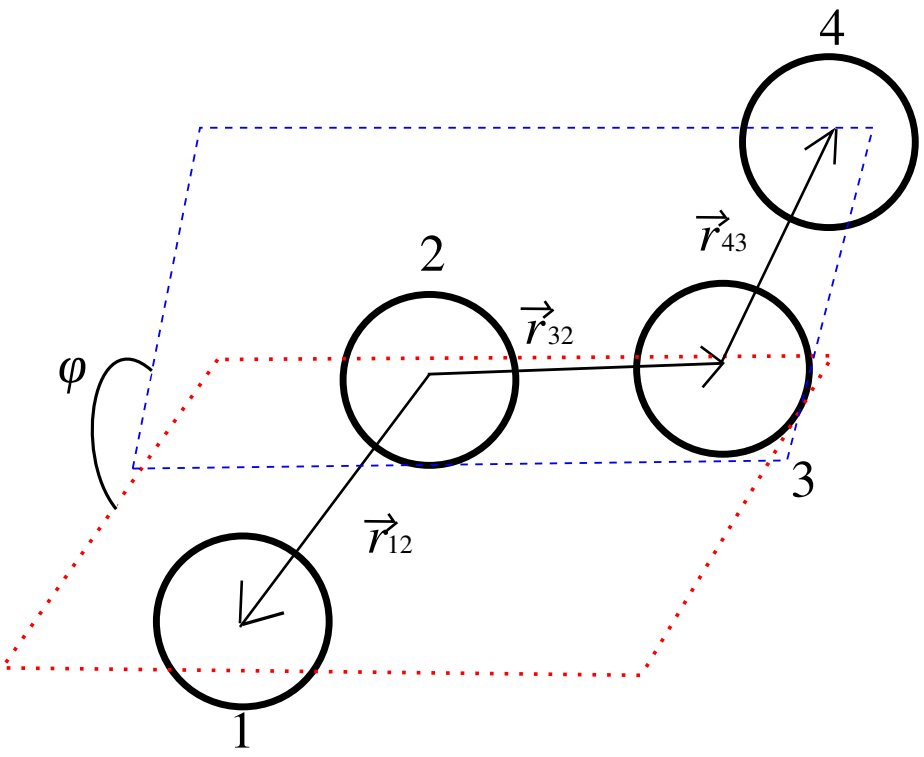

Figure A.2. Schematic diagram depicting the dihedral angle which will be obtained from a specific choice of bond vectors

The force on bead 1, $\vec{f_1}$, is then given by

$$\vec{f_1} = -\nabla_{\vec{r}_1} U \tag{A.8}$$

$$\Rightarrow \vec{f_1} = -\frac{\partial U}{\partial \cos\phi} \nabla_{\vec{r}_1} \cos\phi \tag{A.9}$$

The first term in the above expression is easy to compute. For the second term, vector derivatives need to be computed. Once those are computed, the force on the first bead is given by

$$\begin{aligned}\vec{f_1} = &\left(k_1 + 4k_2\cos\phi + 12k_3\cos^2\phi - 3k_3\right) \times \\ &\left(\frac{(\vec{r}_{12}\times\vec{r}_{32})\cdot(\vec{r}_{32}\times\vec{r}_{43})}{|\vec{r}_{32}\times\vec{r}_{43}|\left(|\vec{r}_{12}|^2|\vec{r}_{32}|^2 - (\vec{r}_{12}\cdot\vec{r}_{32})^2\right)^{\frac{3}{2}}} \left((\vec{r}_{12}\cdot\vec{r}_{32})\,\vec{r}_{32} - |\vec{r}_{32}|^2\vec{r}_{12}\right) \right. \\ &\left. + \frac{(\vec{r}_{32}\cdot\vec{r}_{43})\,\vec{r}_{32} - |\vec{r}_{32}|^2\vec{r}_{43}}{|\vec{r}_{12}\times\vec{r}_{32}||\vec{r}_{32}\times\vec{r}_{43}|} \right)\end{aligned} \tag{A.10}$$

A similar analysis will give the force on bead 4, $\vec{f_4}$. The forces on beads 2 and 3, $\vec{f_2}$ and $\vec{f_3}$ are found by balancing the forces and the torques on the quadruplet:

$$\vec{f_1} + \vec{f_2} + \vec{f_3} + \vec{f_4} = \vec{0} \tag{A.11}$$

$$(-\vec{r}_{12} + \vec{r}_{32}) \times \vec{f_1} + \vec{r}_{32} \times \vec{f_2} - \vec{r}_{43} \times \vec{f_4} = \vec{0} \tag{A.12}$$

Solving these together will give the value of the forces on each atom.

APPENDIX B

ALGORITHM TO GENERATE THE STARTING CONFIGURATION

Algorithm for linear polymer

Owing to the high values of the spring constants, it was observed that starting from any random configuration led to failure of the integration algorithm. To prevent this, an algorithm was designed to generate configurations of stretched chains which would have the following configuration:

1. Distance between atoms being 1 unit
2. All bond angles being 109^{o}
3. All dihedral angles being 120^{o}

This algorithm works for N beads, and is as follows:

1. Provide starting coordinates for the first two beads and a starting unit vector along the x-axis.
2. Fix a starting rotation matrix R_n to be the identity matrix I_3.
3. Fix the rotation matrix about the z-axis (R_z) by using the value of the angle in the components of the matrix to be the value of $180 - \theta$ (convert to radians) where θ is the desired bond angle.
4. Fix the rotation matrix about the x-axis (R_x) by using the value of the angle in the components of the matrix to be the value of ϕ (convert to radians) where ϕ is the desired dihedral angle.

5. Determine the new rotation matrix by multiplying the old rotation matrix by R_z and then R_x.

6. Determine the new unit vector by pre-multiplying the old unit vector by the rotation matrix obtained in step 5.

7. Find the coordinates of the new bead by adding the unit vector obtained in step 6 to the coordinates of the previous bead.

8. Repeat steps 5-7 for $N-2$ beads.

This algorithm can then be generalized by using random number generators to pick bond angles, because the bond angle can either be θ or $-\theta$.

Algorithm for branched polymer

We make a starting configuration for a branched polymer in two steps: for the first step, repeat the procedure and obtain the linear portion of the configuration and output that to a file. Then, parse through this file using another program, and at the branch points (excluding the first and last monomer), advance in the z-axis by 1 unit and then implement rotations about the z-axis. To summarize

1. Once branch point has been found, advance in the z-axis by 1 unit to obtain the first monomer.

2. Fix the rotation matrix about the z-axis (R_z) by using the value of the angle in the components of the matrix to be the value of $180-\theta$ where θ is the desired bond angle.

3. Fix the rotation matrix about the y-axis (R_y) by using the value of the angle in the components of the matrix to be the value of $180-\theta$ where θ is the desired bond angle.

4. Determine the new rotation matrix by multiplying $R_y \times R_z$ to the unit vector.

5. Advance along the obtained unit vector by 1 unit.

6. Repeat steps 2-5 until the number of branches has been reached.

Algorithm for ring polymer

We will generate ring polymers by generating 4 different linear sequences and then combining them. There will be a small imperfection in the structure, but this imperfection does not affect the simulation itself. This structure is sufficiently close to equilibrium for the simulation to remain stable.

To generate a ring polymer consisting of N monomers (N has to be even), we generate two parallel linear sequences just like that described in Section B for $\frac{N}{2} - 4$ monomers each time, then two perpendicular linear sequences like that described in Section B to generate 4 monomers each. We describe the detail below:

1. Generate $\frac{N}{2} - 4$ monomers using the algorithm given in Section B, with the two starting coordinates as (0,0,0) and (1,0,0), and the starting unit vector along the x-axis.

2. Pick the last monomer generated in step 1, and advance along the z-axis by 1 unit to generate one more monomer.

3. Define R_z using θ as the rotation angle, and R_x using ϕ as the rotation angle. Now execute rotations using $R_x \times R_z$ and generate 3 monomers, and output the necessary monomers to file.

4. Pick the first monomer in step 1, advance along the z-axis by 1 unit and repeat step 3 to generate 4 perpendicular monomers.

5. Pick the last monomer generated in step 4, and advance along the x-axis by 1 unit.

6. Repeat step 1 to generate $\frac{N}{2} - 4$ monomers.

7. Reverse the direction of the monomers generated in step 6, and the 4 monomers generated in step 4.

8. Combine the monomers generated in steps 1, 3, and 7 in exactly that order to generate an acceptable structure for a ring.

APPENDIX C

SUPPLEMENTARY INFORMATION FOR LANGEVIN DYNAMICS SIMULATION OF CRYSTALLIZATION OF RING POLYMER

C.1 General crystallization procedure

C.1.1 Linear polymer

The process of primary nucleation was studied in the linear polymer. The polymer was equilibrated at a temperature of $T^* = 12$, until "smectic pearls" were formed, and then quenched to a temperature of $T^* = 9$. The polymer in 'Linear_single' is extended at the beginning of the simulation, and it goes on to achieve a folded lamellar structure.

C.1.2 Ring polymer

A process similar to obtaining the linear polymer crystal was carried out to crystallize the ring polymer as well. The polymer was started from an extended structure and equilibrated to $T^* = 12$ until some parts of the chain visually started to interact with one another. Subsequently, the polymer in 'Ring_single' was quenched to a temperature of $T^* = 9$. The video clearly shows the development of baby nuclei along the backbone, and the formation of the folded lamellar structure.

C.2 Secondary nucleation

C.2.1 Linear polymers

An equilibrated linear chain of 200 monomers at $T^* = 12$ is brought within $3r_0$ to a pre-formed crystal consisting of 19 polymers of 200 monomers each. The entire

system is then allowed to equilibrate at $T^* = 9$. The attached video 'Linear_addition' shows that the extended linear chain adds on to the crystal rapidly.

C.2.2 Ring polymers

An equilibrated linear chain of 200 monomers at $T^* = 12$ is brought within $3r_0$ to a pre-formed crystal consisting of 19 polymers of 200 monomers each. The entire system is then allowed to equilibrate at $T^* = 7.79$. The attached video 'Ring_addition' shows that the extended ring polymer struggles to orient itself correctly and only then adds on to the crystallographic registry.

C.3 Lamellar thicknesses of crystallites

C.3.1 Linear polymer crystals

The following table (Table C.1) shows all the dimensions of the crystals used to determine the melting point of the linear polymers.

C.3.2 Ring polymer crystals

The following table (Table C.2) shows all the dimensions of the crystals used to determine the melting point of the ring polymers.

C.4 Structure factors without baseline correction

To get a sense of the structure factors shown in Figure 2.4, Figure 2.6a, and Figure 2.6b, we show the structure factors without correcting for the baseline in the following figures. Figure C.1 shows the structure factors for the linear polymers crystallized at $T^* = 9$. Figure C.2 shows the structure factors for the ring polymers crystallized at $T^* = 9$. Figure C.3 shows the structure factors for the ring polymers crystallized at $T^* = 7.79$.

Table C.1. Dimensions of the linear polymer crstals

Crystal	Lamellar thickness	Crystal width	Crystal depth
1	10.65	6.69	9.63
2	10.17	5.56	9.88
3	11.00	5.88	9.52
4	10.48	5.64	9.91
5	12.16	4.59	12.07
6	12.33	7.37	10.74
7	9.72	5.31	9.54
8	10.19	5.79	9.07
9	12.19	5.15	11.48
10	11.26	5.87	10.14
11	14.21	4.30	14.16
12	12.25	5.63	10.89
13	12.03	7.27	9.43
14	10.40	5.18	9.93
15	11.08	5.10	10.89
Average	11.34	5.69	10.48
Standard deviation	1.19	0.87	1.31

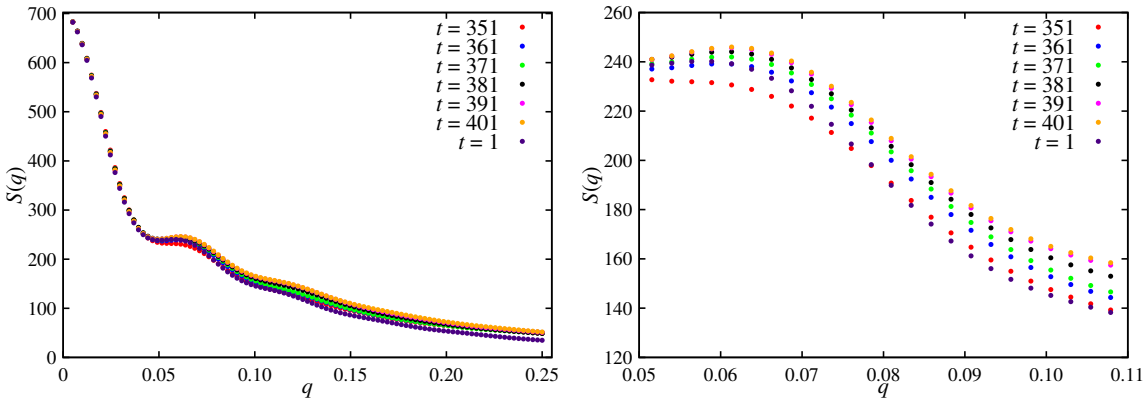

(a) Actual structure factors

(b) Structure factors for the relevant q range

Figure C.1. Structure factors without baseline correction for the linear polymer cystallized at $T^* = 9$.

Table C.2. Dimensions of the ring polymer crystals

Crystal	Lamellar thickness	Crystal width	Crystal depth
1	10.03	5.30	9.03
2	9.71	5.70	9.26
3	14.04	4.04	13.88
4	9.20	5.055	9.01
5	12.11	5.02	11.76
6	10.35	5.67	8.82
7	9.62	6.88	8.52
8	10.07	5.90	9.05
9	10.23	5.13	9.21
10	9.60	5.31	8.82
11	11.49	4.85	10.68
12	10.84	6.59	9.52
13	12.57	6.07	10.74
14	12.32	4.36	12.17
15	11.11	7.60	9.46
Average	10.89	5.56	10.00
Standard deviation	1.37	0.95	1.54

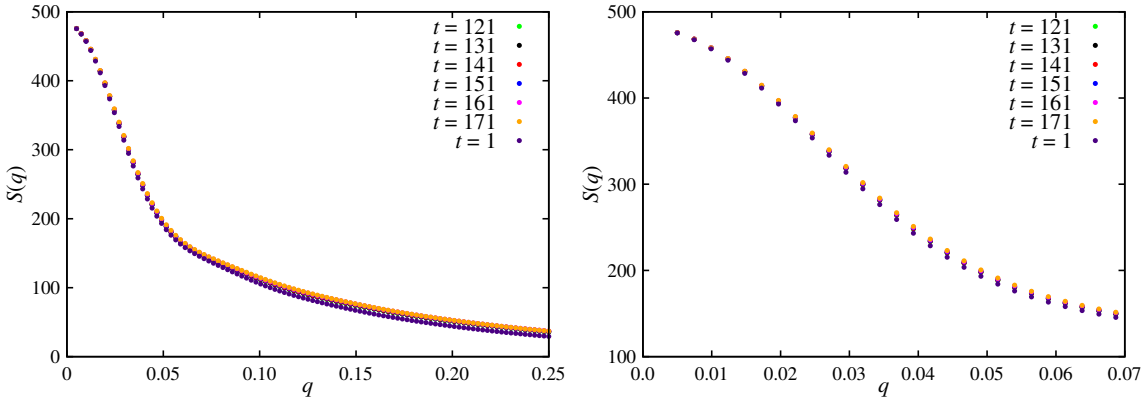

(a) Actual structure factors

(b) Structure factors for the relevant q range

Figure C.2. Structure factors without baseline correction for the ring polymer crystallized at $T^* = 9$.

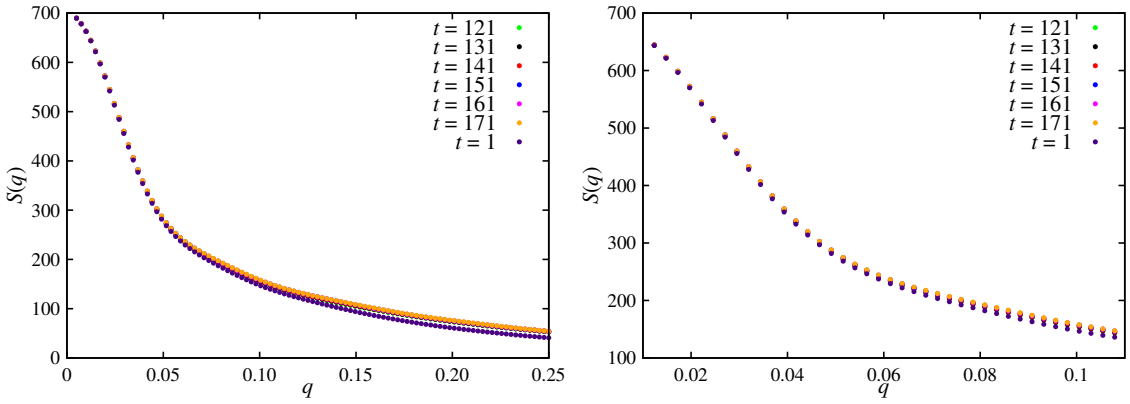

(a) Actual structure factors

(b) Structure factors for the relevant q range

Figure C.3. Structure factors without baseline correction for the ring polymer crystallized at $T^* = 9$.

C.5 Raw structure factors without smoothening

The baseline-corrected structure factors shown in Figure 2.4, Figure 2.6a, and Figure 2.6b have been plotted after smoothening using the cubic spline smoothening function provided by gnuplot. The raw data without the smoothening is shown in the Figure C.4, FIG. C.5, and Figure C.6.

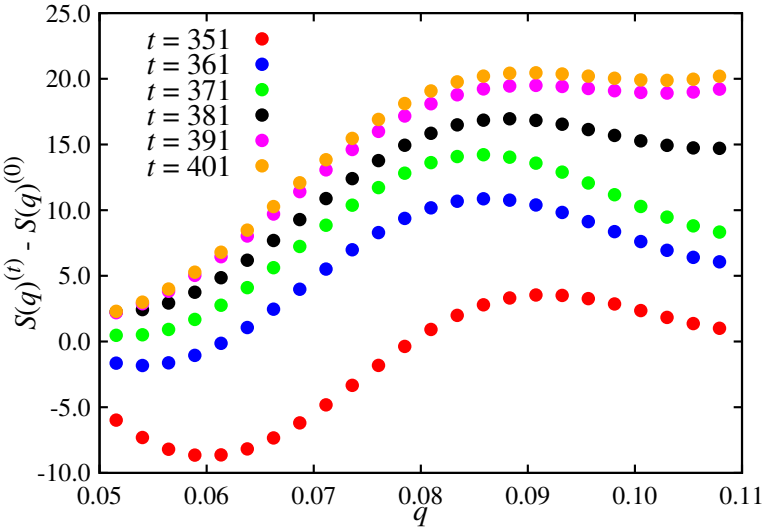

Figure C.4. Baseline-corrected structure factors for the linear polymer crystallized at $T^* = 9$, without smoothening.

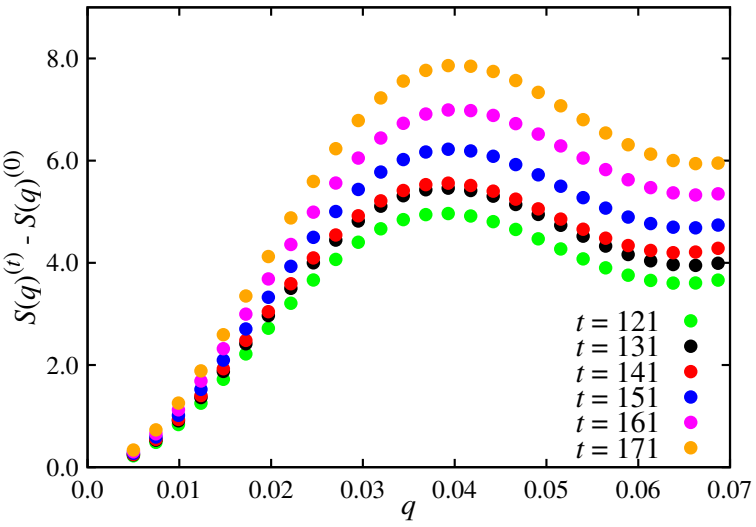

Figure C.5. Baseline-corrected structure factors for the ring polymer crystallized at $T^* = 9$, without smoothening.

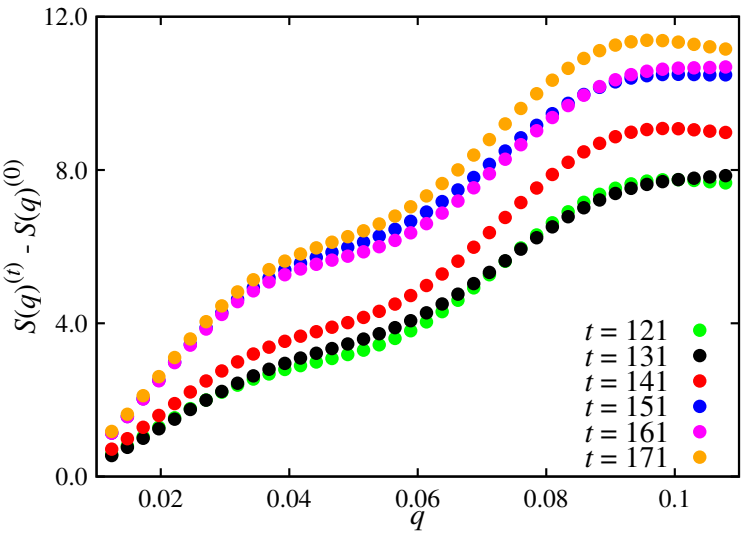

Figure C.6. Baseline-corrected structure factors for the ring polymer crystallized at $T^* = 7.79$, without smoothening.

APPENDIX D

SUPPLEMENTARY INFORMATION FOR INTERLUDE OF METASTABILITY IN THE MELTING OF POLYMER CRYSTALS

D.1 General parellel tempering procedure

In the parallel tempering method that is used with the Langevin dynamics simulation, the key variable of importance is the frequency of the swap step. If the frequency is very high, then the crystalline regions of the landscape can get oversampled. On the other hand, if the frequency is very low, then the entire melting process might get skipped and the sampling would be over the non-equilibrium process. The sampling frequencies t_{swap} have been chosen to optimize the above two constraints of the system, and in keeping with the sampling frequency of Mahalik and Muthukumar[135].

The melting times were determined for each system by observing the evolution of the global order parameter P_2, and finding the minimum time when it passes a threshold value of 0.1. This set the minimum time within which to swap the configurations. Each melting temperature was then run for a specific number of Langevin dynamics timesteps(t_{langevin}). The following table (Table D.1) describes the sampling frequencies of each temperature, and compares them to the melting times. The melting time at the temperature of $T^* = 11.6$ could not be computed as the system did not reach a threshold value of $P_2 = 0.1$.

Table D.1. Swapping frequencies and melting times at each temperature

Crystal	Melting temperature	Melting time	Parallel tempering run time	Swapping frequency	Number of simulations
Single	12	240	5000	50	100
Single	14	29	100	5	250
Single	16	17	50	0.5	500
Single	18	12.5	50	0.5	500
Single	20	8.5	50	0.5	500
Aggregate	11	N.A	5000	50	20
Aggregate	11.6	N.A	5000	50	20
Aggregate	12	3600	5000	50	40
Aggregate	14	110	200	5	60
Aggregate	16	38	90	1	60
Aggregate	18	22	60	1	60
Aggregate	20	15	60	1	60

D.2 The reaction coordinate $m_{\mathbf{amorphous}}$

To show the validity of the choice of the cut-off radius and the threshold value of the local order parameter to define whether a monomer is crystalline or amorphous, we show two instances with the amorphous and the crystalline monomers marked separately. Figure D.1 shows such an example. It can be seen that the choice of parameters for the cut-off radius (6.5), and the threshold P_2 value (0.5) ensure that the crystalline and the amorphous monomers are identified appropriately.

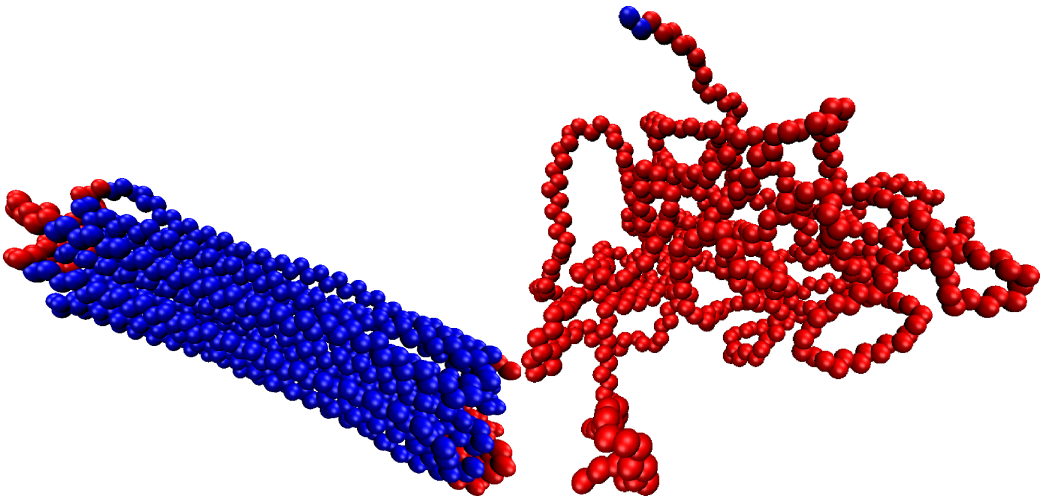

(a) $m_{\text{amorphous}} = 83$ (b) $m_{\text{amorphous}} = 698$

Figure D.1. Number of amorphous monomers in the crystalline state (83) as shown in (a), and the amorphous state (698) as shown in (b). The monomers marked in blue show the crystalline monomers, while the monomers in red show amorphous monomers.

BIBLIOGRAPHY

[1] J. D. Hoffman. Theoretical aspects of polymer crystallization with chain folds: Bulk polymers. *Polymer Engineering & Science*, 4(4):315–362, 1964.

[2] John I. Lauritzen and John D. Hoffman. Theory of formation of polymer crystals with folded chains in dilute solution. *Journal of Research of the National Bureau of Standards Section A*, 64A(1):73, 1960.

[3] John D. Hoffman and James J. Weeks. Melting process and the equilibrium melting temperature of polychlorotrifluoroethylene. *Journal of Research of the National Bureau of Standards Section A: Physics and Chemistry*, 66A(1):13, jan 1962.

[4] Gunter Reiter. Some unique features of polymer crystallisation. *Chem. Soc. Rev.*, 43:2055–2065, 2014.

[5] Paul J. Flory. *Principles of polymer chemistry*. Cornell University Press, 1953.

[6] Jihae Chung, Michael G. Taylor, Ignacio Granja, John R. Asplin, Giannis Mpourmpakis, and Jeffrey D. Rimer. Factors differentiating the effectiveness of polyprotic acids as inhibitors of calcium oxalate crystallization in kidney stone disease. *Crystal Growth & Design*, 18(9):5617–5627, 2018.

[7] M. Muthukumar and P. Welch. Modeling polymer crystallization from solutions. *Polymer*, 41(25):8833–8837, 2000.

[8] Bruno H. Zimm and Walter H. Stockmayer. The dimensions of chain molecules containing branches and rings. *The Journal of Chemical Physics*, 17(12):1301–1314, 1949.

[9] M. Kapnistos, M. Lang, D. Vlassopoulos, W. Pyckhout-Hintzen, D. Richter, D. Cho, T. Chang, and M. Rubinstein. Unexpected power-law stress relaxation of entangled ring polymers. *Nature Materials*, 7(12):997–1002, oct 2008.

[10] Yuya Doi, Kazuki Matsubara, Yutaka Ohta, Tomohiro Nakano, Daisuke Kawaguchi, Yoshiaki Takahashi, Atsushi Takano, and Yushu Matsushita. Melt rheology of ring polystyrenes with ultrahigh purity. *Macromolecules*, 48(9): 3140–3147, 2015.

[11] P.G. de Gennes. *Scaling Concepts in Polymer Physics*. Cornell University Press, 1979.

[12] M. Doi and S.F. Edwards. *The Theory of Polymer Dynamics*. International series of monographs on physics. Clarendon Press, 1988.

[13] Yanfei Li, Kai-Wen Hsiao, Christopher A. Brockman, Daniel Y. Yates, Rae M. Robertson-Anderson, Julia A. Kornfield, Michael J. San Francisco, Charles M. Schroeder, and Gregory B. McKenna. When ends meet: Circular dna stretches differently in elongational flows. *Macromolecules*, 48(16):5997–6001, 2015.

[14] Jonathan D. Halverson, Won Bo Lee, Gary S. Grest, Alexander Y. Grosberg, and Kurt Kremer. Molecular dynamics simulation study of nonconcatenated ring polymers in a melt. ii. dynamics. *The Journal of Chemical Physics*, 134 (20):204905, 2011.

[15] Rae M. Robertson, Stephan Laib, and Douglas E. Smith. Diffusion of isolated dna molecules: Dependence on length and topology. *Proceedings of the National Academy of Sciences*, 103(19):7310–7314, 2006.

[16] Rae M. Robertson and Douglas E. Smith. Strong effects of molecular topology on diffusion of entangled dna molecules. *Proceedings of the National Academy of Sciences*, 104(12):4824–4827, 2007.

[17] Jonathan D. Halverson, Won Bo Lee, Gary S. Grest, Alexander Y. Grosberg, and Kurt Kremer. Molecular dynamics simulation study of nonconcatenated ring polymers in a melt. i. statics. *The Journal of Chemical Physics*, 134(20): 204904, 2011.

[18] Edward F. Casassa. Some statistical properties of flexible ring polymers. *Journal of Polymer Science Part A: General Papers*, 3(2):605–614, 1965.

[19] M.E. Cates and J.M. Deutsch. Conjectures on the statistics of ring polymers. *J. Phys. France*, 47(12):2121–2128, 1986.

[20] Rossana Pasquino, Thodoris C. Vasilakopoulos, Youn Cheol Jeong, Hyojoon Lee, Simon Rogers, George Sakellariou, Jürgen Allgaier, Atsushi Takano, Ana R. Brás, Taihyun Chang, Sebastian Gooßen, Wim Pyckhout-Hintzen, Andreas Wischnewski, Nikos Hadjichristidis, Dieter Richter, Michael Rubinstein, and Dimitris Vlassopoulos. Viscosity of ring polymer melts. *ACS Macro Letters*, 2(10):874–878, 2013.

[21] Chahrazed Meddah, Andrey Milchev, Sid Ahmed Sabeur, and Alexander M. Skvortsov. Molecular weight effects on interfacial properties of linear and ring polymer melts: A molecular dynamics study. *The Journal of Chemical Physics*, 145(19):194902, 2016.

[22] Jacques Roovers. *Overview on physical properties of cyclic polymers*. World Scientific Publishing Co. Pte. Ltd.: Singapore, 2013.

[23] Ricardo A. Pérez-Camargo, Agurtzane Mugica, Manuela Zubitur, and Alejandro J. Müller. *Crystallization of Cyclic Polymers*, pages 93–132. Springer International Publishing, Cham, 2017.

[24] Christopher W. Bielawski, Diego Benitez, and Robert H. Grubbs. An "endless" route to cyclic polymers. *Science*, 297(5589):2041–2044, 2002.

[25] Zhongfan Jia and Michael J. Monteiro. Cyclic polymers: Methods and strategies. *Journal of Polymer Science Part A: Polymer Chemistry*, 50(11):2085–2097, 2012.

[26] R.A. Pérez, M.E. Córdova, J.V. López, J.N. Hoskins, B. Zhang, S.M. Grayson, and A.J. Müller. Nucleation, crystallization, self-nucleation and thermal fractionation of cyclic and linear poly(ϵ-caprolactone)s. *Reactive and Functional Polymers*, 80:71 – 82, 2014. Cyclic polymers: New developments.

[27] Hsuan-Han Su, Hsin-Lung Chen, Angélica Díaz, María Teresa Casas, Jordi Puiggalí, Jessica N. Hoskins, Scott M. Grayson, Ricardo A. Pérez, and Alejandro J. Müller. New insights on the crystallization and melting of cyclic {PCL} chains on the basis of a modified thomson-gibbs equation. *Polymer*, 54(2):846 – 859, 2013.

[28] Miguel E. Córdova, Arnaldo T. Lorenzo, Alejandro J. Müller, Jessica N. Hoskins, and Scott M. Grayson. A comparative study on the crystallization behavior of analogous linear and cyclic poly(ϵ-caprolactones). *Macromolecules*, 44(7):1742–1746, 2011.

[29] Kerstin Schäler, Elena Ostas, Klaus Schröter, Thomas Thurn-Albrecht, Wolfgang H. Binder, and Kay Saalwächter. Influence of chain topology on polymer dynamics and crystallization. investigation of linear and cyclic poly(ϵ-caprolactone)s by 1h solid-state nmr methods. *Macromolecules*, 44(8):2743–2754, 2011.

[30] Ricardo A. Pérez, Juan V. López, Jessica N. Hoskins, Boyu Zhang, Scott M. Grayson, María Casas Teresa, Jordi Puiggalí, and Alejandro J. Müller. Nucleation and antinucleation effects of functionalized carbon nanotubes on cyclic and linear poly(ϵ-caprolactones). *Macromolecules*, 47(11):3553–3566, 2014.

[31] Zhaolei Li, Jing Wang, Ricardo A Pérez-Camargo, Alejandro J Müller, Boyu Zhang, Scott M Grayson, and Wenbing Hu. Non-monotonic molecular weight dependence of crystallization rates of linear and cyclic poly(epsilon-caprolactone)s in a wide temperature range. *Polymer International*, 65(9): 1074–1079, 2016.

[32] Jing Wang, Zhaolei Li, Ricardo A. Pérez, Alejandro J. Müller, Boyu Zhang, Scott M. Grayson, and Wenbing Hu. Comparing crystallization rates between linear and cyclic poly(epsilon-caprolactones) via fast-scan chip-calorimeter measurements. *Polymer*, 63:34 – 40, 2015.

[33] George Zardalidis, Julian Mars, Jurgen Allgaier, Markus Mezger, Dieter Richter, and George Floudas. Influence of chain topology on polymer crystallization: poly(ethylene oxide) (peo) rings vs. linear chains. *Soft Matter*, 12: 8124–8134, 2016.

[34] Eun Ji Shin, Wonhee Jeong, Hayley A. Brown, Bon Jun Koo, James L. Hedrick, and Robert M. Waymouth. Crystallization of cyclic polymers: Synthesis and crystallization behavior of high molecular weight cyclic poly(ϵ-caprolactone)s. *Macromolecules*, 44(8):2773–2779, 2011.

[35] Yasuyuki Tezuka, Tatsuroh Ohtsuka, Kaoru Adachi, Ryota Komiya, Noriyoshi Ohno, and Norimasa Okui. A defect-free ring polymer: Size-controlled cyclic poly(tetrahydrofuran) consisting exclusively of the monomer unit. *Macromolecular Rapid Communications*, 29(14):1237–1241, 2008.

[36] Tsunaki Kitahara, Shinichi Yamakazi, and Kunio Kimura. Effects of topological constraint and knot entanglement on the crystal growth of polymers proved by growth rate of spherulite of cyclic polyethylene. *Kobunshi Ronbunshu*, 68(10): 694–701, 2011.

[37] Hiroki Takeshita, Monticha Poovarodom, Takahiro Kiya, Fuminori Arai, Katsuhiko Takenaka, Masamitsu Miya, and Tomoo Shiomi. Crystallization behavior and chain folding manner of cyclic, star and linear poly(tetrahydrofuran)s. *Polymer*, 53(23):5375 – 5384, 2012.

[38] Eun Ji Shin, Alexandra E. Jones, and Robert M. Waymouth. Stereocomplexation in cyclic and linear polylactide blends. *Macromolecules*, 45(1):595–598, 2012.

[39] Naoto Sugai, Shigeo Asai, Yasuyuki Tezuka, and Takuya Yamamoto. Photoinduced topological transformation of cyclized polylactides for switching the properties of homocrystals and stereocomplexes. *Polym. Chem.*, 6:3591–3600, 2015.

[40] Haiying Li, Robert Jéröme, and Philippe Lecomte. Synthesis of tadpole-shaped copolyesters based on living macrocyclic poly(ϵ-caprolactone). *Polymer*, 47(26): 8406 – 8413, 2006.

[41] Kwang Sup Lee and Gerhard Wegner. Linear and cyclic alkanes (C_nH_{2n+2}, C_nH_{2n}) with n $>$ 100. synthesis and evidence for chain-folding. *Die Makromolekulare Chemie, Rapid Communications*, 6(3):203–208, 1985.

[42] Ga-Er Yu, Tao Sun, Ze-Gui Yan, Colin Price, Colin Booth, Jennifer Cook, Anthony J. Ryan, and Kyriakos Viras. Low-molar-mass cyclic poly(oxyethylene)s studied by raman spectroscopy, x-ray scattering and differential scanning calorimetry. *Polymer*, 38(1):35 – 42, 1997.

[43] M. Muthukumar. *Nucleation in Polymer Crystallization*, pages 1–63. John Wiley & Sons, Inc., 2004.

[44] Juan V. Lopez, Ricardo A. Perez-Camargo, Boyu Zhang, Scott M. Grayson, and Alejandro J. Muller. The influence of small amounts of linear polycaprolactone chains on the crystallization of cyclic analogue molecules. *RSC Adv.*, 6:48049–48063, 2016.

[45] Tom McLeish. Polymers without beginning or end. *Science*, 297(5589):2005–2006, 2002.

[46] Jonathan D. Halverson, Gary S. Grest, Alexander Y. Grosberg, and Kurt Kremer. Rheology of ring polymer melts: From linear contaminants to ring-linear blends. *Phys. Rev. Lett.*, 108(3), jan 2012.

[47] Sunghyun Nam, Johannes Leisen, Victor Breedveld, and Haskell W. Beckham. Melt dynamics of blended poly(oxyethylene) chains and rings. *Macromolecules*, 42(8):3121–3128, 2009.

[48] C. Liu and M. Muthukumar. Langevin dynamics simulations of early-stage polymer nucleation and crystallization. *The Journal of Chemical Physics*, 109 (6):2536–2542, 1998.

[49] P. Welch and M. Muthukumar. Molecular mechanisms of polymer crystallization from solution. *Physical Review Letters*, 87:218302, 2001.

[50] M. Muthukumar. Molecular modelling of nucleation in polymers. *Philosophical Transactions of the Royal Society of London. Series A: Mathematical, Physical and Engineering Sciences*, 361(1804):539–556, 2003.

[51] S. Balijepalli and G.C. Rutledge. Conformational statistics of polymer chains in the interphase of semi-crystalline polymers. *Computational and Theoretical Polymer Science*, 10(1–2):103 – 113, 2000.

[52] Takashi Yamamoto. Computer modeling of polymer crystallization – toward computer-assisted materials' design. *Polymer*, 50(9):1975–1985, 2009.

[53] Murugappan Muthukumar. *Shifting Paradigms in Polymer Crystallization*, pages 1–18. Springer Berlin Heidelberg, Berlin, Heidelberg, 2007.

[54] M. Muthukumar. *Modeling Polymer Crystallization*, pages 241–274. Springer Berlin Heidelberg, Berlin, Heidelberg, 2005.

[55] I. Dukovski and M. Muthukumar. Langevin dynamics simulations of early stage shish-kebab crystallization of polymers in extensional flow. *The Journal of Chemical Physics*, 118(14):6648–6655, 2003.

[56] M. Imai, K. Kaji, T. Kanaya, and Y. Sakai. Ordering process in the induction period of crystallization of poly(ethylene terephthalate). *Physical Review B*, 52: 12696–12704, 1995.

[57] M. Imai, K. Mori, T. Mizukami, K. Kaji, and T. Kanaya. Structural formation of poly (ethylene terephthalate) during the induction period of crystallization: 1. ordered structure appearing before crystal nucleation. *Polymer*, 33(21):4451–4456, 1992.

[58] S. Gautam, S. Balijepalli, and G. C. Rutledge. Molecular simulations of the interlamellar phase in polymers: Effect of chain tilt. *Macromolecules*, 33(24): 9136–9145, 2000.

[59] Richard H. Gee, Naida Lacevic, and Laurence E. Fried. Atomistic simulations of spinodal phase separation preceding polymer crystallization. *Nature Materials*, 5(1):39–43, dec 2005.

[60] Hongyi Xiao, Chuanfu Luo, Dadong Yan, and Jens-Uwe Sommer. Molecular dynamics simulation of crystallization cyclic polymer melts as compared to their linear counterparts. *Macromolecules*, 50(24):9796–9806, 2017.

[61] Wolfgang Paul, Do Y. Yoon, and Grant D. Smith. An optimized united atom model for simulations of polymethylene melts. *The Journal of Chemical Physics*, 103(4):1702–1709, 1995.

[62] Murugappan Muthukumar. *Polymer translocation*. Taylor & Francis, Boca Raton, 2011.

[63] M. R. Pear and J. H. Weiner. Brownian dynamics study of a polymer chain of linked rigid bodies. *The Journal of Chemical Physics*, 71(1):212–224, 1979.

[64] D. C. Rapaport. *The art of molecular dynamics simulation*. Cambridge University Press, Cambridge, UK New York, NY, 2004.

[65] M. P. Allen and D. J. Tildesley. *Computer simulation of liquids*. Clarendon Press Oxford University Press, Oxford England New York, 1989.

[66] M. Imai, K. Mori, T. Mizukami, K. Kaji, and T. Kanaya. Structural formation of poly(ethylene terephthalate) during the induction period of crystallization: 2. kinetic analysis based on the theories of phase separation. *Polymer*, 33(21): 4457 – 4462, 1992.

[67] William Humphrey, Andrew Dalke, and Klaus Schulten. Vmd: Visual molecular dynamics. *Journal of Molecular Graphics*, 14(1):33–38, 1996.

[68] M. Imai, K. Kaji, and T. Kanaya. Orientation fluctuations of poly(ethylene terephthalate) during the induction period of crystallization. *Phys. Rev. Lett.*, 71:4162–4165, Dec 1993.

[69] Ellen L. Heeley, C. Kit Poh, Wu Li, Anna Maidens, Wim Bras, Igor P. Dolbnya, Anthony J. Gleeson, Nicolas J. Terrill, J. Patrick A. Fairclough, Peter D. Olmsted, Rile I. Ristic, Micheal J. Hounslow, and Anthony J. Ryan. Are metastable, precrystallisation, density-fluctuations a universal phenomena? *Faraday Discuss.*, 122:343–361, 2003.

[70] Shankar Kumar, John M. Rosenberg, Djamal Bouzida, Robert H. Swendsen, and Peter A. Kollman. The weighted histogram analysis method for free-energy calculations on biomolecules. i. the method. *Journal of Computational Chemistry*, 13(8):1011–1021, 1992.

[71] Goran Ungar and Xiang-Bing Zeng. Learning polymer crystallization with the aid of linear, branched and cyclic model compounds. *Chemical Reviews*, 101 (12):4157–4188, 2001.

[72] K. Armitstead, G. Goldbeck-Wood, and A. Keller. *Macromolecules: Synthesis, Order and Advanced Properties*, chapter Polymer crystallization theories, pages 219–312. Springer Berlin Heidelberg, Berlin, Heidelberg, 1992.

[73] Arindam Kundagrami and M. Muthukumar. Continuum theory of polymer crystallization. *The Journal of Chemical Physics*, 126(14):144901, 2007.

[74] Gert Strobl. Crystallization and melting of bulk polymers: New observations, conclusions and a thermodynamic scheme. *Progress in Polymer Science*, 31(4): 398 – 442, 2006.

[75] Akihiko Toda, Masamichi Hikosaka, and Koji Yamada. Superheating of the melting kinetics in polymer crystals: a possible nucleation mechanism. *Polymer*, 43(5):1667–1679, 2002.

[76] Akihiko Toda, Isao Kojima, , and Masamichi Hikosaka. Melting kinetics of polymer crystals with an entropic barrier. *Macromolecules*, 41(1):120–127, 2008.

[77] M. Muthukumar. Communication: Theory of melt-memory in polymer crystallization. *The Journal of Chemical Physics*, 145(3):031105, 2016.

[78] Huanhuan Gao, Madhavi Vadlamudi, Rufina G. Alamo, and Wenbing Hu. Monte carlo simulations of strong memory effect of crystallization in random copolymers. *Macromolecules*, 46(16):6498–6506, 2013.

[79] Benjamin O. Reid, Madhavi Vadlamudi, Al Mamun, Hamed Janani, Huanhuan Gao, Wenbing Hu, and Rufina G. Alamo. Strong memory effect of crystallization above the equilibrium melting point of random copolymers. *Macromolecules*, 46(16):6485–6497, 2013.

[80] C. Ruiz-Orta, J.P. Fernandez-Blazquez, E.J. Pereira, and R.G. Alamo. Time-resolved {FTIR} spectroscopic study of the evolution of helical structure during isothermal crystallization of propylene 1-hexene copolymers. identification of regularity bands associated with the trigonal polymorph. *Polymer*, 52(13):2856 – 2868, 2011.

[81] K. Jeon, H. Palza, R. Quijada, and R.G. Alamo. Effect of comonomer type on the crystallization kinetics and crystalline structure of random isotactic propylene 1-alkene copolymers. *Polymer*, 50(3):832 – 844, 2009.

[82] Al Mamun, Xuejian Chen, and Rufina G. Alamo. Interplay between a strong memory effect of crystallization and liquid–liquid phase separation in melts of broadly distributed ethylene–1-alkene copolymers. *Macromolecules*, 47(22): 7958–7970, 2014.

[83] Xuejian Chen, George D. Wignall, Lilin He, Carlos Lopez-Barron, and Rufina G. Alamo. Sans evidence of liquid–liquid phase separation leading to inversion of crystallization rate of broadly distributed random ethylene copolymers. *Macromolecules*, 50(11):4406–4414, 2017.

[84] Xuejian Chen, Carlos López-Barrón, Yiming Zeng, and Rufina G. Alamo. Concentration fluctuations in the early stages of llps and partial dissolution of melt-memory in broadly distributed ethylene copolymers. *Polymer*, 148:181 – 190, 2018. ISSN 0032-3861.

[85] L. Sangroniz, R. G. Alamo, D. Cavallo, A. Santamaría, A. J. Müller, and A. Alegría. Differences between isotropic and self-nucleated pcl melts detected by dielectric experiments. *Macromolecules*, 51(10):3663–3671, 2018.

[86] Youngchul Lee and Roger S. Porter. Effects of thermal history on crystallization of poly(ether ether ketone) (peek). *Macromolecules*, 21(9):2770–2776, 1988.

[87] Y. P. Khanna and A. C. Reimschuessel. Memory effects in polymers. i. orientational memory in the molten state; its relationship to polymer structure and influence on recrystallization rate and morphology. *Journal of Applied Polymer Science*, 35(8):2259–2268, 1988.

[88] Y. P. Khanna, A. C. Reimschuessel, A. Banerjie, and C. Altman. Memory effects in polymers. ii. processing history vs. crystallization rate of nylon 6—observation of phenomenon and product behavior. *Polymer Engineering & Science*, 28 (24):1600–1606, 1988.

[89] Y. P. Khanna, R. Kumar, and A. C. Reimschuessel. Memory effects in polymers. iii. processing history vs. crystallization rate of nylon 6—comments on the origin of memory effect. *Polymer Engineering & Science*, 28(24):1607–1611, 1988.

[90] Y. P. Khanna, R. Kumar, and A. C. Reimschuessel. Memory effects in polymers. iv. processing history vs. crystallization rate—effect of polymer structure. *Polymer Engineering & Science*, 28(24):1612–1615, 1988.

[91] G. C. Alfonso and A. Ziabicki. Memory effects in isothermal crystallization ii. isotactic polypropylene. *Colloid and Polymer Science*, 273(4):317–323, Apr 1995.

[92] A. Häfele, B. Heck, T. Hippler, T. Kawai, P. Kohn, and G. Strobl. Crystallization of poly(ethylene-co-octene): Ii melt memory effects on first order kinetics. *Eur. Phys. J. E*, 16(2):217–224, 2005.

[93] A. Maus, E. Hempel, T. Thurn-Albrecht, and K. Saalwächter. Memory effect in isothermal crystallization of syndiotactic polypropylene –role of melt structure and dynamics? *Eur. Phys. J. E*, 23(1):91–101, 2007.

[94] Jianing Zhang and M. Muthukumar. Simulations of nucleation and elongation of amyloid fibrils. *The Journal of Chemical Physics*, 130(3):035102, 2009.

[95] Jessica Nasica-Labouze, Phuong H. Nguyen, Fabio Sterpone, Olivia Berthoumieu, Nicolae-Viorel Buchete, Sébastien Coté, Alfonso De Simone, Andrew J. Doig, Peter Faller, Angel Garcia, Alessandro Laio, Mai Suan Li, Simone Melchionna, Normand Mousseau, Yuguang Mu, Anant Paravastu, Samuela Pasquali, David J. Rosenman, Birgit Strodel, Bogdan Tarus, John H. Viles, Tong Zhang, Chunyu Wang, and Philippe Derreumaux. Amyloid /Symbol b protein and alzheimer's disease: When computer simulations complement experimental studies. *Chemical Reviews*, 115(9):3518–3563, 2015.

[96] K. Suehiro, H. Tanizaki, and M. Takayanagi. X-ray studies of surface melting in single crystals of linear polyethylene. *Polymer*, 17(12):1059 – 1062, 1976. ISSN 0032-3861.

[97] Y Tanabe, G.R Strobl, and E.W Fischer. Surface melting in melt-crystallized linear polyethylene. *Polymer*, 27(8):1147 – 1153, 1986. ISSN 0032-3861.

[98] Peter J. Barham and David M. Sadler. A neutron scattering study of the melting behaviour of polyethylene single crystals. *Polymer*, 32(3):393–395, 1991.

[99] P. J. Barham. *Melting of Polymer Crystals*, pages 153–158. Springer Netherlands, Dordrecht, 1993.

[100] Akihiko Toda, Chiyoko Tomita, Masamichi Hikosaka, and Yasuo Saruyama. Kinetics of irreversible melting of polyethylene crystals revealed by temperature modulated dsc. *Thermochimica Acta*, 324(1):95 – 107, 1998. ISSN 0040-6031.

[101] Akihiko Toda, Tatsuro Oda, Masamichi Hikosaka, and Yasuo Saruyama. A new method of analysing transformation kinetics with temperature modulated differential scanning calorimetry: application to polymer crystal growth. *Polymer*, 38(1):231 – 233, 1997. ISSN 0032-3861.

[102] Iwao Okazaki and Bernhard Wunderlich. Reversible local melting in polymer crystals. *Macromolecular Rapid Communications*, 18(4):313–318, 1997.

[103] Iwao Okazaki and Bernhard Wunderlich. Reversible melting in polymer crystals detected by temperature-modulated differential scanning calorimetry. *Macromolecules*, 30(6):1758–1764, 1997.

[104] Akihiko Toda, Chiyoko Tomita, Masamichi Hikosaka, and Yasuo Saruyama. Melting of polymer crystals observed by temperature modulated d.s.c. and its kinetic modelling. *Polymer*, 39(21):5093 – 5104, 1998.

[105] Wenbing Hu, Thomas Albrecht, and Gert Strobl. Reversible surface melting of pe and peo crystallites indicated by tmdsc. *Macromolecules*, 32(22):7548–7554, 1999.

[106] A. Toda and Y. Saruyama. A modeling of the irreversible melting kinetics of polymer crystals responding to temperature modulation with retardation of melting rate coefficient. *Polymer*, 42(10):4727 – 4730, 2001. ISSN 0032-3861.

[107] Masahiro Fujita and Yoshiharu Doi. Annealing and melting behavior of poly(l-lactic acid) single crystals as revealed by in situ atomic force microscopy. *Biomacromolecules*, 4(5):1301–1307, 2003.

[108] Sergei N. Maganov, Natalya A. Yerina, Goran Ungar, Darrell H. Reneker, and Dimitri A. Ivanov. Chain unfolding in single crystals of ultralong alkane $C_{390}H_{782}$ and polyethylene: An atomic force microscopy study. *Macromolecules*, 36(15):5637–5649, 2003.

[109] Yi-Xin Liu, Jian-Feng Li, Dun-Shen Zhu, Er-Qiang Chen, and Hong-Dong Zhang. Direct observation and modeling of transient nucleation in isothermal thickening of polymer lamellar crystal monolayers. *Macromolecules*, 42(8): 2886–2890, 2009.

[110] S. Rastogi, A. B. Spoelstra, J. G. P. Goossens, and P. J. Lemstra. Chain mobility in polymer systems: on the borderline between solid and melt. 1. lamellar doubling during annealing of polyethylene. *Macromolecules*, 30(25): 7880–7889, 1997.

[111] Dun-Shen Zhu, Yi-Xin Liu, An-Chang Shi, and Er-Qiang Chen. Morphology evolution in superheated crystal monolayer of low molecular weight poly(ethylene oxide) on mica surface. *Polymer*, 47(15):5239 – 5242, 2006. ISSN 0032-3861. Morphology of Crystalline Polymers: Dedicated to David Bassett on the Occasion of his Retirement.

[112] A. K. Winkel, J. K. Hobbs, and M. J. Miles. Annealing and melting of long-chain alkane single crystals observed by atomic force microscopy. *Polymer*, 41 (25):8791–8800, 2000.

[113] N. Sanz, J. K. Hobbs, and M. J. Miles. In situ annealing and thickening of single crystals of $C_{294}H_{590}$ observed by atomic force microscopy. *Langmuir*, 20 (14):5989–5997, 2004.

[114] Günter Reiter. Model experiments for a molecular understanding of polymer crystallization. *Journal of Polymer Science Part B: Polymer Physics*, 41(16): 1869–1877, 2003.

[115] Mingwen Tian and Joachim Loos. Investigations of morphological changes during annealing of polyethylene single crystals. *Journal of Polymer Science Part B: Polymer Physics*, 39(7):763–770, 2001.

[116] J.K. Hobbs. In situ atomic force microscopy of the melting of melt-crystallized polyethylene. *Polymer*, 47(15):5566–5573, 2006.

[117] Nicolas Dubreuil, Stephane Hocquet, Marcel Dosiére, and Dimitri A. Ivanov. Melting of isochronously decorated single crystals of linear polyethylene, as monitored by atomic force microscopy. *Macromolecules*, 37(1):1–5, 2004.

[118] S. Hocquet, M. Dosière, A. Thierry, B. Lotz, M. H. J. Koch, N. Dubreuil, and D. A. Ivanov. Morphology and melting of truncated single crystals of linear polyethylene. *Macromolecules*, 36(22):8376–8384, 2003.

[119] Sally J. Organ, Jamie K. Hobbs, and Mervyn J. Miles. Reorganization and melting of polyethylene single crystals: Complementary tem, dsc, and real-time afm studies. *Macromolecules*, 37(12):4562–4572, 2004.

[120] Sanjay Rastogi, Dirk R. Lippits, Gerrit W. M. Peters, Robert Graf, Yefeng Yao, and Hans W. Spiess. Heterogeneity in polymer melts from melting of polymer crystals. *Nature Materials*, 4(8):635–641, jul 2005.

[121] D. R. Lippits, S. Rastogi, and G. W. H. Höhne. Melting kinetics in polymers. *Phys. Rev. Lett.*, 96:218303, Jun 2006.

[122] Dirk R. Lippits, Sanjay Rastogi, Günther W. H. Höhne, Brahim Mezari, and Pieter C. M. M. Magusin. Heterogeneous distribution of entanglements in the polymer melt and its influence on crystallization. *Macromolecules*, 40(4):1004–1010, 2007.

[123] Sanjay Rastogi, Dirk R. Lippits, Günther W. H. Höhne, Brahim Mezari, and Pieter C. M. M. Magusin. The role of the amorphous phase in melting of linear uhmw-pe: implications for chain dynamics. *Journal of Physics: Condensed Matter*, 19(20):205122, apr 2007.

[124] Y-F. Yao, R. Graf, H. W. Spiess, D. R. Lippits, and S. Rastogi. Morphological differences in semicrystalline polymers: Implications for local dynamics and chain diffusion. *Phys. Rev. E*, 76:060801, Dec 2007.

[125] Anurag Pandey, Akihiko Toda, and Sanjay Rastogi. Influence of amorphous component on melting of semicrystalline polymers. *Macromolecules*, 44(20): 8042–8055, 2011.

[126] A. A. Minakov, A. Wurm, and C. Schick. Superheating in linear polymers studied by ultrafast nanocalorimetry. *The European Physical Journal E*, 23(1): 43, May 2007.

[127] Akihiko Toda, Ken Taguchi, Koji Nozaki, and Misuzu Konishi. Melting behaviors of polyethylene crystals: An application of fast-scan dsc. *Polymer*, 55(14): 3186 – 3194, 2014. ISSN 0032-3861.

[128] Akihiko Toda, Ken Taguchi, Kano Sato, Koji Nozaki, Masanori Maruyama, Katsuharu Tagashira, and Misuzu Konishi. Melting kinetics of it-polypropylene crystals over wide heating rates. *Journal of Thermal Analysis and Calorimetry*, 113(3):1231–1237, jan 2013.

[129] Wenbing Hu, Daan Frenkel, and Vincent B. F. Mathot. Free energy barrier to melting of single-chain polymer crystallite. *The Journal of Chemical Physics*, 118(8):3455–3457, 2003.

[130] Wenbing Hu, Daan Frenkel, and Vincent B. F. Mathot. Intramolecular nucleation model for polymer crystallization. *Macromolecules*, 36(21):8178–8183, 2003.

[131] David A. Nicholson and Gregory C. Rutledge. Analysis of nucleation using mean first-passage time data from molecular dynamics simulation. *The Journal of Chemical Physics*, 144(13):134105, 2016.

[132] Kiran Iyer and Murugappan Muthukumar. Langevin dynamics simulation of crystallization of ring polymers. *The Journal of Chemical Physics*, 148(24): 244904, 2018.

[133] David J. Earl and Michael W. Deem. Parallel tempering: Theory, applications, and new perspectives. *Phys. Chem. Chem. Phys.*, 7:3910–3916, 2005.

[134] Yuji Sugita and Yuko Okamoto. Replica-exchange molecular dynamics method for protein folding. *Chemical Physics Letters*, 314(1):141 – 151, 1999. ISSN 0009-2614.

[135] J. P. Mahalik and M. Muthukumar. Langevin dynamics simulation of polymer-assisted virus-like assembly. *The Journal of Chemical Physics*, 136(13):135101, 2012.

[136] Jeffrey R. Churchill and Francis G. Hutchinson. Biodegradable amphipathic copolymers, May 1988. US Patent 4,745,160.

[137] Jun Li, Xu Li, Xiping Ni, Xin Wang, Hongzhe Li, and Kam W. Leong. Self-assembled supramolecular hydrogels formed by biodegradable peo-phb-peo triblock copolymers and α-cyclodextrin for controlled drug delivery. *Biomaterials*, 27(22):4132 – 4140, 2006.

[138] Xian Jun Loh, Zhong-Xing Zhang, Yun-Long Wu, Tiong Soon Lee, and Jun Li. Synthesis of novel biodegradable thermoresponsive triblock copolymers based on poly[(r)-3-hydroxybutyrate] and poly(n-isopropylacrylamide) and their formation of thermoresponsive micelles. *Macromolecules*, 42(1):194–202, 2009.

[139] Naomi Sanabria-DeLong, Sarvesh K. Agrawal, Surita R. Bhatia, and Gregory N. Tew. Controlling hydrogel properties by crystallization of hydrophobic domains. *Macromolecules*, 39(4):1308–1310, Feb 2006.

[140] Sarvesh K. Agrawal, Naomi Sanabria-DeLong, Pete R. Jemian, Gregory N. Tew, and Surita R. Bhatia. Micro- to nanoscale structure of biocompatible pla-peo-pla hydrogels. *Langmuir*, 23(9):5039–5044, 2007.

[141] Sarvesh K. Agrawal, Naomi Sanabria-DeLong, Sujata K. Bhatia, Gregory N. Tew, and Surita R. Bhatia. Energetics of association in poly(lactic acid)-based hydrogels with crystalline and nanoparticle-polymer junctions. *Langmuir*, 26 (22):17330–17338, 2010.

[142] Naomi Sanabria-DeLong, Sarvesh K. Agrawal, Surita R. Bhatia, and Gregory N. Tew. Impact of synthetic technique on pla-peo-pla physical hydrogel properties. *Macromolecules*, 40(22):7864–7873, 2007.

[143] Sarvesh K. Agrawal, Naomi Sanabria-DeLong, Gregory N. Tew, and Surita R. Bhatia. Structural characterization of pla-peo-pla solutions and hydrogels: Crystalline vs amorphous pla domains. *Macromolecules*, 41(5):1774–1784, 2008.

[144] Sarvesh K. Agrawal, Naomi Sanabria-DeLong, Gregory N. Tew, and Surita R. Bhatia. Rheological characterization of biocompatible associative polymer hydrogels with crystalline and amorphous endblocks. *Journal of Materials Research*, 21(8):2118–2125, 2006.

[145] E. M. Saffer, G. N. Tew, and S. R. Bhatia. Poly(lactic acid)-poly(ethylene oxide) block copolymers: New directions in self-assembly and biomedical applications. *Current Medicinal Chemistry*, 18(36):5676–5686, 2011.

[146] Khaled A. Aamer, Heidi Sardinha, Surita R. Bhatia, and Gregory N. Tew. Rheological studies of plla-peo-plla triblock copolymer hydrogels. *Biomaterials*, 25(6):1087 – 1093, 2004.

[147] Sarvesh K. Agrawal, Naomi Sanabria-DeLong, Jeannine M. Coburn, Gregory N. Tew, and Surita R. Bhatia. Novel drug release profiles from micellar solutions of pla-peo-pla triblock copolymers. *Journal of Controlled Release*, 112(1):64 – 71, 2006. ISSN 0168-3659.

[148] Bogdan Barz, Bradley S. Turner, Rama Bansil, and Brigita Urbanc. Folding of pig gastric mucin non-glycosylated domains: a discrete molecular dynamics study. *Journal of Biological Physics*, 38(4):681–703, Sep 2012.

[149] Mayandi Sivaguru, Jessica J. Saw, James C. Williams, John C. Lieske, Amy E. Krambeck, Michael F. Romero, Nicholas Chia, Andrew L. Schwaderer, Reinaldo E. Alcalde, William J. Bruce, Derek E. Wildman, Glenn A. Fried, Charles J. Werth, Richard J. Reeder, Peter M. Yau, Robert A. Sanford, and Bruce W. Fouke. Geobiology reveals how human kidney stones dissolve in vivo. *Scientific Reports*, 8(1), Sep 2018.

[150] Jeffrey A. Wesson, Richard J. Johnson, Marrilda Mazzali, Anne M. Beshensky, Susan Stietz, Ceci Giachelli, Lucy Liaw, Charles E. Alpers, William G. Couser, Jack G. Kleinman, and Jeremy Hughes. Osteopontin is a critical inhibitor of calcium oxalate crystal formation and retention in renal tubules. *Journal of the American Society of Nephrology*, 14(1):139–147, 2003.

[151] Masao Tsujihata. Mechanism of calcium oxalate renal stone formation and renal tubular cell injury. *International Journal of Urology*, 15(2):115–120, Dec 2007.

[152] Jeffrey A. Wesson, Elaine M. Worcester, John H. Wiessner, Neil S. Mandel, and Jack G. Kleinman. Control of calcium oxalate crystal structure and cell adherence by urinary macromolecules. *Kidney International*, 53(4):952 – 957, 1998. ISSN 0085-2538.

[153] Xiaoxia Sheng, Michael D. Ward, and Jeffrey A. Wesson. Adhesion between molecules and calcium oxalate crystals: Critical interactions in kidney stone formation. *Journal of the American Chemical Society*, 125(10):2854–2855, 2003.

[154] Sahar Farmanesh, Sriram Ramamoorthy, Jihae Chung, John R. Asplin, Pankaj Karande, and Jeffrey D. Rimer. Specificity of growth inhibitors and their cooperative effects in calcium oxalate monohydrate crystallization. *Journal of the American Chemical Society*, 136(1):367–376, 2014.

[155] Jeffrey D. Rimer, Zhihua An, Zina Zhu, Michael H. Lee, David S. Goldfarb, Jeffrey A. Wesson, and Michael D. Ward. Crystal growth inhibitors for the prevention of l-cystine kidney stones through molecular design. *Science*, 330 (6002):337–341, 2010.

[156] Jihae Chung, Ignacio Granja, Michael G. Taylor, Giannis Mpourmpakis, John R. Asplin, and Jeffrey D. Rimer. Molecular modifiers reveal a mechanism of pathological crystal growth inhibition. *Nature*, 536(7617):446–450, 2016.

[157] E. A. Abdel-Aal, A. M. K. Yassin, and M. F. El-Shahat. Effect of crystallization parameters and presence of aqueous extract of nigella sativa on growth inhibition of calcium oxalate monohydrate particles. *Particulate Science and Technology*, 36(2):226–234, 2016.

[158] Kang Rae Cho, Prashant Kulshreshtha, Kuang Jen J. Wu, Jong Seto, S. Roger Qiu, and James J. De Yoreo. The effects of different types of additives on growth of biomineral phases investigated by in situ atomic force microscopy. *Journal of Crystal Growth*, 509:8–16, 2019.

[159] Janet E. Crawford, E. P. Crematy, and A. E. Alexander. The effect of natural and synthetic polyelectrolytes on the crystallization of calcium oxalate. *Australian Journal of Chemistry*, 21(4):1067–1072, 1968.

[160] Joseph S. Manne, Naresh Biala, Arthur D. Smith, and Carl C. Gryte. The effect of anionic polyelectrolytes on the crystallization of calcium oxalate hydrates. *Journal of crystal growth*, 100(3):627–634, 1990.

[161] Mualla Oner and Paul Calvert. The role of acrylic polyelectrolytes and acrylic gels as crystallization inhibitors and promoters of calcium oxalate. In *Advances in Materials Science and Implant Orthopedic Surgery*, pages 247–263. Springer, 1995.

[162] H. Füredi-Milhofer and S. Sarig. Interactions between polyelectrolytes and sparingly soluble salts. *Progress in Crystal Growth and Characterization of materials*, 32(1-3):45–74, 1996.

[163] David E. Fleming, Wilhelm van Bronswijk, and Rosemary Lyons Ryall. A comparative study of the adsorption of amino acids on to calcium minerals found in renal calculi. *Clinical science*, 101(2):159–168, 2001.

[164] Emel Akyol, Ayhan Bozkurt, and Mualla Öner. The effects of polyelectrolytes on the inhibition and aggregation of calcium oxalate crystallization. *Polymers for Advanced Technologies*, 17(1):58–65, 2006.

[165] Emel Akyol and Mualla Öner. Inhibition of calcium oxalate monohydrate crystal growth using polyelectrolytes. *Journal of Crystal Growth*, 307(1):137–144, 2007.

[166] Semra Kırboğa and Mualla Öner. Inhibition of calcium oxalate crystallization by graft copolymers. *Crystal Growth and Design*, 9(5):2159–2167, 2009.

[167] Semra Kırboğa and Mualla Öner. The role of vinyl sulfonic acid homopolymer in calcium oxalate crystallization. *Colloids and Surfaces B: Biointerfaces*, 78 (2):357–362, 2010.

[168] Andrew D. Wallace, Ali Al-Hamzah, Christopher P. East, William O.S. Doherty, and Christopher M. Fellows. Effect of poly (acrylic acid) end-group functionality on inhibition of calcium oxalate crystal growth. *Journal of Applied Polymer Science*, 116(2):1165–1171, 2010.

[169] Christopher P. East, Andrew D. Wallace, Ali Al-Hamzah, William O.S. Doherty, and Christopher M. Fellows. Effect of poly (acrylic acid) molecular mass and end-group functionality on calcium oxalate crystal morphology and growth. *Journal of Applied Polymer Science*, 115(4):2127–2135, 2010.

[170] Annu Thomas, Elena Rosseeva, Oliver Hochrein, Wilder Carrillo-Cabrera, Paul Simon, Patrick Duchstein, Dirk Zahn, and Rüdiger Kniep. Mimicking the growth of a pathologic biomineral: shape development and structures of calcium oxalate dihydrate in the presence of polyacrylic acid. *Chemistry–A European Journal*, 18(13):4000–4009, 2012.

[171] Emel Akyol and Mualla Öner. Controlling of morphology and polymorph of calcium oxalate crystals by using polyelectrolytes. *Journal of Crystal Growth*, 401:260 – 265, 2014. ISSN 0022-0248.

[172] Malcolm A. Kelland, Mohamed F. Mady, and Rikke Lima-Eriksen. Kidney stone prevention: Dynamic testing of edible calcium oxalate scale inhibitors. *Crystal Growth & Design*, 18(12):7441–7450, 2018.

[173] Konstantinos D. Demadis and Mualla Öner. Inhibitory effects of "green" additives on the crystal growth of sparingly soluble salts. *Green Chemistry Research Trends*, pages 265–287, 2009.

[174] Wolfgang Kaiser. *Kunststoffchemie fur Ingenieure von der Synthese bis zur Anwendung*. Hanser, Munchen, 2011.

[175] H. D. Keith and F. J. Padden. Spherulitic crystallization from the melt. i. fractionation and impurity segregation and their influence on crystalline morphology. *Journal of Applied Physics*, 35(4):1270–1285, 1964.

[176] H. D. Keith and F. J. Padden. Spherulitic crystallization from the melt. ii. influence of fractionation and impurity segregation on the kinetics of crystallization. *Journal of Applied Physics*, 35(4):1286–1296, 1964.

[177] Sara Sanmartín, Javier Ramos, Juan Francisco Vega, and Javier Martínez-Salazar. Strong influence of branching on the early stage of nucleation and crystal formation of fast cooled ultralong n-alkanes as revealed by computer simulation. *European Polymer Journal*, 50:190–199, 2014.

[178] Giovanni Rojas, Bora Inci, Yuying Wei, and Kenneth B. Wagener. Precision polyethylene: Changes in morphology as a function of alkyl branch size. *Journal of the American Chemical Society*, 131(47):17376–17386, 2009.

[179] A. Häfele, B. Heck, T. Hippler, T. Kawai, P. Kohn, and G. Strobl. Crystallization of poly(ethylene-co-octene): Ii melt memory effects on first order kinetics. *European Physical Journal E*, 16(2):217–224, 2005.

[180] G. Hauser, J. Schmidtke, and G. Strobl. The role of co-units in polymer crystallization and melting : New insights from studies on syndiotactic poly(propene-co-octene). *Macromolecules*, 31(18):6250–6258, 1998.

[181] G. Strobl. From the melt via mesomorphic and granular crystalline layers to lamellar crystallites: A major route followed in polymer crystallization? *European Physical Journal E*, 3(2):165–183, 2000.

[182] Yuki Ono and Jiro Kumaki. In situ real-time observation of polymer folded-chain crystallization by atomic force microscopy at the molecular level. *Macromolecules*, 51(19):7629–7636, 2018.

[183] Peter Debye. Zur theorie der spezifischen wärmen. *Annalen der Physik*, 344 (14):789–839, 1912.

[184] Can Zhou, Marc A. Hillmyer, and Timothy P. Lodge. Micellization and micellar aggregation of poly(ethylene-alt-propylene)-b-poly(ethylene oxide)-b-poly(n-isopropylacrylamide) triblock terpolymers in water. *Macromolecules*, 44 (6):1635–1641, 2011.

[185] Zhifeng Bai, Yiyong He, Nicholas P. Young, and Timothy P. Lodge. A thermoreversible micellization-transfer-demicellization shuttle between water and an ionic liquid. *Macromolecules*, 41(18):6615–6617, 2008.

[186] Yongsheng Liu, Minghai Li, Rama Bansil, and Milos Steinhart. Kinetics of phase transition from lamellar to hexagonally packed cylinders for a triblock copolymer in a selective solvent. *Macromolecules*, 40(26):9482–9490, 2007.